

COUPLED THERMO-MECHANICAL FINITE-ELEMENT MODEL WITH
APPLICATION TO INITIAL SOLIDIFICATION

BY

HONG ZHU

B.S., Huazhong University of Sciences and Technology, 1985

M.S., Tsinghua University, 1987

THESIS

Submitted in partial fulfillment of the requirements
for the degree of Doctor of Philosophy in Theoretical and Applied Mechanics
in the Graduate College of the
University of Illinois at Urbana-Champaign, 1996

Urbana, Illinois

May, 1996

Hong Zhu

Coupled Thermal-Mechanical Finite Element Model with Application to Initial
Solidification

DOCTOR OF PHILOSOPHY

ABSTRACT

Computational modeling of mechanical behavior in a solidifying body is of great potential benefit to understand and improve material processes such as foundry shape casting, continuous casting and welding. Understanding the history of shape and stress during solidification processes is important for process development and can help in the prediction and prevention of problems such as cracks and depressions on the initial stage of continuous casting. This thesis is directed towards realizing this opportunity by developing and evaluating computational procedures for stress modeling of processes with solidification. An efficient coupled finite element thermo-mechanical model is applied to investigate thermal-mechanical behavior of the steel shell during the initial stages of solidification at the meniscus, focusing on the mechanisms of surface depression and surface crack formation.

To represent deformation phenomena properly over the wide range of temperatures encountered in solidification processes, it is accepted that unified elastic-viscoplastic models are better than classic creep and plasticity theory. However, these models are difficult to be implemented in finite element analysis because the constitutive differential equations for rate-dependent unified elastic-viscoplastic models are both highly nonlinear and mathematical "stiff". Three numerical time-integration schemes are evaluated to integrate such constitutive models. They include the explicit forward Euler scheme, the implicit backward Euler scheme and the alternating implicit / explicit scheme based on the operator-splitting technique. The latter two methods involve transforming the tensor algorithm constitutive models for isotropic materials into two scalar equations to solve at each spatial integration point for two unknowns: the stress magnitude and the inelastic strain magnitude. Several constitutive algorithms are examined to solve this nonlinear two equations system. This is similar to solving a uni-axial problem with prescribed strain rate. These "local" algorithms include the successive substitution method, the forward gradient method, the Newton-Raphson method, the bounded Newton method and Nemat-Nasser's explicit prediction method. The performance of these methods are compared using a computationally-demanding solidification test problem with known solution. Results indicate that a formulation comprised of the alternating implicit-explicit time integration scheme and the bounded Newton

method at the local level calculation is the most robust, accurate and efficient method.

A coupled transient finite element model based on the fixed-grid implementation of this formulation is developed to simulate temperature, shape, and stress development in a solidifying steel shell during initial stage of continuous casting. The model includes the effects of temperature-dependent properties, thermal shrinkage, phase transformations and creep, using an elastic-viscoplastic constitutive equation for low carbon steel. This model is validated through comparison with several benchmark problems, chosen to represent phenomena present during stress analysis of solidifying metals. The model is then used to investigate four different assumptions for simplifying the simulation of large, unconstrained castings into two dimensions.

This verified model is applied to predict the distorted shape of a vertical section through the solidifying shell, during a sudden fluctuation in liquid level at the meniscus. The results show that thermal stress causes the exposed portion of the thin shell to bend towards the liquid, when there is a severe, sudden drop in liquid level. In addition, the axial temperature gradient creates high transverse stresses. The subsequent rise in liquid level increases the bending. These results illustrate an important mechanism contributing to the formation of transverse surface depressions and short longitudinal surface cracks associated with severe liquid level fluctuations.

To my parents

ACKNOWLEDGMENTS

I wish to thank my advisor, Prof. Brian G. Thomas, for his encouragement, advice and support during the course of this work. I also express thanks to Prof. Tarek G. Shawki and Daniel A. Tortorelli for serving on my dissertation committee and for all that I have learned from them during my graduate studies. Furthermore, I would like to thank ARMCO Inc., Inland Steel, BHP, and LTV Steel and National Science Foundation for their financial support and the National Center for Supercomputing Applications for time on the CRAY Y-MP supercomputers.

I am very grateful to my parents, whose confidence in me has been a great source of energy.

I would like to express my appreciation to my wife Haifeng and my daughter Melissa for their love, support and understanding throughout this endeavor.

I would like to extend thanks to my colleagues Dr. Xiaoqing Huang, Dr. Avijit Moitra and graduate students Gouwei Li, Keith Rackers, David Lui, Robert Madavid for their encouragement and friendship throughout the duration of my graduate studies.

Table of Contents

Chapter 1	Introduction.....	1
	1.1 Background.....	1
	1.2 Objective.....	2
	1.3 Organization.....	2
	1.4 Reference	3
Chapter 2	Fixed-Grid Finite-Element Model of Mechanical Behavior of Solidifying Metals 4	
	2.1 Background.....	4
	2.1.1 Incorporating coupled effects such as fluid flow.....	7
	2.1.2 Solution strategies for coupled fields.....	8
	2.1.3 Numerical methods for stress analysis during solidification.....	9
	2.1.4 Constitutive models	9
	2.1.5 Numerical implementation of unified constitutive equations into finite element models	10
	2.1.6 Treatment of the liquid phase	11
	2.1.7 Phase Transformation	12
	2.1.8 Interaction with the mold.....	13
	2.1.9 Relative motion between the casting and the mold	14
	2.1.10 Two-dimensional models.....	15
	2.1.11 The present study	16
	2.2 Heat transfer / solidification modeling	17
	2.3 Mechanical model formulation.....	18

2.3.1	Constitutive equations.....	18
2.3.2	Time integration scheme.....	22
2.3.3	The constitutive algorithm (step 1).....	23
2.3.4	The boundary-value problem.....	25
2.3.5	Finite-element implementation (step 2).....	26
2.4	Model validation and examples	32
2.4.1	Cantilever beam with mechanical load	33
2.4.2	Thermal loading of a plate with temperature-dependent shear modulus.....	34
2.4.3	Unconstrained elastic pipe in generalized plane strain	35
2.4.4	Stress in a solidifying slab	36
2.4.4.1	Analytical solution.....	37
2.4.4.2	Numerical solution.....	38
2.4.4.3	Comparison with commercial package ABAQUS	42
2.4.4.5	Effect of two-dimensional stress state	46
2.4.4.6	Realistic constitutive behavior.....	48
2.6	Reference.....	51
Chapter 3	Comparison of Numerical Time-Integration Schemes and Finite-Element Implementations for Unified Temperature-Dependent Elastic-Viscoplastic Constitutive Models.....	61
3.1	Introduction.....	61
3.2	Unified constitutive equations	65
3.3	Time-integration procedure	67
3.3.1	Explicit time integration / forward Euler scheme	68
3.3.2	Implicit time integration / backward Euler scheme	69

	3.3.3 Mixed implicit-explicit time integration / alternating implicit-explicit scheme.....	70
	3.4 The constitutive algorithm	73
	3.4.1 The successive substitution (Picard method).....	76
	3.4.2 The Newton-Raphson method	77
	3.4.3 The forward gradient method.....	77
	3.4.4 The bounded Newton-Raphson method.....	78
	3.4.5 The Nemat-Nasser's explicit prediction method.....	80
	3.5 Spatial integration / finite element implementation.....	82
	3.6 Results and discussion	85
	3.6.1 Specified constitutive models	85
	3.6.2 Uniaxial calculations.....	87
	3.6.3 Thermal stress analysis in a solidifying slab	94
	3.7 Conclusion	101
	3.7 Reference.....	102
Chapter 4	Thermal Distortion of Solidifying Shell near Meniscus in Continuous Casting of Steel.....	107
	4.1 Introduction.....	107
	4.2 Model Description.	110
	4.2.1 Heat transfer model formulation.....	110
	4.2.2 Mechanical model formulation.....	113
	4.2.3 Special treatment for liquid level dropping / rising	113
	4.2.4 Thermo-mechanical property data	114
	4.2.4.1 Thermal conductivity	114

4.2.4.2 Enthalpy	115
4.2.4.3 Thermal linear expansion.....	116
4.2.5 Boundary conditions	116
4.2.6 Discussion of model assumptions	118
4.3 Results.....	120
4.4 Mechanism of surface depressions and longitudinal cracks	126
4.5 Discussion	126
4.6 Conclusions.....	129
4.7 References.....	129
Chapter 5 Summary and Conclusions.....	133
Appendix A Constant-Gradient Triangle Element in Chapter 4.....	135
Vita.....	137

List of Tables

Table 3.1	Comparison of Accuracy and Cost of Different Elastic-viscoplastic FEM Algorithms	100
Table 4.1	Simulation Conditions	118

List of Figures

Figure 2.1	Coupled phenomena in solidification analysis	6
Figure 2.2	Cantilever beam with shear load (test problem 1)	33
Figure 2.3 modulus34	Finite-element model of plate with temperature-dependent shear	
Figure 2.4	Finite element model of heated elastic hollow cylinder (test problem 3).....	36
Figure 2.5	Chilled slab with one-dimensional solidification	37
Figure 2.6	Constitutive behavior assumed in solidification test problem	38
Figure 2.7	Finite element model of solidification test problem	39
Figure 2.8 solution	Temperature distribution in solidification test problem from analytical	39
Figure 2.9 solution	Stress distribution through slab from elastic-viscoplastic finite element	41
Figure 2.10 solution of	Comparison of analytical solution and elastic-viscoplastic finite element	
	solidification test problem	41
Figure 2.11 problem	Comparison of elastic finite element approximations of solidification test	43
Figure 2.12	Effect of mesh refinement and time step size on relative error for	
solidification test	problem	44
Figure 2.13	Variation of computational cost with mesh refinement.....	45
Figure 2.14 problem	Effect of out-of-plane assumption on y stress for solidification test	47
Figure 2.15 problem	Effect of out-of-plane assumption on z stress for solidification test	47
Figure 2.16	Stress distribution with realistic (steel) constitutive equation for	
solidification test	problem	49
Figure 3.1	Uniaxial tension result from forward Euler scheme	88

Figure 3.2	Uniaxial tension results from forward gradient method	89
Figure 3.3	Uniaxial tension results from backward Euler scheme with N-R iteration	89
Figure 3.4	Uniaxial tension results from backward Euler scheme with Nemat-Nasser prediction method	90
Figure 3.5	Stress relaxation results from forward Euler scheme	92
Figure 3.6	Stress relaxation results from forward gradient method	92
Figure 3.7	Stress relaxation results from backward Euler scheme with N-R iteration	93
Figure 3.8	Stress relaxation results from backward Euler scheme with the Nemat- Nasser prediction method	93
Figure 3.9	Chilled slab with one-dimensional solidification	95
Figure 3.10	Constitutive behavior assumed in solidification test problem	96
Figure 3.11	Temperature distribution in solidification test problem from analytical solution	97
Figure 3.12	Finite element model of solidification test problem	97
Figure 3.13	Comparison of analytic solution and FEM solutions for solidification with different algorithms	100
Figure 3.14	Comparison FEM solutions with realistic constitutive equation	101
Figure 4.1	Schematic of initial solidification near meniscus	108
Figure 4.2	Movement of longitudinal slice model domain during simulation	111
Figure 4.3	Thermal conductive of Carbon and Stainless steel as a function of temperature	115
Figure 4.4	Enthalpy of carbon steel and stainless steel used in the model	115
Figure 4.5	Thermal linear expansion curves for carbon and stainless steel	116
Figure 4.6	Temperature profile through shell	121
Figure 4.7	Axial (z) stress profiles through constrained shell	121

Figure 4.8	Distorted shell shape with temperature contours.....	122
Figure 4.9	Stress and temperature down shell surface (1.8s).....	123

Chapter 1

Introduction

1.1 Background

Many manufacturing and fabrication processes such as foundry shape casting, continuous casting and welding involve solidification phenomena. Understanding the history of shape and stress during solidification is important for process development and can help in the prediction and prevention of detrimental residual stress, distortion, crack formation and even porosity formation. With the rapid development of computer hardware and computational techniques in recent years, numerical modeling offers the potential to realistically investigate these complex processes. However, owing to the great computational complexity of the problem, many previous stress analysis have oversimplified several important phenomena. one of those is realistic constitutive models to characterize mechanical behavior. To properly represent deformation phenomena such as strain hardening and rate-dependent creep-plasticity interactions over a wide range of temperatures encountered in elevated-temperature processes, it is accepted that unified elastic-viscoplastic models are better than classic creep and plasticity theory [1, 2]. However, there is a considerable challenge to utilize these models due to the lack of efficient and robust methods for numerical implementations of them in large-scale finite element analysis.

Most of the surface defects in continuous casting are suspected to initiate during the initial stages of solidification in the mold, especially near the meniscus. These defects include deep oscillation marks, surface depressions, longitudinal and transverse surface cracks. Although a body of empirical knowledge and evidence exists, the exact mechanisms for many of these problems are still unclear.

1.2 Objectives

The first objective of this research is to develop and evaluate new computational procedures for stress modeling of process with solidification, emphasis on the numerical implementation of the unified constitutive models for fixed-grid mechanical analysis of solidification. The second objective is to develop an efficient finite-element model to investigate thermal-mechanical behavior of the steel shell during the initial stages of solidification, focusing on the mechanisms of surface depression and surface crack formation.

1.3 Organization

The rest of this thesis is organized as follows.

In chapter 2, the issues for modeling thermal stress generation with solidification are reviewed. A finite-element fixed-grid model for modeling mechanical behavior with solidification is presented. This model features a robust numerical scheme to handle the highly-nonlinear unified constitutive equations employed to describe high-temperature mechanical behavior and appropriate two-dimensional assumptions to properly simplify the three-dimensional system. Several techniques are proposed to handle liquid elements in the context of the fixed-grid method. This model is validated by a benchmark test problem for thermal-mechanical analysis of solidification with a known analytical solution. Several computational issues such as element type, mesh and time step size, and two-dimensional approximation are discussed through numerical experiments.

In chapter 3, the numerical implementations of the unified rate-dependent constitutive models in large-scale analysis are discussed. Three numerical time-integration schemes are employed to integrate the constitutive equations, including the explicit forward Euler scheme, the implicit backward Euler scheme and the alternating

implicit-explicit scheme based on the operator-splitting technique. Several constitutive algorithms are examined for the local iteration at material points. These "local" algorithms include the successive substitution method, the forward gradient method, the Newton-Raphson method, the bounded Newton method and the Nemat-Nasser's explicit prediction method. The performance of all combinations of methods were compared using the computational-demanding solidification test problem presented in chapter 2.

In chapter 4, the best method found in chapter 3 and described in chapter 2 is implemented into a two-dimensional, transient, finite-element model to simulate temperature, shape, and stress development in the steel shell, during the initial stages of solidification in the mold. The model is applied to predict the distorted shape of a vertical section through the shell, during a sudden fluctuation in liquid level at the meniscus. The results illustrate an important mechanism contributing to the formation of transverse surface depressions and short longitudinal surface cracks associated with severe liquid level fluctuations.

In chapter 5, conclusions are drawn from this research.

1.4 Reference

1. P. Kozlowski, B.G. Thomas, J. Azzi and H. Wang, Simple Constitutive Equations for Steel at High Temperature, Metallurgical Transactions A, vol. 23 (March) (1992) 903-918.
2. A.K. Miller, Unified Constitutive Equations for Creep and Plasticity, (Elsevier Applied Science Publishers Ltd, Essex, United Kingdom, 1987).

Chapter 2

Fixed-Grid Finite-Element Model of Mechanical Behavior of Solidifying Metals

Computer modeling of mechanical behavior in processes involving solidification requires treatment of many complex phenomena which present several numerical difficulties. This chapter reviews the available methods and presents an accurate, robust and efficient model of mechanical behavior involving solidification along with its finite element implementation. The model includes a stable and efficient method to integrate the unified elastic-visco-plastic equations used to describe the high-temperature constitutive behavior. The mechanical interaction between the solid phase and the liquid phase is incorporated through internal constraint conditions. The proposed model is validated through comparison with several benchmark problems, chosen to represent phenomena present during stress analysis of solidifying metals. The model is then used to investigate four different assumptions for simplifying the simulation of large, unconstrained castings into two dimensions. The model is ready to simulate the initial solidification of the steel shell in continuous casting processes and other important phenomena.

2.1 Background

Computational modeling of mechanical behavior in a solidifying body is of great potential benefit to understand and improve material processes such as foundry shape casting, continuous casting and welding. Understanding the history of shape and stress during solidification processes is important for process development and can help in the prediction and prevention of detrimental residual stress, distortion, crack formation and even porosity formation. With the rapid development of computer hardware and computational techniques in recent years, numerical modeling offers the potential to realistically investigate these complex processes. A few analytical solutions of stress development in a solidifying body have been developed by Weiner and Boley [1], Tien and Kaump [2]. Although these

analyses oversimplify the complex physical phenomena associated with solidification, they are useful in providing benchmark problems for verification of the numerical models.

The first task in mechanical modeling of thermal processes such as solidification is accurate prediction of the transient temperature history, which controls the thermal strains responsible for most of the stresses. The major computational feature of modeling heat transfer with solidification is the treatment of the latent heat which is evolved at the moving solid-liquid interface. Many different numerical methods have been developed to handle this. These include fixed-grid methods, reviewed by Voller et al [3], front-tracking methods [4], deforming finite-element mesh methods [5] and arbitrary Lagrangian-Eulerian methods [6].

Comparatively, the mathematical modeling of stress generation in solidification processes has received less attention. One reason for this is the number of computational difficulties encountered when modeling the complex phenomena which govern the mechanical behavior. Figure 1 shows how these phenomena interact to couple together the important variables affecting mechanical analysis (stress and strain) during solidification, which include fluid flow, heat transfer, and microstructure. Two-way coupling between these four separate types of analysis greatly escalates the computational difficulties. For example, while temperature controls stress, stress in turn affects temperature in two ways. Firstly, the changing degree of contact between the mold and the casting affects the interface heat transfer, which can control temperature development. Secondly, the energy dissipated during plastic deformation is important to temperature in large-strain processes, such as squeeze casting, rolling, and forging. Fortunately, the latter effect contributes little to the temperature distribution during small-strain solidification processes, so is often neglected. Further coupling caused by several other phenomena are included in Figure 2.1.

Figure 2.1 Coupled phenomena in solidification analysis

This complex interaction of phenomena creates computational problems. Additional problems arise due to the moving (dynamically changing) solid-liquid interface, complex thermal and mechanical loading, highly nonlinear rate-dependent constitutive relationships, heterogeneous non-isotropic temperature-dependent material properties, solid-state phase transformations, microstructural effects such as segregation, interaction and relative motion between the casting and the mold, and the inherent three-dimensional nature of the process. The development of computational methods to handle these phenomena constitutes important fields of current research, which are reviewed in the next sections as background for the present study.

2.1.1 Incorporating coupled effects such as fluid flow

To model mechanical behavior during solidification, an accurate temperature field is needed to calculate thermal strain and materials properties at every time step. Convective heat transfer in the liquid can affect the analysis of temperature. Some attempts to simultaneously model the coupled thermal-fluid-mechanical system have been made, although this is very computationally expensive and difficult. For example, Kelly et al [7] transferred data between two commercial finite element packages to calculate coupled velocity / temperature (FIDAP) and thermal stress (ABAQUS) to simulate the continuous casting of round billets. The easiest method to account for convective heat transfer is simply to increase the liquid conductivity. When the solidification heat transfer has little influence on the fluid flow pattern, a more accurate method is to uncouple the fluid flow and thermal-stress calculations. The convective heat transfer effect can be calculated by a separate fluid flow model [8], whose results are used as an internal heat source or internal boundary condition in a heat conduction model [9]. This method is appropriate when a coupled thermal-mechanical analysis is necessary to account for the effect of the changing shape of the casting and mold on heat transfer across the interfacial gap between them. Mechanical behavior can greatly influence heat transfer in some processes, such as continuous casting of steel, by changing the size of

the low-conductivity air gap [10, 11], or changing the pressure-related contact thermal conductivity [12].

In other processes, such as sand casting, thermal-mechanical coupling across the interfacial gap is not important. In these cases, it may be more appropriate to couple the fluid flow and heat transfer calculations into a single model. For example, Boehmer et al [13] developed a thermal-mechanical model to analyze mechanical behavior in a continuous casting machine by using an in-house finite-difference code for heat transfer and the commercial finite-element package ADINA for stress analysis. Fjaer and Mo [14] used a similar method to model the direct chill casting of aluminum billets. Although this framework can allow realistic incorporation of fluid flow effects, these models ignore the effect of the mechanical calculation on the gap heat transfer.

2.1.2 Solution strategies for coupled fields

The computational efficiency of modeling transient nonlinear systems with coupled fields depends greatly on the time integration algorithm and the manner of iterating between the coupled fields. Two main strategies can be used for time-stepping with coupled fields. The monolithic, or simultaneous solution scheme employs the same time-stepping algorithm to the fully-coupled system. The staggered scheme applies different time-stepping algorithms to the different parts of the coupled system [15, 16].

The simultaneous-iteration approach and nested-iteration approach are used to solve nonlinear coupled systems [16, 17]. Different combinations of time integration scheme and iteration manner for transient nonlinear coupled fields have their own advantages and the best algorithm depends on the specific problem. For fully-coupled thermo-mechanical analysis with solidification, all of the schemes in previous models [7, 9, 13, 18, 19] use a staggered integration algorithm with a nested iteration technique, which is easy to implement with two separated single-field analysis codes.

2.1.3 Numerical methods for stress analysis during solidification

Various numerical methods have been used for modeling stress in a solidification process. Some previous researchers, including Cross [20] and Hattel et al [21] have employed control-volume finite-difference methods to simulate three-dimensional thermoelastic stresses in die casting. Heinlein and Mukherjee [22] presented a boundary integral equation method to analyze mechanical behavior for the one dimensional solidification of an aluminum bar. However, most previous numerical models [7, 14, 23-28] are based on the finite-element method, due to its flexibility for efficiently handling arbitrary geometric shapes, as well as complex material properties and other nonlinear phenomena.

2.1.4 Constitutive models

Realistic models of constitutive behavior and materials properties are the foundation of successful modeling of mechanical behavior. During solidification and subsequent cooling processes, evolution of the microstructure causes a large variation in the mechanical properties. The constitutive model should reproduce experimental mechanical behavior measured over the range of process conditions of interest. Typical experiments include tension tests, creep tests, stress relaxation tests and cyclic tests. At high temperatures, time-dependent processes (creep) are very important, so the inelastic component of strain is highly rate-dependent

For solidification processes, various constitutive models have been used. These include an elastic model by Manesh [29], an elastic / perfectly plastic model by Weiner and Boley [1] , an elastic-plastic model by Tszeng et al [24], an elastic-hyperbolic type creep model by Heinlein et al [22] and Zabaras et al [4], a separated elastic-plastic-creep model is used by Kristiansson [23] and Boehmer et al [13], a simple visco-plastic model by Dalin [30], a modified Perzyna's visco-plastic model by Inoue et al [25, 31] and Williams et al [26], a unified elastic-viscoplastic model by Fjaer and Mo [14] and Hannart et al [19], and internal

variable models by Mo and Holm [32], Smelser and Richmond [28], and Bamman [33]. The latter unified models are growing in popularity due to their physically-based, phenomenological approach [34-36].

Unified models differ from classic plasticity - creep models in that there is no explicit yield condition or loading/unloading criteria. Unified models treat creep and plasticity as a unified "inelastic strain", whose instantaneous rate of change depends on the current stress, temperature, and "structure". Structure is represented by one or more scalar or tensor state-variables, which evolve with time, and can include phenomena such as rate of phase transformation. Traditional elastic-viscoplastic models are obtained when inelastic strain is selected as the structure parameter. The kinematic hardening or Bauschinger effect, which can be described with a structure parameter in several unified models [34, 35], has been proven important to mechanical behavior with solidification by Mo et al [32] and Bammann et al [33]. Although unified models can produce more realistic mechanical behavior, there is a lack of high-temperature experimental data, such as that needed to characterize the Bauschinger effect for the range of alloys, strain-rates, and stress-ranges of interest. An additional problem is numerical instability, as these constitutive equations are extremely nonlinear, or "stiff", meaning that a small change in one state variable may produce large changes in others [35, 37, 38].

2.1.5 Numerical implementation of unified constitutive equations into finite element models

Numerical integration and related finite-element implementation of constitutive equations is another important issue of current interest, particularly for the highly non-linear unified models. A good method has both numerical stability and computational efficiency. Many schemes [39-52] have been proposed to integrate the stress rate equations. These schemes treat the total strain rate as an implicit term during solution of the global equilibrium equations and boundary conditions. Inelastic strain rate is treated as either explicit or implicit, depending on the time integration scheme. With an explicit forward Euler time-integration

scheme, a very small time step size may be needed to satisfy stability requirements [39, 40]. Several semi-implicit forward-gradient methods have been developed to overcome the stability restriction of explicit integration of the inelastic strain rate [36, 43-46]. These methods are based on a truncated Taylor-series approximation to linearize the inelastic strain rate and avoid iteration. They have the drawback of less accuracy over the knee of the stress-strain curve due to their simple approximation.

On the other hand, the implicit treatment of inelastic strain rate requires intensive computational effort to iteratively solve the nonlinear global system of equations [39, 41-43]. Two well-known methods to accomplish this are the tangent stiffness method and the initial strain method [39, 47, 53]. The initial strain method has the advantage of maintaining a constant global stiffness matrix during iterations, although its convergence rate is at best linear. In the tangent stiffness method, the global stiffness matrix must be reformed at every iteration, but the convergence rate may be faster. The quadratic convergence rate of the Newton-Raphson scheme is achieved only when the "consistent tangent modulus" is used [47, 48, 54]. These methods require a local algorithm to integrate the inelastic strain rate to update the stress at each material point or integration point. This local algorithm has a great influence on both computational efficiency and stability. Convergence problems have been reported when simple iteration with successive substitution is used as the local algorithm [40]. For implicit integration of their unified constitutive equation for solidification, Fjaer and Mo used the initial strain method at the global level and a forward gradient method at the local level [14].

2.1.6 Treatment of the liquid phase

Incompressible liquid is subject to large shear deformation without generating stress. However, it can transmit hydrostatic pressure to the solidifying shell. When gravity acting on the liquid is significant, this pressure can be the dominant mechanical load, responsible for

creep bulging in large castings. The stress state is always continuous across the solid-liquid interface [22, 55]. Several approaches can be taken to model this behavior.

One method is to numerically “strip away” the liquid elements according to the results of the heat transfer calculation. Liquid elements are simply not assembled into the stiffness matrix [7, 13, 14]. Pressure boundary conditions are easily applied to the new surfaces of the remaining solid domain. When the liquid is exposed to ambient pressure, the boundary condition is simply hydrostatic pressure due to gravity, which increases in proportion to distance below the liquid surface. This method has been applied successfully to steady continuous casting [7, 13, 14], but has numerical disadvantages when the solidification front moves with time. Zabarar et al [4] proposed a front-tracking thermomechanical finite-element model in which remeshing is necessary at every time step.

Alternatively, a time-invariant mesh or “fixed-grid” method [19, 23-27, 56, 57] can be applied by altering the properties of the liquid with temperature. Besides easier numerical treatment of arbitrary movement of the solidifying interface in existing stress codes, avoiding remeshing has the major advantage of robust handling of complex interactions between the thermal and the mechanical behavior, such as gap heat transfer and local remelting [58]. Moreover, modeling the liquid domain may be of interest. Recent work on crack initiation criteria [59] indicates that a critical level of tensile strain in the presence of a critical liquid fraction range is responsible for hot-tear crack formation. To model this effect requires realistic simulation of strain in the mushy zone of alloy solidification. Methods to accomplish this will be discussed in further detail later in this paper.

2.1.7 Phase Transformation

During solidification and subsequent cooling processes, complex coupling may exist between heat transfer, mechanical behavior and solid-state phase transformations [12, 60]. Heat transfer is greatly influenced by the release or absorption of latent heat during phase

transformation. Phase transformation affects stress generation in two ways. Firstly, it creates additional strain due to the density change. This is readily incorporated into a unified thermal strain [27, 61]. Secondly, phase transformation creates additional inelastic strain. This effect, known as “phase transformation plasticity” [62-64], may have an important influence on the mechanical analysis. In turn, phase transformation kinetics are strongly affected by both temperature and internal stress. This may require a separate model of the microstructure, including phenomena such as the critical undercooling for nucleation [65]. The effect of stress is seldom considered because the microscopic mechanisms are not fully understood.

Several coupled thermal-mechanical models [7, 9, 18] have been developed for casting analysis, which include the effects of phase transformation. Das et al [66] shown that the interaction of stress and phase transformation has a significant effect on the residual stress for the gas metal arc welding process.

2.1.8 Interaction with the mold

Interaction between the casting and the mold affects both the loading on the exterior of the solidifying shell for stress analysis and the size of the interfacial gap for heat transfer analysis. This requires the stress analysis to be fully coupled with the thermal analysis.

Contact phenomena are involved in solidification processes through mechanical interaction between the shell and the mold. Strong nonlinearity is created because, in general, the contact boundary is not known *a priori*. This can be mathematically described as an inequality constraint [67, 68]. Three main approaches for numerical treatment of contact in the context of finite-element methods include the Langrange multiplier method [69-71], penalty method [67, 72] and augmented-Lagrangian method [17, 73, 74]. However, converged solutions are computationally expensive to obtain for complex contact problems. For example, Boehmer et al [13] reported that the analysis of the mechanical behavior of the

solidified shell in a continuous casting machine with mold constraint requires ten times the computation time of the analysis without mold constraint.

If the behavior of the contact is known a priori, it is possible to develop special algorithms to improve the convergence rate. For the analysis of casting processes, several algorithms [9, 57, 75, 76] take advantage of the known behavior of air gap formation between the shell and the mold. Recently, a formulation [77, 78] based on the microscopic physical behavior of the surface has been proposed for thermomechanical contact analysis. This formulation is reported to be easy to implement into existing finite element codes using nonlinear spring elements.

2.1.9 Relative motion between the casting and the mold

The analysis of processes such as continuous casting, squeeze casting, and rolling present the additional computational challenge of large relative motion between the processing materials and the mold or “tools”. As explained by Zienkiewicz [79], a Lagrangian description is usually adopted for transient processes, while an Eulerian description is often used for steady state problems. An Eulerian description with a “fluid approach” fixes the mesh at spatial points (in the “laboratory” frame of reference). Material behavior is modeled as a rate-dependent non-Newtonian fluid, which travels through the model domain. Velocity is selected as the primary field variable and the convective terms appear in the governing equations. Special updating schemes are required for the convective terms. This added complexity creates numerical difficulties, particularly when incorporating the effects of creep [79] or when modeling a free surface [30]. Several models use this approach [7, 14, 30, 80, 81].

On the other hand, in a Lagrangian description with a “solid approach”, the computational mesh moves with the material points. Material behavior is described with Hooke’s generalized law, the primary field variable is displacement or incremental

displacement, and variables with path and history dependencies are easy to update. The shortcoming of this approach is that continuous remeshing is necessary if there is large relative motion. This may be computationally-intensive unless the casting and mold move as rigid bodies along paths which are known a priori.

Other methods have been developed to overcome the disadvantages of pure Lagrangian and pure Eulerian descriptions when modeling contact problems with large deformation and large relative motions. For small-strain processes such as continuous casting, most models [9, 23, 24, 57, 82] mathematically follow a slice through the solidifying shell down through the mold, taking advantage of the small deformation rate relative to the casting speed. These models may be called arbitrary Lagrangian-Eulerian descriptions [83-88]. Several investigations employ this method, where the grid point velocity in the undiscritized third direction is fixed at the casting speed and a fully-Lagrangian frame is used in the slice plane.

2.1.10 Two-dimensional models

Although solidification, like any process, is inherently three-dimensional, the tremendous complexities make it desirable to use a two-dimensional model for computational efficiency. To model stress with solidification, several different two-dimensional models have been used, including axisymmetric [4, 7, 10, 14, 28, 31, 89], shell [90, 91], plane stress [26, 56, 92], plane strain [13, 24, 25, 57], generalized plane strain and plane deformation behavior [23, 93, 94]. The axisymmetric condition is naturally employed whenever there is radial symmetry in the geometry, boundary conditions, and properties. Accuracy of the other five two-dimensional approximations should be judged by comparison with three-dimensional analysis or direct experimental verification. Wikander et al [94] examined three different two-dimensional finite-element models of welding and compared the numerical and experimental residual stress and strain results. [Plane deformation was found to best approximate a D-shaped cross-section.](#)

For numerical implementation of the generalized-plane-strain condition, extra primary variables must be solved in the undiscretized direction. Either the direct solver [95] or the iteration method [96-98] can be used to solve the mixed variables in the resulting system of equations. The best method to use depends on the bandwidth of the stiffness matrix and the number of global freedom degrees and will be investigated as part of this study.

2.1.11 The present study

The above discussion has shown that the modeling of stress generation with solidification many complex interactions between phenomena and involves many computational difficulties. One of the greatest computational challenges remaining is the development of realistic models of entire casting processes, including all important phenomena. Once a model is developed, it should be verified with known solutions that test each of its features. As part of the verification stage, important computational aspects such as element type, mesh density, time step size, methods for liquid domain, two-dimensional stress state should be carefully examined. Most previous stress models have not been thoroughly validated. Moreover, due to the complexity of problem and lack of robust algorithms to handle the complex constitutive models, most previous stress models are limited to two-dimensional analysis, use unrealistic constitutive models. There is a great incentive to develop and implement efficient computational algorithms into validated stress models of solidification processes.

This chapter presents a new model for the simulation of mechanical behavior in solidifying metals. It is based on the fixed-grid finite element method, and includes an efficient scheme for finite-element implementation of the unified elastic-viscoplastic constitutive equations. Several different two-dimensional versions of the model have been tested, using typical problems involved in mechanical behavior with solidification. Several essential computational issues are evaluated. A detailed comparison study of different methods for finite-element implementation of the unified constitutive equations will be

discussed in future papers. The model presented here is being developed into a fully-coupled thermo-mechanical model of the continuous casting process for steel slabs, including other important phenomena such as turbulent multi-phase flow and mold distortion.

2.2 Heat transfer / solidification modeling

Assuming that the energy generated by mechanical work is insignificant in processes with solidification, the energy balance equation can be written as:

$$\rho c_p \frac{DT}{Dt} = (K T, i), i + Q, \quad (2.1)$$

where ρ , c_p , K , Q are the temperature-dependent density, specific heat, thermal conductivity and internal heat source density respectively. $\frac{DT}{Dt}$ is the time-derivative in the Lagrangian reference frame. In a spatially-fixed Eulerian frame,

$$\frac{DT}{Dt} = T, t + V_i T, i \quad , i, j = 1, 2, 3 \text{ (summation on } i) \quad (2.2)$$

where V is velocity of the spatial point.

In general, the boundary conditions on the entire surface of the domain may be classified into three portions:

$$T = \bar{T} \quad \text{on } S_T, \quad (2.3)$$

$$(-K T, i) n_i = \bar{q} \quad \text{on } S_q, \quad (2.4)$$

$$(-K T, i) n_i = h (T - T_a) \quad \text{on } S_h, \quad (2.5)$$

in which \bar{T} is a fixed temperature on the boundary portion S_T , \bar{q} is the prescribed heat flux at the boundary S_q and h is the heat transfer coefficient on the remaining boundary portion S_h with corresponding ambient temperature, T_a . \mathbf{n} is the unit normal vector of the surface of the domain.

Many other papers deal with treatment of the above partial different equation and boundary conditions to solve for the temperature field using the finite element method [99]. With fixed-grid techniques, the important non-linear effect of the latent heat of solidification can be accounted for through several different methods, reviewed elsewhere [3, 100].

Since attention in this study is focused on the mechanical models of processes with solidification, a simple analytical solution to this partial differential equation is used to calculate thermal strain and temperature-dependent mechanical properties [1].

2.3 Mechanical model formulation

2.3.1 Constitutive equations

Assuming small strains, small displacements and small rotations, the total strain rate tensor $\dot{\boldsymbol{\epsilon}}$ can be additively decomposed into components consisting of an elastic strain rate tensor $\dot{\boldsymbol{\epsilon}}^e$, an inelastic strain rate tensor $\dot{\boldsymbol{\epsilon}}^p$ and a thermal strain rate tensor $\dot{\boldsymbol{\epsilon}}^T$,

$$\dot{\boldsymbol{\epsilon}} = \dot{\boldsymbol{\epsilon}}^e + \dot{\boldsymbol{\epsilon}}^p + \dot{\boldsymbol{\epsilon}}^T . \quad (2.6)$$

The inelastic strain rate includes the effects of both time-independent plasticity and time-dependent creep.

The stress tensor $\boldsymbol{\sigma}$ is obtained from the generalized form of Hooke's law,

$$\boldsymbol{\sigma} = \mathbf{C} : \boldsymbol{\epsilon}^e , \quad (2.7)$$

in which \mathbf{C} is a fourth-order isotropic elastic tensor with components :

$$C_{ijkl}(T) = \lambda(T) \delta_{ij} \delta_{kl} + \mu(T) (\delta_{ik} \delta_{jl} + \delta_{il} \delta_{jk}) , \quad (2.8)$$

where $\lambda(T)$ and $\mu(T)$ are temperature-dependent Lamé constants and δ_{ij} are components of the kronecker delta, $\boldsymbol{\delta}$. The corresponding rate form of the constitutive relation can be written as

$$\dot{\boldsymbol{\sigma}} = \mathbf{C} : (\dot{\boldsymbol{\epsilon}} - \dot{\boldsymbol{\epsilon}}^T - \dot{\boldsymbol{\epsilon}}^p) + \dot{T} \frac{\partial \mathbf{C}}{\partial T} : (\boldsymbol{\epsilon} - \boldsymbol{\epsilon}^T - \boldsymbol{\epsilon}^p). \quad (2.9)$$

In the second term of the above equation, the changes in the elastic tensor caused by temperature variation are seen to contribute to the stress rate. Although this term is often neglected, its effect is significant in solidification problems. The formulation (2.7) - (2.9) is a classical hyperelastic equation in the absence of inelastic deformation.

Thermal strain $\boldsymbol{\epsilon}^T$ is defined as

$$\boldsymbol{\epsilon}^T = [\text{TLE}(T) - \text{TLE}(T_0)] \boldsymbol{\delta}, \quad (2.10)$$

in which the unified state function TLE, thermal linear expansion, accounts for the volume changes caused by both temperature differences and phase transformations. T_0 is reference temperature, typically chosen to be the solidus temperature. TLE can be found from the mass density, ρ as:

$$\text{TLE}(T) = \sqrt[3]{\frac{\rho(T_0)}{\rho(T)}} - 1.0. \quad (2.11)$$

In mixed phase regions, TLE can be found from a weighted average using the TLE curves measured for each of the individual phases present, based on their volume fractions. For example, during the solidification of steel, liquid (l), delta ferrite (δ), austenite (γ), alpha ferrite (α), and iron carbide (Fe_3C) may be present:

$$\text{TLE} = (\%l) \text{TLE}_l + (\%\delta) \text{TLE}_\delta + (\%\gamma) \text{TLE}_\gamma + (\%\alpha) \text{TLE}_\alpha + (\%\text{Fe}_3\text{C}) \text{TLE}_{\text{Fe}_3\text{C}}, \quad (2.12)$$

This formulation makes it easy to use a separate microstructure model to find the phase fractions present at each time and location. This microstructure model could simulate phase transformation kinetics to account for non-equilibrium conditions, where the phases present are not a direct function of temperature. Alternatively, the simple microstructure model used

here assumes equilibrium conditions, based on the phase diagram to calculate the phase fractions. Jablonka and Harste [101] provide a complete TLE function from the melting temperature to room temperature for plain-carbon steels.

Thermal strain rate $\dot{\epsilon}^T$ during time interval $[t, t+\Delta t]$ is taken in a backward-difference form of thermal strain as

$$\dot{\epsilon}^T = \frac{[TLE(T_{t+\Delta t}) - TLE(T_t)]}{\Delta t} \delta. \quad (2.13)$$

Assuming associated plastic flow, the inelastic strain rate $\dot{\epsilon}^P$ given by the Prandtl-Reuss relations [102] is

$$\dot{\epsilon}^P = \sqrt{\frac{3}{2}} \frac{\dot{\bar{\epsilon}}^P}{\bar{\sigma}} \mathbf{N}. \quad (2.14)$$

This treatment ignores spatial anisotropy due to the inherent directional properties of crystals and their different orientation. This is likely to be critical when modeling scale is on the order of the grain size. Thus this work is only good for macroscopic behavior relative to the grain columnar.

In above equation (2.14), \mathbf{N} is the unit direction tensor of inelastic strain rate, which is defined as:

$$\mathbf{N} = \sqrt{\frac{3}{2}} \frac{\boldsymbol{\sigma}'}{\bar{\sigma}}, \quad (2.15)$$

Here the deviatoric stress tensor $\boldsymbol{\sigma}'$, the Von-mises effective stress $\bar{\sigma}$, and the equivalent inelastic strain $\bar{\epsilon}^P$ are defined by

$$\boldsymbol{\sigma}' = \boldsymbol{\sigma} - \frac{1}{3} \text{tr}(\boldsymbol{\sigma}) \delta, \quad (2.16)$$

$$\bar{\sigma} = \sqrt{\frac{3}{2} \boldsymbol{\sigma}' \cdot \boldsymbol{\sigma}'}, \quad (2.17)$$

and

$$\bar{\epsilon}^p = \sqrt{\frac{2}{3} \boldsymbol{\epsilon}^p \cdot \boldsymbol{\epsilon}^p} , \quad (2.18)$$

respectively. The equivalent inelastic strain rate is a function of the current effective stress and the structure parameter

$$\dot{\bar{\epsilon}}^p = f(\bar{\sigma}, s) , \quad (2.19)$$

in which s represents a scalar structure parameter or “internal variable”. Its evolution equation takes the form

$$\dot{s} = g(\bar{\sigma}, s) . \quad (2.20)$$

This single internal variable unified constitutive model is used to describe the equivalent inelastic strain rate, which represents both time-dependent creep and time-independent plasticity. This approach is natural because creep strain is significant during tensile tests at high temperature and cannot be distinguished from plastic strain. Many different models [14, 28, 103-105] employ the equivalent inelastic strain $\bar{\epsilon}^p$ as the single structure parameter s in a rate-dependent constitutive equation. Equations (2.20) and (2.21) generally are strongly-nonlinear ordinary differential equations and may be mathematical "stiff" in some regions. Special attention is required in their numerical integration. During solidification and other phase changes, the structure parameter may change suddenly, according to the sudden change in microstructure. When this occurs, the structure variable should be reset to an appropriate initial value for the new phase. Thus, for a strain-hardening viscoplastic constitutive model, inelastic strain accumulated in the old phase (e.g., liquid phase) should not contribute directly to material behavior in new phase range (e.g., solid phase). With this treatment, completely fictitious material behavior may be involved for computational convenience in the liquid-phase region without necessarily creating inaccuracy

in another. In a later section, this idea is exploited to handle the liquid domain in the fixed-grid method.

Knowing the values of all state variables (σ , s) at time t , these variables are determined at time $t+\Delta t$ through integration of the evolution equations (2.6) and (2.20). Thermal strain rate is assumed to be a constant during $[t, t+\Delta t]$ and is known from prior thermal analysis and equation (2.13). The proposed time integration scheme is based on an operator-splitting technique which alternates between implicit and explicit forms of the total strain rate and inelastic strain rate when integrating equation (2.6). This scheme was used by Glowinski and Talle [106] to integrate a viscoplastic model without the hardening effects. The method originated from the ADI scheme of Douglas and Rachford for transient heat conduction problems [107]. Time integration is carried out in two steps.

2.3.2 Time integration scheme

In the first “local” step, stress and inelastic strain rate are estimated through implicit time integration at each material point, knowing the total strain rate at time t from the previous time step:

$$\hat{\sigma}_{t+\Delta t} = C_{t+\Delta t} : [\epsilon_t - \epsilon^T_t - \epsilon^p_t + (\dot{\epsilon}_t - \dot{\epsilon}^T_{t+\Delta t} - \hat{\epsilon}^p_{t+\Delta t})\Delta t] . \quad (2.21)$$

In the second “global” step, stress and total strain rate are found through implicit spatial integration using the finite element method, based on explicit time integration using the inelastic strain rate from step 1:

$$\sigma_{t+\Delta t} = C_{t+\Delta t} : [\epsilon_t - \epsilon^T_t - \epsilon^p_t + (\dot{\epsilon}_{t+\Delta t} - \dot{\epsilon}^T_{t+\Delta t} - \hat{\epsilon}^p_{t+\Delta t})\Delta t] . \quad (2.22)$$

In these equations, $\hat{\epsilon}$ represents intermediate, estimated terms.

In the first step, total strain rates based on the known incremental displacement field calculated in the previous time step are used to update the current stress and structure parameters at each material point. Equations (2.14 - 2.21) thus constitute a system of

nonlinear equations with 15 unknowns (two tensors and three scalars) to find at every material point of a three dimensional analysis. This problem could be solved by the Newton-Raphson method [106]. With so many unknowns, however, this would be very computationally expensive. Using a similar technique to that of Lush et al [47] and Zabaras et al [48], this system of simultaneous equations was reduced to a pair of scalar equations with only two unknowns, which are more easily solved. Details of this solution procedure are given in the next section.

In the second step, the inelastic strain rate is based on the estimate in the first step. Thus, Eq.(2.22) can be regarded as a simple elastic constitutive equation with an initial strain or initial stress. The current total strain rate is found by solving the elastic constitutive equation and the system equilibrium equations using a global numerical method for spatial integration such as finite element method.

Compared with other implicit schemes [42, 45, 47, 108] for finding the inelastic strain rate, this operator-splitting, numerical-integration scheme is more efficient because the global system of equations is solved only once each time step. Implicit integration of the inelastic strain rate at each material point in the first step gives this scheme more stability than other methods, such as the explicit scheme proposed by Zienkiewicz [39].

2.3.3 The constitutive algorithm (step 1)

As pointed out above, equation (2.21) must be integrated numerically at each material point. This method used to accomplish this is called the "constitutive" algorithm or the "local" algorithm.

Substituting equations (2.8), (2.14), (2.15) and (2.19) into equation (2.21), gives :

$$\hat{\boldsymbol{\sigma}}_{t+\Delta t} = \boldsymbol{\sigma}_{t+\Delta t}^* - \sqrt{6} \mu_{t+\Delta t} f(\hat{\boldsymbol{\sigma}}_{t+\Delta t}, \hat{\mathbf{s}}_{t+\Delta t}) \Delta t \hat{\mathbf{N}}_{t+\Delta t}, \quad (2.23)$$

where

$$\boldsymbol{\sigma}_{t+\Delta t}^* = \mathbf{C}_{t+\Delta t} : [\boldsymbol{\epsilon}_t - \boldsymbol{\epsilon}_t^T - \boldsymbol{\epsilon}_t^p + (\dot{\boldsymbol{\epsilon}}_t - \dot{\boldsymbol{\epsilon}}_{t+\Delta t}^T) \Delta t] . \quad (2.24)$$

Implicit integration of equation (2.20) requires the solution of:

$$\hat{s}_{t+\Delta t} = s_t + g(\hat{\bar{\sigma}}_{t+\Delta t}, \hat{s}_{t+\Delta t}) \Delta t . \quad (2.25)$$

By taking the deviatoric part of (2.23), substituting $\hat{\boldsymbol{\sigma}}_{t+\Delta t}' = \sqrt{\frac{2}{3}} \hat{\bar{\sigma}}_{t+\Delta t} \hat{\mathbf{N}}_{t+\Delta t}$, gives:

$$[\sqrt{\frac{2}{3}} \hat{\bar{\sigma}}_{t+\Delta t} + \sqrt{6} \mu_{t+\Delta t} f(\hat{\bar{\sigma}}_{t+\Delta t}, \hat{s}_{t+\Delta t}) \Delta t] \hat{\mathbf{N}}_{t+\Delta t} = \boldsymbol{\sigma}_{t+\Delta t}^*, \quad (2.26)$$

which means that $\hat{\mathbf{N}}_{t+\Delta t}$ and $\boldsymbol{\sigma}_{t+\Delta t}^*$ have same direction. Thus,

$$\hat{\mathbf{N}}_{t+\Delta t} = \sqrt{\frac{3}{2}} \frac{\boldsymbol{\sigma}_{t+\Delta t}^*}{\bar{\sigma}_{t+\Delta t}^*}, \quad (2.27)$$

and

$$\boldsymbol{\sigma}_{t+\Delta t}' = \frac{\hat{\bar{\sigma}}_{t+\Delta t}}{\bar{\sigma}_{t+\Delta t}^*} \boldsymbol{\sigma}_{t+\Delta t}^*. \quad (2.28)$$

Combining (2.28) and (2.26) produces:

$$\hat{\bar{\sigma}}_{t+\Delta t} = \bar{\sigma}_{t+\Delta t}^* - 3 \mu_{t+\Delta t} f(\hat{\bar{\sigma}}_{t+\Delta t}, \hat{s}_{t+\Delta t}) \Delta t , \quad (2.29)$$

Equations (2.25) and (2.29) form a pair of nonlinear scalar equations with two unknowns

$\hat{\bar{\sigma}}_{t+\Delta t}$ and $\hat{s}_{t+\Delta t}$.

The constitutive algorithm of the present model proceeds as follows:

Step 1a. Calculate $\dot{\boldsymbol{\epsilon}}_t$ from the incremental displacement field at time t.

Step 1b. Calculate $\boldsymbol{\sigma}_{t+\Delta t}^*$ using equation (2.24) .

Step 1c. Calculate the deviatoric part and the effective stress of $\boldsymbol{\sigma}_{t+\Delta t}^*$ using Eqs. 2.16, 2.17.

Step 1d. Solve equations (2.25) and (2.29) simultaneously for $\hat{\bar{\sigma}}_{t+\Delta t}$ and $\hat{s}_{t+\Delta t}$

Step 1e. Calculate $\hat{\boldsymbol{\sigma}}_{t+\Delta t}$ by:

$$\hat{\boldsymbol{\sigma}}_{t+\Delta t} = \frac{\hat{\bar{\sigma}}_{t+\Delta t}}{\bar{\sigma}_{t+\Delta t}^*} \boldsymbol{\sigma}_{t+\Delta t}^* + \frac{1}{3} \text{tr}(\boldsymbol{\sigma}_{t+\Delta t}^*) \boldsymbol{\delta} .$$

Step 1f. Calculate $\bar{\boldsymbol{\varepsilon}}_{t+\Delta t}^p$ and $\hat{\boldsymbol{\varepsilon}}_{t+\Delta t}^p$ using eqs. (2.19) and (2.14).

An iterative scheme is needed in step 1c because the two equations are usually very nonlinear. Several methods [45, 47, 48, 51] maybe used to do this. In the present work, a two-level Newton-Raphson method suggested by Lush et al [47] was selected, due to its flexibility for a large class of functions f and g [48].

2.3.4 The boundary-value problem

For the quasi static process of interest, the equilibrium equations can be written as

$$\sigma_{ij,i} + b_j = 0 \quad \text{in } V, \quad (2.30)$$

in which inertia forces are neglected and b_j is a component of body forces.

The strain-displacement relation is

$$\varepsilon_{ij} = \frac{1}{2} (u_{i,j} + u_{j,i}) \quad \text{in } V . \quad (2.31)$$

The boundary conditions are

$$\mathbf{u} = \bar{\mathbf{u}} \quad \text{on } A_u, \quad (2.32)$$

$$\boldsymbol{\sigma} \cdot \mathbf{n} = \bar{\mathbf{t}} \quad \text{on } A_t \quad (2.33)$$

where V is the simulation volume region with surface A_u and A_t , $\bar{\mathbf{u}}$ and $\bar{\mathbf{t}}$ are the prescribed displacements and surface tractions respectively.

2.3.5 Finite-element implementation (step 2)

Following the standard isoparametric finite element procedure [109], the element coordinates and displacements can be approximated in terms of the corresponding nodal quantities:

$$\mathbf{x} = \sum N_i \mathbf{x}_i = [\mathbf{N}]^e \{\mathbf{x}\}^e, \quad (2.34)$$

$$\mathbf{u} = \sum N_i \mathbf{u}_i = [\mathbf{N}]^e \{\mathbf{u}\}^e, \quad (2.35)$$

where i ranges from one to the number of nodes in element e and N_i , \mathbf{x}_i , and \mathbf{u}_i are the shape function, position and displacement at element node i respectively. $[\mathbf{N}]^e$ is the shape function matrix for the element e and $\{\mathbf{x}\}^e$, $\{\mathbf{u}\}^e$ are the column vectors of the components containing the node coordinates and displacements of element e respectively.

Substituting equations (2.35) into the strain-displacement relation (2.31), the total strain vector $\{\boldsymbol{\varepsilon}\}^e$ with components $\{\varepsilon_{11}, \varepsilon_{22}, \varepsilon_{33}, \varepsilon_{12}, \varepsilon_{23}, \varepsilon_{31}\}$ for element e , is expressed as:

$$\{\boldsymbol{\varepsilon}\}^e = [\mathbf{B}]^e \{\mathbf{u}\}^e, \quad (2.36)$$

where $[\mathbf{B}]^e$ is the standard strain-displacement matrix for element e defined by spatial-differentiation of the shape functions.

Using the standard Galerkin's method [99], the governing equations and boundary conditions (2.30) - (2.33) can be transformed into the following system of algebraic equations at each node in the finite element domain:

$$\sum_{e=1}^{ne} \int_{V_e} ([B]^e)^T \{\sigma\} dV = \sum_{e=1}^{ne} \int_{V_e} ([N]^e)^T \mathbf{b} dV + \sum_{e=1}^{ne} \int_{A_{te}} ([N]^e)^T \mathbf{\bar{t}} dA , \quad (2.37)$$

in which ne is the total number of elements and the summation symbol represents the global assembly operation. $\{\sigma\}$ is a 6×1 column vector containing components of stress, $\{\sigma\} = \{\sigma_{11}, \sigma_{22}, \sigma_{33}, \sigma_{12}, \sigma_{23}, \sigma_{31}\}^T$. The above finite element equation (2.37) must be satisfied at every time in the simulation. To solve Eqs. (2.37), the time integration scheme in Eq. (2.22) and strain-displacement Eq. (2.36) are used to evaluate the time-dependent, nonlinear constitutive equations:

$$\begin{aligned} & \sum_{e=1}^{ne} \int_{V_e} ([B]^e)^T [C]_{t+\Delta t} [B]^e dV \{\Delta u\}_{t+\Delta t} = \\ & \sum_{e=1}^{ne} \int_{V_e} ([B]^e)^T [C]_{t+\Delta t} (\{\hat{\epsilon}^p\}_{t+\Delta t} + \{\dot{\epsilon}^T\}_{t+\Delta t}) \Delta t dV - \sum_{e=1}^{ne} \int_{V_e} ([B]^e)^T [C]_{t+\Delta t} \{\epsilon^e\}_t dV + \\ & \sum_{e=1}^{ne} \int_{V_e} ([N]^e)^T \mathbf{b} dV + \sum_{e=1}^{ne} \int_{A_{te}} ([N]^e)^T \mathbf{\bar{t}} dA . \end{aligned} \quad (2.38)$$

Here $[C]_{t+\Delta t}$ contains components of the 4th-order elastic tensor \mathbf{C} at time $t+\Delta t$, and is a 6×6 matrix for three dimensions. It should be pointed that $\{\Delta u\}_{t+\Delta t}$ contains incremental displacements, while \mathbf{b} and $\mathbf{\bar{t}}$ contain the total body force components and boundary traction components respectively. This mixed form in Eq. (2.38) avoids the phenomenon that solutions gradually shift away from equilibrium, which occurs with purely incremental forms [43]. In addition, this form allows easy implementation of moving internal boundary conditions without special treatment [58]. Second-order Gaussian quadrature is used to numerically integrate eqs. (2.38) [43], which are assembled into a set of linear equations with a banded, symmetric coefficient matrix or "global stiffness matrix" on the left hand side. This system is solved for $\{\Delta u\}_{t+\Delta t}$ using the Cholesky method [110]. Next, $\{u\}_{t+\Delta t}$ are updated, the current strain $\{\epsilon\}_{t+\Delta t}$ and stress $\{\sigma\}_{t+\Delta t}$ are calculated by equations (2.36) and (2.22). The inelastic strains $\{\epsilon^p\}_{t+\Delta t}$ needed for the calculations are taken from the previous solution

of Eq. (2.21) at each numerical integration point using the procedure discussed in section 2.3.3.

2.3.6 Treatment of liquid elements

To avoid complicated remeshing procedures [4] , the present model uses a “fixed-grid” approach. The simulation domain includes both solid and liquid elements, so special treatment is needed. Three approaches were implemented and compared in the present work. The first was to model liquid elements by simply altering the temperature-dependent mechanical properties. Rearranging equation (2.7),

$$\sigma_{ij} = -p\delta_{ij} + 2\mu\epsilon_{ij}^e, \quad (2.39)$$

$$\text{where } p = -K\epsilon_{kk}^e = -(\lambda + 2\mu)\epsilon_{kk}^e. \quad (2.40)$$

The bulk modulus K , Lamé constants λ and μ are related to Young's modulus E and the Poisson ratio ν by:

$$K = \frac{E}{1-2\nu}, \quad (2.41)$$

$$\lambda = \frac{E\nu}{(1+\nu)(1-2\nu)}, \quad (2.42)$$

$$\mu = \frac{E}{2(1+\nu)}. \quad (2.43)$$

The most popular method to treat liquid elements is to simply reduce E by several orders of magnitude as temperature increases from the solidus to the liquidus temperature. Being easily deformable (small μ) and compressible (small K) avoids any mechanical influence of the liquid on the solid. This is physically reasonable when modeling, for example, 2-D generalized-plane strain sections through castings where the liquid outside the section is exposed to ambient pressure p [9, 111]. To further model effect of hydrostatic

pressure generation in the liquid on the solidifying shell, the bulk modulus in the liquid can be maintained on the same order as that in the solid by appropriately increasing ν to approach 0.5 (large K) simultaneously with the decrease in E [19, 24, 28, 112, 113].

With either implementation of this method, thermal strain and inelastic strain in the liquid elements are set to zero, and non-physical elastic strains were produced. These generated huge non-physical stresses after the transition from liquid to solid, if the temperature-dependency of the elastic constants was properly accounted for via the $\dot{T} \frac{\partial C}{\partial T} \epsilon^e$ term in Eq.(2.9). This problem could be avoided by neglecting this term, but the later behavior of the solid was changed significantly. The second problem with this method was numerical ill-conditioning. A singular stiffness matrix sometimes arose when Young's modulus in the liquid elements was too small relative to that of the solid.

The second method to treat liquid in the present work was simply to reset the elastic strain of all liquid elements to zero at the end of every time step. This avoids both problems of the previous method, but requires setting up cumbersome flags in the program.

A third method, which solves all of the above problems by avoiding drastic change of the elastic constants altogether, is to allow increased inelastic strain in the liquid instead. This method was implemented in the present work by creating a viscoplastic constitutive relation for the liquid phase in the form of a penalty function which generated inelastic strain in proportion to effective stress in the liquid. This avoids shear stress in the liquid, while transmitting hydrostatic stress. This method takes advantage of the robust algorithm for handling inelastic strain presented earlier.

It should be pointed out that the elastic strain in the first two methods and inelastic strain in the third method are treated as structure parameters which should be reset to their initial values in the new phase (solid), after phase transformation has occurred. The effect of hydrostatic pressure in the liquid due to gravity was incorporated into the second and third

methods in order to simulate continuous casting. This was done by applying the pressure as an internal constraint condition to appropriate nodes near the solid-liquid interface [9].

2.3.7 Two-dimensional models

Section (2.3.1)-(2.3.5) described a general three-dimensional computational framework for modeling the mechanical behavior of systems with temperature and rate-dependent material behavior. However, it is of great interest to use reliable two-dimensional models for computational efficiency. Four different two-dimensional assumptions including plane-stress, plane-strain, generalized-plane-strain and plane-deformation conditions have been implemented into a finite-element model called CON2D coded in FORTRAN. Special aspects of the implementation of these models will be discussed here, as further details can be found elsewhere [43, 99].

In three dimensions, the matrix form of equation (2.7) Hook's law is

$$\{\sigma\} = [C]\{\epsilon^e\}, \quad (2.44)$$

where $\{\sigma\}$ is a 6x1 component vector for stress, $\{\sigma\} = \{\sigma_{11}, \sigma_{22}, \sigma_{33}, \sigma_{12}, \sigma_{23}, \sigma_{31}\}^T$, $\{\epsilon^e\}$ is a 6x1 component vector for elastic strain, $\{\epsilon^e\} = \{\epsilon_{11}^e, \epsilon_{22}^e, \epsilon_{33}^e, \epsilon_{12}^e, \epsilon_{23}^e, \epsilon_{31}^e\}^T$, and $[C]$ is a 6x6 elastic matrix. By deleting the stress and strain components which vanish in two dimensions, these quantities simplify to $\{\sigma\} = \{\sigma_{xx}, \sigma_{yy}, \sigma_{xy}, \sigma_{zz}\}^T$, $\{\epsilon^e\} = \{\epsilon_{xx}^e, \epsilon_{yy}^e, \epsilon_{xy}^e, \epsilon_{zz}^e\}^T$, and

$$[C]_{4 \times 4} = \frac{E}{(1+\nu)(1-2\nu)} \begin{bmatrix} (1-\nu) & \nu & 0 & \nu \\ \nu & (1-\nu) & 0 & \nu \\ 0 & 0 & \frac{(1-2\nu)}{2} & 0 \\ \nu & \nu & 0 & 1-\nu \end{bmatrix}, \quad (2.45)$$

where E is the temperature-dependent Young's modulus and ν is Poisson ratio. For plane-stress ($\sigma_{zz} = 0$) and plane-strain ($\epsilon_{zz} = 0$) conditions, $[C]$ may further simplified to a 3×3 matrix to evaluate the element stiffness matrix terms for Eq. (2.38). To evaluate the element “forces” contributed from thermal strain and inelastic strain using the initial strain method, care should be made to incorporate the influences of thermal and inelastic strains in the undiscretized z dimension on the in-plane equilibrium equation.

The third condition, generalized-plane strain, assumes strain in the third direction is constant ($\epsilon_{zz} = a$) over the entire simulation domain. The fourth condition, plane-deformation assumes strain in the z direction is a linear function of the in-plane coordinates:

$$\epsilon_{zz} = a + bx + cy. \quad (2.46)$$

For both generalized-plane-strain and plane-deformation conditions, strain-related unknown variables (a, b, c) are coupled with the in-plane displacements and must be solved together with the global system of equations over the entire domain. Thus, a mixed finite-element formulation of displacements and strain-related variables is used for both conditions. The associated element strain-displacement matrix $[B]^e$, defined in Eq. (2.36) also must be modified accordingly.

For the finite-element implementation of the generalized-plane-strain condition, the additional degree of freedom, a , is shared by each element in the domain. Thus, the modification of $[B]^e$ generates an additional equation to the in-plane equilibrium equations already being satisfied:

$$\int \sigma_{zz} dA = F_z. \quad (2.47)$$

Here F_z is an external mechanical force acting in the undiscretized (z) direction which must be specified as a contribution to the RHS of Eq. (2.38). Furthermore, F_z is set to zero to model a slice through a long unconstrained body. This condition is appropriate for thermal

stress problems with symmetrical domains, properties, and boundary conditions in both in-plane directions.

For plane deformation, two additional equations and degrees of freedom are generated:

$$\int \sigma_{zz} y \, dA = M_x , \quad (2.48)$$

$$\int \sigma_{zz} x \, dA = M_y , \quad (2.49)$$

M_x and M_y are in-plane external mechanical moments which act in the x and y directions respectively, and are specified in the same manner as F_z . Because the new degrees of freedom are coupled with every other degree of freedom in the plane, the additional terms generated in Eq.(2.38) produce non-zero terms in the shape of an "arrowhead" in the global stiffness matrix [98]. This damages the banded nature of this matrix, which may significantly increase computation time for some banded solution algorithms. To overcome this problem, a variable-bandwidth Cholesky solver was used as a "direct method" to solve the system of linear equations [114]. This skyline solver stores the non-zero symmetric portion of each row of the banded, symmetric, positive-definite, coefficient matrix in a one-dimensional array.

An alternative method has been implemented to overcome the arrowhead-shape problem for generalized-plane-strain conditions. This method partitions global system Eq. (38) into parts, which are solved using iteration. The first part of the equations is very similar to the equations generated in the plane-strain model except considering influence to the force from strain ϵ_{zz} . The second part of equation is the discretized equilibrium equation in the z direction Eq. (2.47). Assuming initial ϵ_{zz} is zero, this "iteration method" solves the first part of the equation for the in-plane incremental displacements using the constant-bandwidth Cholesky solver. Then, ϵ_{zz} is adjusted using the second part of the equations. These steps are repeated until convergence [58].

2.4 Model validation and examples

To verify the proposed finite element system and its FORTRAN implementation, several typical problems with known solutions have been solved by the CON2D model. All simulations were performed on a Silicon Graphics IRIS 4D / 25 workstation with 16 MBytes of RAM. Each problem was chosen to be a numerically challenging test of one or more of the phenomena present in a solidifying body, as modeled with a 2-D thermal elastic-viscoplastic generalized-plane-strain section. Some of these examples are reported here.

2.4.1 Cantilever beam with mechanical load

This problem tested the ability of the model to calculate displacement and stress under simple mechanical loading. The problem illustrated in Figure 2.2 is an isothermal, elastic, 0.1 x 1.2 x 4.8 m cantilever beam with a static 400 N/m parabolic shear load distribution at the tip. From beam theory, the deflection at tip (point B) is 0.03583m while the axial stress at point A is 600 MPa, with $E = 300$ GPa and $\nu = 0.25$.

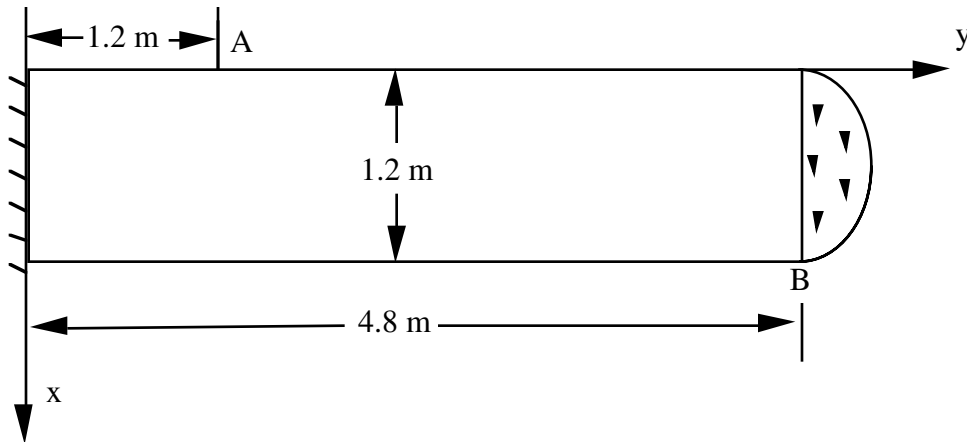


Figure 2.2 Cantilever beam with shear load (test problem 1)

A uniform 5 x 9 (45 nodes) mesh was used to discretize the 1.2 x 4.8 m domain under plane stress. With 64 three-node triangular elements, tip deflection was 0.00337 m (5.3% error), while the axial stress at point A was 537 MPa (-10.7% error). With 16 six-node

isoparametric triangular elements, tip deflection error decreased to -0.9% (0.03528m) while the axial stress error decreased to -3.8% (577 MPa). It is obvious that six-node isoparametric elements produce much better accuracy than three-node elements for the same number of nodes, as reported by others [115].

2.4.2 Thermal loading of a plate with temperature-dependent shear modulus

This problem tested the capability of the model to handle both thermal strains and non-homogeneous material properties. As shown in Figure 2.3, a 4 x 1 m thermoelastic plate in plane strain with a linear temperature-dependent shear modulus, $\mu = (7956.83 - 15.2373 \times T)$ MPa, was subjected to a linear temperature variation in the y direction increasing from initial 0°C to a final distribution of $T = 100 - 95(1-y)$ constrained in the x direction. Other constant material properties include $\nu = 0.3$ and thermal expansion coefficient, $\alpha = 0.125 \times 10^{-4} (^\circ\text{C})^{-1}$.

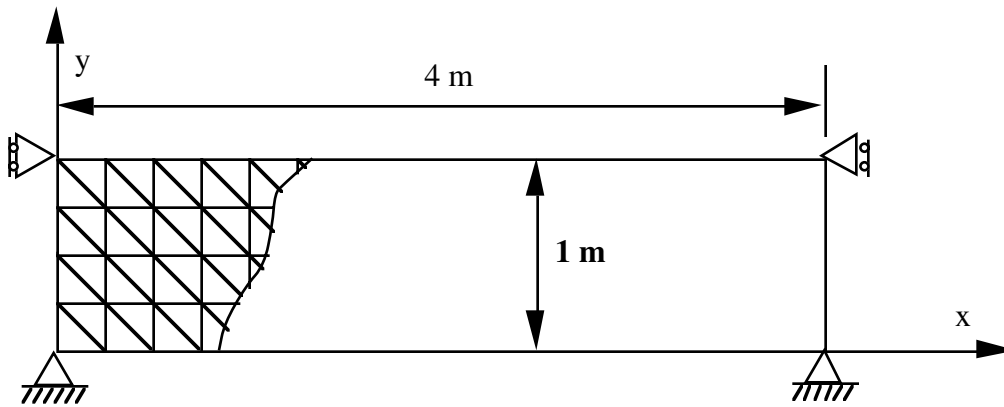


Figure 2.3. Finite-element model of plate with temperature-dependent shear modulus

An analytical solution from Sladek [116] yields $\sigma_x = -2\alpha \frac{1+\nu}{1-\nu} \mu T$, where σ_x reaches -362.4 MPa at the upper side ($x=0$).

The finite-element model with a uniform 17 x 5 (105 nodes) mesh produced σ_x at the upper side of -389.8 (7.6% error) for 64 three-node elements and -365.9 (1.0% error) for 16 six-node elements. Although the three-node triangular element solution for this non-homogeneous problem is within engineering accuracy with this coarse mesh, it is outperformed by the six-node triangular element, which assumes a linear stress distribution appropriate for the linear variation of material properties in this problem.

2.4.3 Unconstrained elastic pipe under thermal loading in generalized plane strain

This problem was selected to verify the ability of the model to handle two-dimensional geometry and generalized-plane-strain constraint under thermal loading. The inner surface temperature of a long hollow cylinder is increased from zero to T_0 while keeping the outer surface temperature at zero, produces the steady state temperature field $T(r)$

$$T(r) = \frac{T_0 \ln \frac{r}{b}}{\ln \frac{a}{b}}. \quad (2.50)$$

From general thermoelasticity theory, this unconstrained hollow cylinder has axial strain ϵ_{zz} as

$$\epsilon_{zz} = \frac{2\alpha \int_a^b T(r) r dr}{b^2 - a^2} = \frac{\alpha \iint T(r) dA}{A}, \quad (2.51)$$

in which b is the outer radius, a is the inner radius, A is the cross-sectional area, and material properties are constant. For $b = 0.25\text{m}$, $a = 0.16\text{m}$, $E = 20 \text{ GPa}$, $\nu = 0.3$, $T_0 = 100^\circ\text{C}$, $\alpha = 0.00005$, ϵ_{zz} is 8.528×10^{-4} .

For finite element analysis, one quarter of a transverse section was modeled using a uniform 21 x 11 (231 nodes), two-dimensional rectangular-Cartesian mesh of 100 six-node elements under generalized plane strain, as shown in Figure 2.4. Two methods for solving the generalized plane strain problem were compared. The direct method generated $\epsilon_{zz} = 8.530 \times 10^{-4}$ (0.023% error) and used 2.8s CPU time, while the iteration method produced $\epsilon_{zz} =$

8.593×10^{-4} (0.762 % error) after 5 iterations, using 3.8s CPU time on the same machine. Because the direct method required less CPU time with better accuracy, it was selected for all further analysis with generalized-plane-strain.

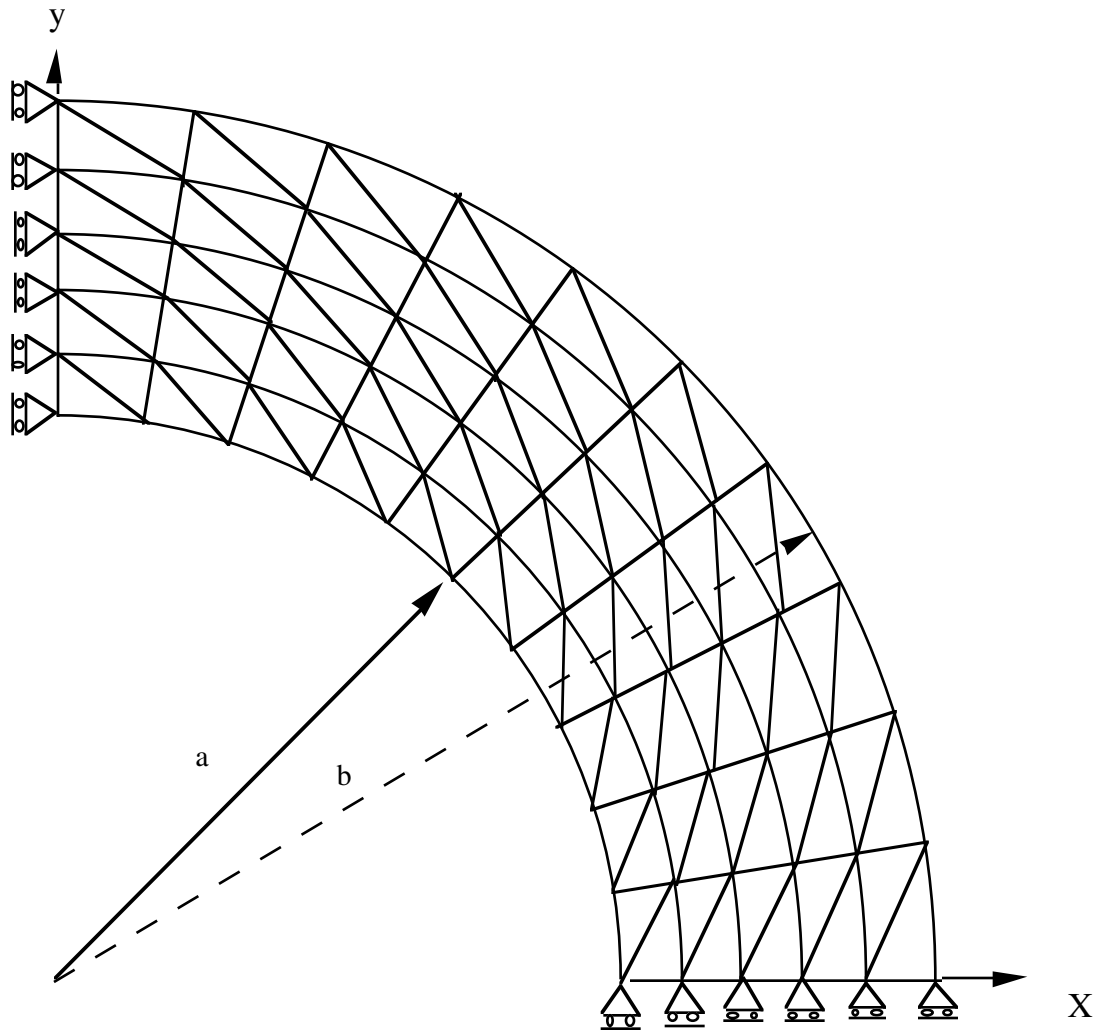


Figure 2.4. Finite element model of heated elastic hollow cylinder (test problem 3)

2.4.4 Stress in a solidifying slab

Weiner and Boley developed an exact analytical solution of thermal stresses during 1-D solidification of a slab with temperature-dependent, rate-independent, elastic-perfectly-plastic material behavior [1]. Here, this problem was transformed into a challenging benchmark test problem for thermal-mechanical analysis of solidification using an elastic-

viscoplastic constitutive equation. Both the finite element model developed in this work (CON2D) and the commercial finite element package, ABAQUS, were used applied to solve this problem. In addition, several important computational factors including element size, time step size, stress state in the undiscretized direction, and CPU time were investigated, in the context of this “solidification test problem”.

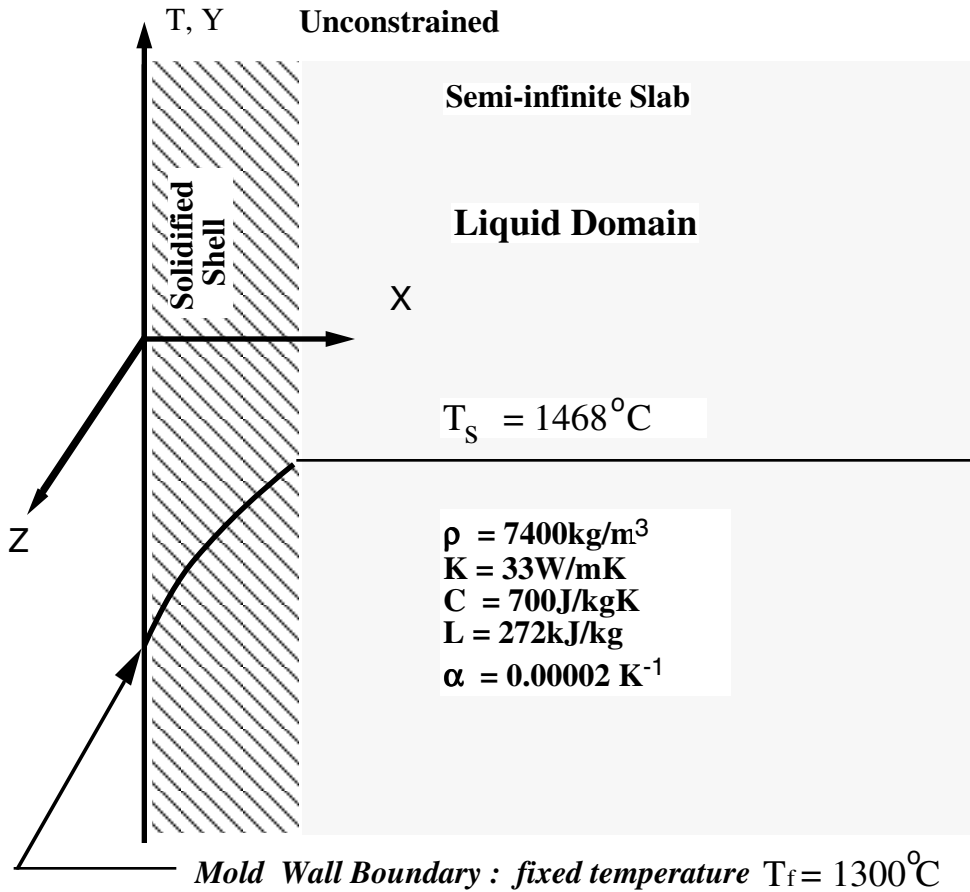


Figure 2.5 Chilled slab with one-dimensional solidification

2.4.4.1 Analytical solution

As shown in Figure 2.5, the problem involves one-dimensional solidification (x direction) in a semi-infinite domain. Initially, the domain contains liquid at a uniform temperature equal to the unique solidification temperature, T_s . At time $t = 0$, the surface ($x=0$)

is suddenly chilled to T_f . The elastic-perfectly-plastic constitutive behavior includes a yield stress σ_Y , which decreases linearly from 20 MPa at T_f to zero at T_s as shown in Figure 2.6.

Other thermal and mechanical properties are constants based on steel properties used by Kristiansson [93] : $\rho = 7400 \text{ kg/m}^3$, $c = 700 \text{ J/kgK}$, $K = 33 \text{ W/mK}$, latent heat $L = 272 \text{ kJ/kg}$, $T_s = 1468^\circ\text{C}$, $T_f = 1300^\circ\text{C}$, $\nu = 0.35$, $\alpha = 0.00002 \text{ K}^{-1}$, $E = 40 \text{ GPa}$.

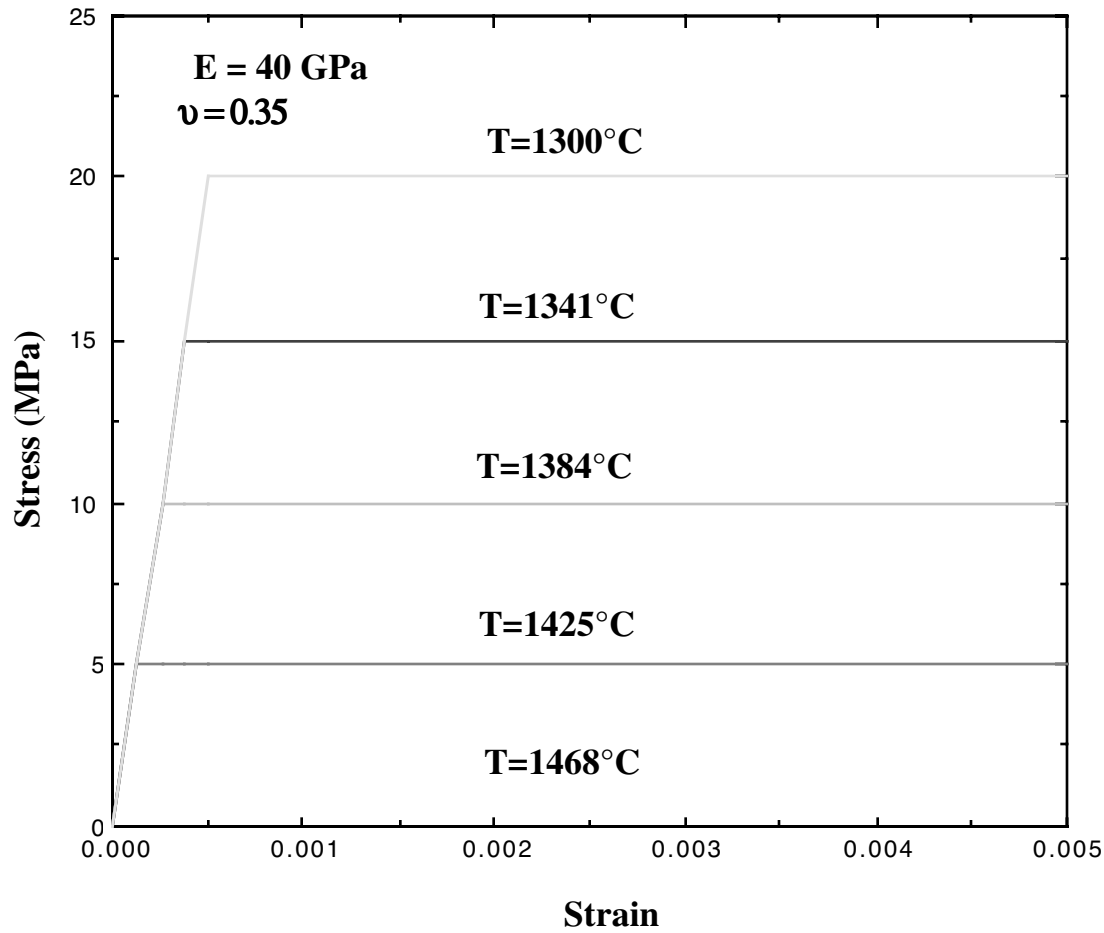


Figure 2.6 Constitutive behavior assumed in solidification test problem

The transient temperature distribution and the solidified shell thickness for this Stefan problem can be found in Carslaw [117]. It is illustrated in Figure 2.8 at several different times. Stress across the solidified shell is given by Weiner and Boley [1] assuming generalized plane strain in both the y and z directions. The transverse stresses σ_y , σ_z are equal and vary with x while all other components of stress are zero.

2.4.4.2 Numerical solution

The present finite-element model was used to analyze this one-dimensional solidification test problem using the two-dimensional domain and mesh pictured in Figure 2.7. Generalized plane strain was assumed in both y and z directions. This stress state was implemented in the y direction by imposing the constraint that the vertical displacements u_y are equal along the top side of the domain.

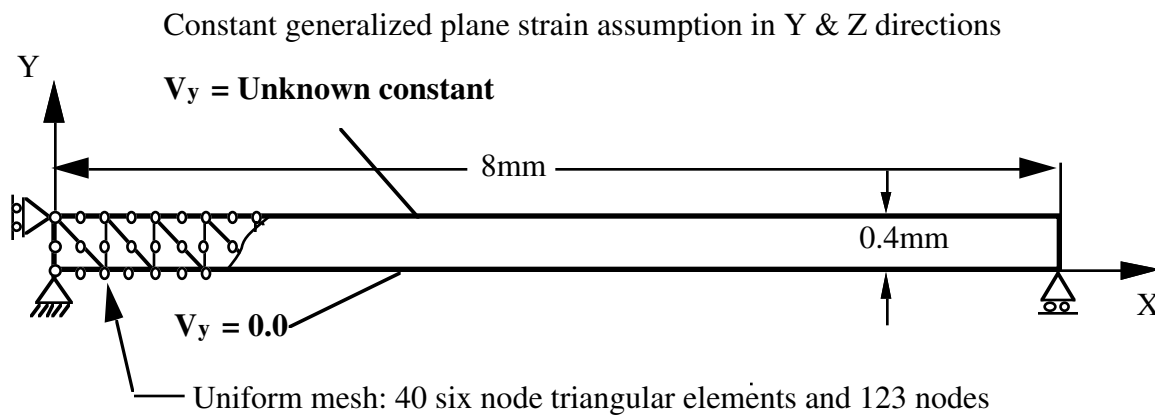


Figure 2.7 Finite element model of solidification test problem

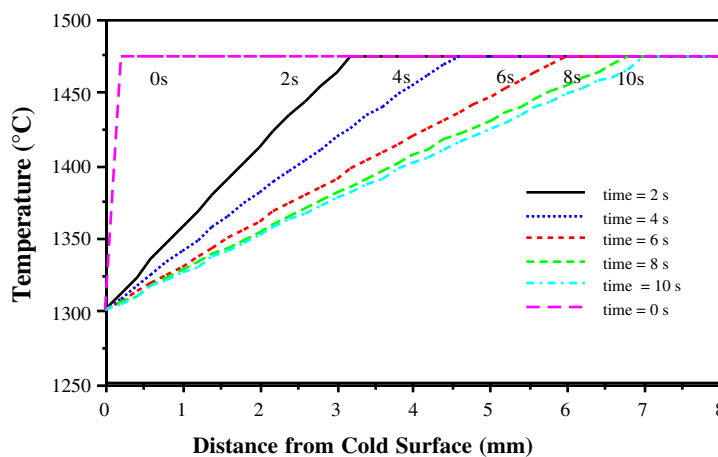


Figure 2.8 Temperature distribution in solidification test problem from analytical solution

The elastic-perfectly-plastic constitutive model of this present problem was transformed into an elastic-viscoplastic model using the following nonlinear rate equation for the inelastic strain rate,

$$\dot{\epsilon}^p = f(\bar{\sigma}, s) = A [\max(\bar{\sigma}, \sigma_Y) - \sigma_Y]^n, \quad (2.52)$$

in which $A = 1.0 \times 10^8$, $n = 5.0$. This equation is a penalty function to ensure that rapid inelastic strain occurs until the proper stress is achieved. Although a first order power law with a very large fluidity constant A can accurately characterize the rate-independent material behavior [118], large n is used in order to increase the non-linearity and consequent numerical difficulty of the problem. This formulation of the problem is a particularly rigorous test of the numerical algorithms, due to the severe nonlinear nature of equation (52).

To compare the numerical and analytical solutions, the relative error in norm L_2 is defined as

$$L_2 = \left(\frac{\sum |\sigma_{zn} - \sigma_{za}|^2}{\sum |\sigma_{za}|^2} \right)^{1/2}, \quad (2.53)$$

in which Σ sums from 1 to the total number of nodes in the simulation domain, σ_{zn} represents z stress from the numerical model (undiscretized direction), σ_{za} is z stress from the analytical solution.

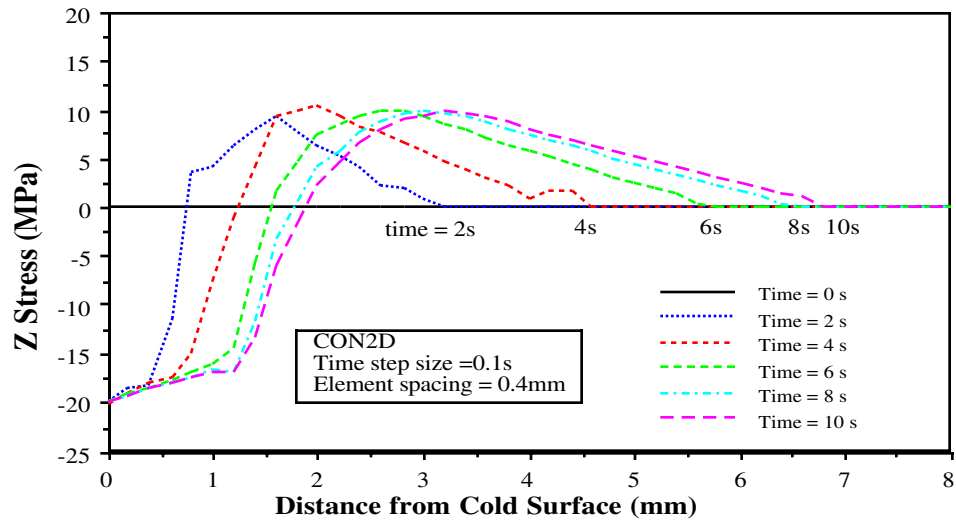


Figure 2.9 Stress distribution through slab from elastic-viscoplastic finite element solution (solidification test problem)

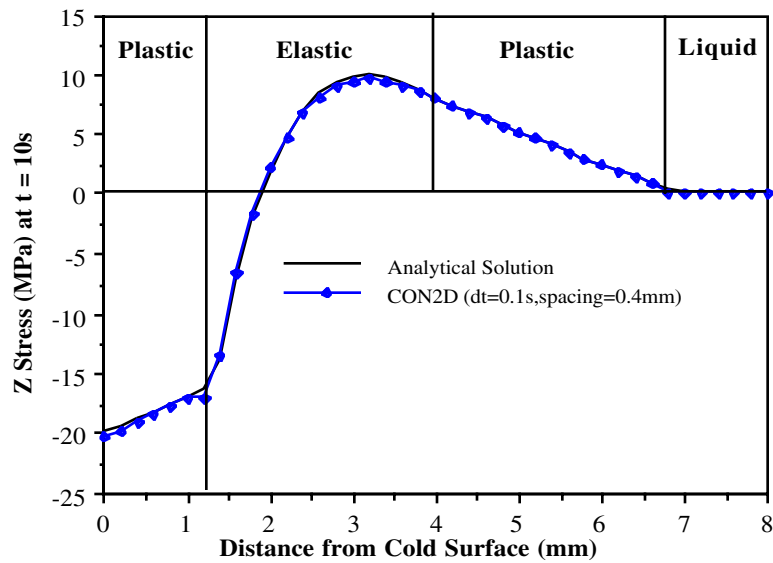


Figure 2.10. Comparison of analytical solution and elastic-viscoplastic finite element solution of solidification test problem

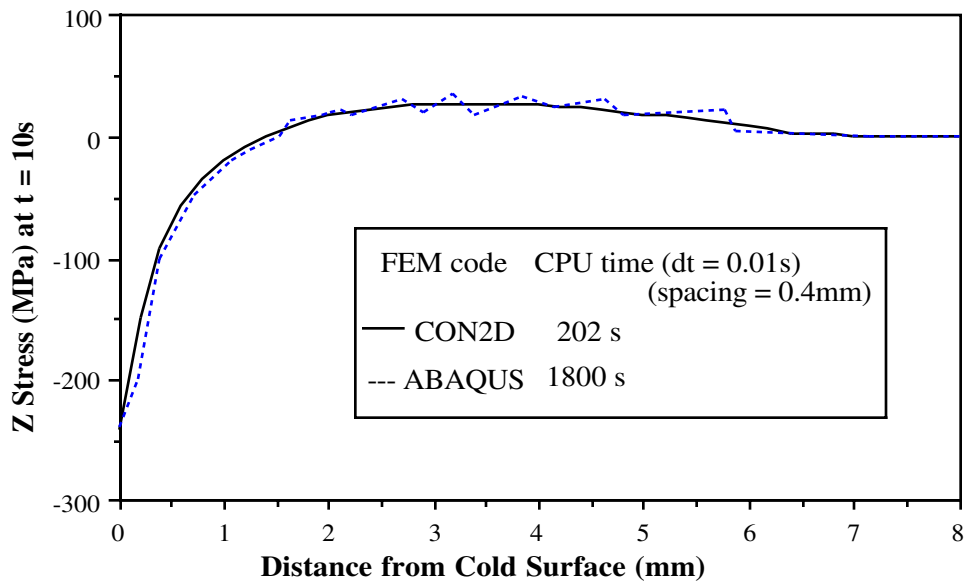
The 8.0 x 0.4 mm domain was modeled for 10s using 40 six-node triangular elements (41 x 3 nodes) and a constant time step size of 0.1s. The σ_z distributions corresponding to the times in Figure 2.8 are shown in Figure 2.9. With the generalized plane strain state, it is clear that compression appears on the cold surface while tension arises near the solid / liquid interface. This pattern enlarges as the shell grows. Note that force balances require the average stress through the slab to equal zero. The σ_z stress distribution from the numerical model at $t = 10$ s is compared to the analytical solution in Figure 2.10. The relative error is 3.7% at $t = 10$ s while CPU time is 22s for the CON2D model. Both methods proposed in this paper to treat liquid elements produced the same results with roughly the same CPU time.

2.4.4.3 Comparison with commercial package ABAQUS

To further evaluate the efficiency of the present model, this solidification test problem was solved using ABAQUS. At first, the elastic-perfectly-plastic constitutive behavior was simulated using standard elastic-plastic constitutive equation by treating the liquid elements to have a very small yield stress. However, convergence was never reached even with a prohibitively small time step. Further investigation on a single element test problem, with temperature-dependent yield stress, revealed that once the yield stress in one element changes by more than 100%, the fully implicit Newton-Raphson solution algorithm of ABAQUS is divergent. Thus, this method is unsuitable for stress analysis with solidification, which always involves large increases in yield stress, as hot solid cools. To get around this problem, other researchers have used ABAQUS to approximate the solution to solidification stress problems such as these, by invoking an arbitrary, non-physical "cut-off" temperature to completely ignore stress generation in all elements above the cut-off temperature [119].

Next, ABAQUS was used to solve a simple elastic version of the test problem by ignoring inelastic strain. This also failed before a user subroutine was created to simultaneously ignore the $\dot{T} \frac{\partial \mathbf{C}}{\partial T}$ term in Eq.(9) and change the temperature-dependent elastic

constants of liquid elements to avoid shear stress [113]. A comparison of the results from ABAQUS and the present model for this problem is given in Figure 2.11. Both simulations used the same time step size (0.01s) and mesh size (0.4 mm spacing). Although the stress distributions from both programs match, the CPU time with ABAQUS is nearly 9 times that of the model developed in the present work. Furthermore, the CPU time required by CON2D to solve the full solidification test problem, including the highly nonlinear rate-dependent constitutive behavior, increased only 20% over the linear-elastic problem from 2002s to 2200s.

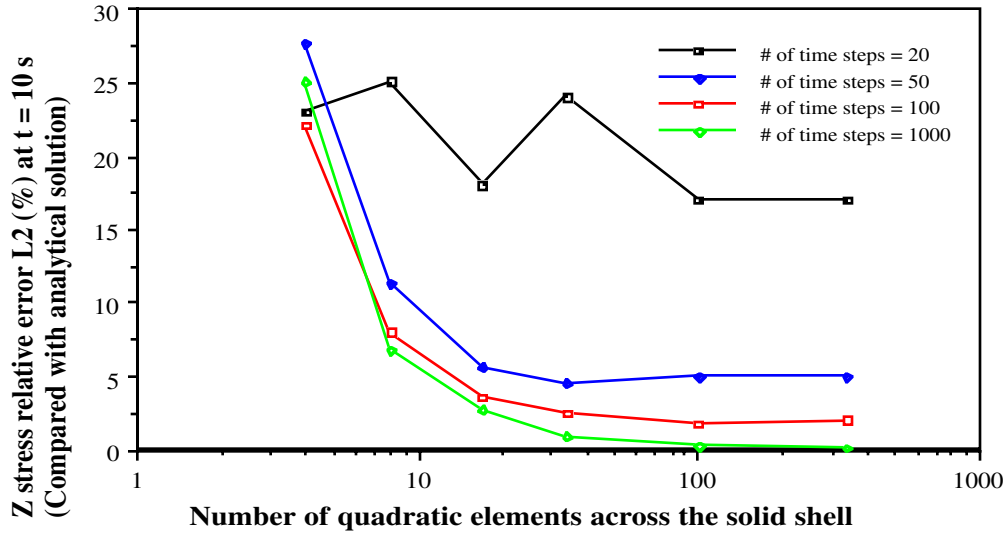


2.11 Comparison of elastic finite element approximations of solidification test problem

2.4.4.4 Effect of time step and mesh size

The solidification test problem in 2.4.4.2. was next used to study the influence of time-step size and mesh refinement on the accuracy. Twenty-four simulations were performed, using four different time step sizes: 0.5s, 0.2s, 0.1s and 0.01s, and six different meshes: 11 x 3 mesh with 33 nodes and 10 six-node elements, 21 x 3 mesh with 63 nodes and 40 six-node

elements, 41 x 3 mesh with 123 nodes and 80 six-node elements, 81 x 3 mesh with 243 nodes and 80 six-node elements, 241 x 3 mesh with 723 nodes and 480 six-node elements, 801 x 3 mesh with 2403 nodes and 1600 six-node elements. The relative error criterion of equation (54) was again adopted, using z stress results at $t = 10$ s.



Figure

2.12 Effect of mesh refinement and time step size on relative error for solidification test problem

The effects of different mesh size and time step size on error can be seen in Figure 2.12. Accuracy generally improves with refinement of both time step size and element size, except for very coarse meshes (i.e., 11 x 3 mesh) and very large time step sizes (i.e., 0.5s) which have erratic results. For any other time step size, the error decreases very fast with initial refinement of element size (i.e., from 11 x 3 mesh to 41 x 3 mesh). With continued refinement, accuracy passes through an optimum and then improves very little or even worsens. It is likely that every given mesh size has an inherent limit in achievable accuracy and an optimum time step size associated with it [120]. A similar conclusion can be made for the refinement of mesh size. Thus, to get a specified accuracy, there is an optimum combination of element size and time step size. For a error of 3.7%, the 40 x 3 mesh (17 six

node element across the shell) with 0.1s time step size (100 time steps) is a cost-effective combination to solve the solidification test problem in 2.4.4.2.

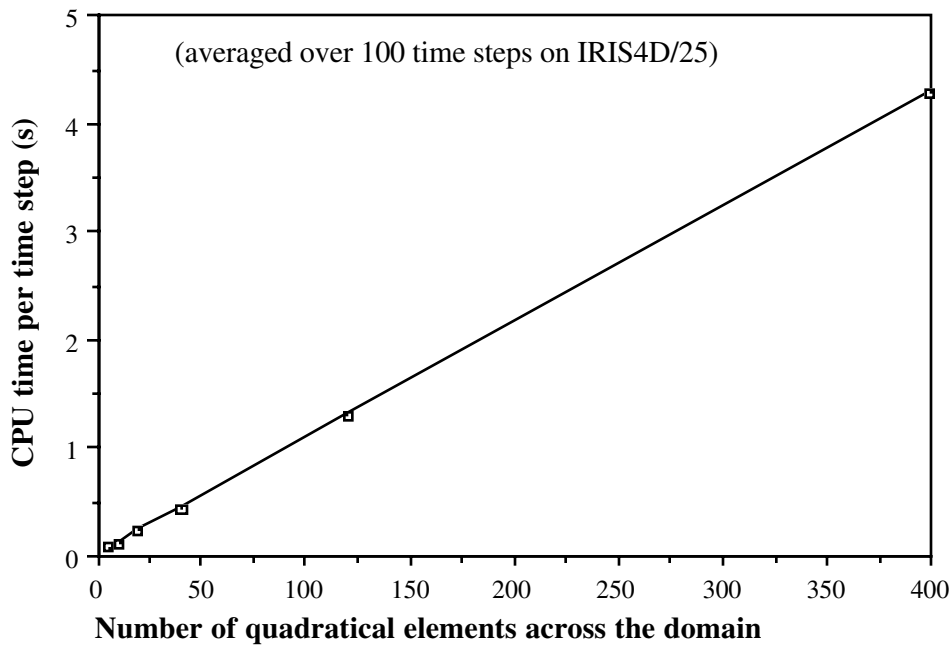


Figure 2.13 Variation of computational cost with mesh refinement

As shown in Figure 2.13, the CPU time per time step is a linear function of the number of elements in the mesh when the problem is essentially one-dimensional and all mesh patterns have same the band width of the stiffness matrixes and optimal node numbering. To decrease the relative error from 3.7% to 0.1%, total CPU times increases from 22 seconds to 4280 seconds.

It should be pointed out that many stress models of solidification processes in previous literature appear to have used very coarse mesh sizes (similar or coarser than the 11 x 3 mesh). This likely has led to large errors or possibly even an unrealistic stress solution. A previous investigation comparing mesh and time step effects on the accuracy of heat transfer simulations with solidification [120] reported that with 11 nodes across the

solidification direction, the “average absolute error” was less than 0.1 % after 100 time steps. The stress results with this mesh and time step size produce a 26 % relative error. Thus, for coupled thermal-mechanical analysis involving solidification, a much finer mesh is required for the mechanical model, in order to get accuracy similar to that of the corresponding heat transfer analysis. At least 21 nodes across the solidifying shell are suggested, in order to achieve engineering accuracy within 10 % relative error.

2.4.4.5 Effect of two-dimensional stress state

To examine the effect of stress state in the undiscretized z direction on the calculated stresses, four different 2-D stress states were investigated: plane stress, plane strain, generalized plane strain and plane deformation. Other conditions of the solidification test problem were kept the same, including the generalized plane strain condition in the y direction, imposed by constraint equations. The minimal effect of stress state on the in-plane y stress can be seen in Figure 2.14. As expected, z stresses from the different stress states are completely different as shown in Figure 2.15.

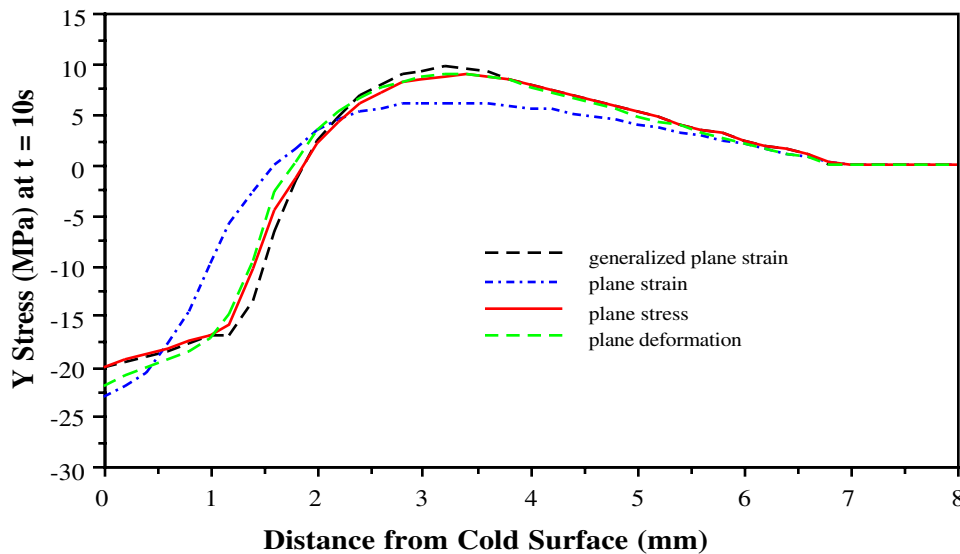
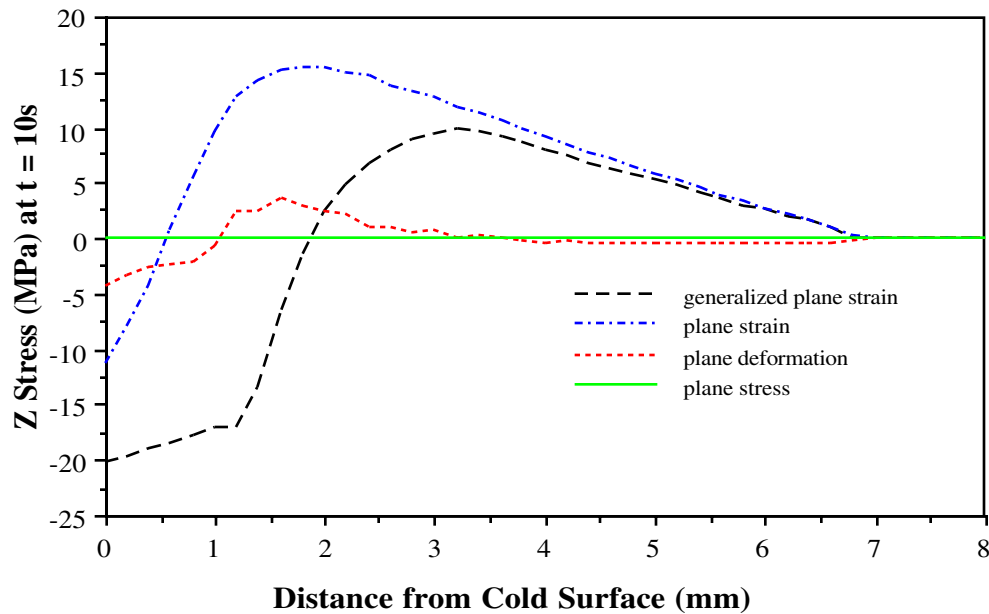


Figure 2.14 Effect of out-of-plane assumption on y stress for solidification test problem



F

Figure 2.15 Effect of out-of-plane assumption on z stress for solidification test problem

For solidification problems involving two-fold symmetry, such as long castings with rectangular cross-sections, the most appropriate stress state is generalized plane strain, assuming that friction against the mold walls and other axial forces are negligible. When modeling without exploiting symmetry, plane deformation is always appropriate. It is important to note, however, that a plane deformation analysis produces different results than generalized plane strain when two-fold symmetry is exploited by modeling only one quarter of the domain. Using the same logic, either b or c in eq. (46) should be set to zero when modeling half of a casting with a single symmetry plane, as appropriate. The traditional stress state of plane stress appears to be quite reasonable for the in-plane behavior.

2.4.4.6. Realistic constitutive behavior

Having validated the model, the solidification test problem of 4.2.2 was modified to include realistic constitutive behavior for solidifying plain-carbon steel using the rate-dependent elastic-viscoplastic model III of Kozlowski et al [105]. This model was developed to match tensile test results of Wray [121] and creep data of Suzuki [122] over a wide range of strain rates, high temperatures, and carbon contents (%C) relevant to continuous casting conditions:

$$\dot{\bar{\epsilon}}^p = f(\bar{\sigma}, s) = f_c * \exp\left(-\frac{Q}{T}\right) * (\bar{\sigma} - f_1 \bar{\epsilon}^p f_2)^{f_3-1}, \quad (2.54)$$

where $Q = 44650$,

$$f_c = 4.655 \times 10^4 + 7.14 \times 10^4 (\%C) + 1.2 \times 10^5 (\%C)^2,$$

$$f_1 = 130.5 - 5.128 \times 10^{-3} T,$$

$$f_2 = -0.6289 + 1.114 \times 10^{-3} T,$$

$$f_3 = 8.132 - 1.54 \times 10^{-3} T.$$

The σ_z stress results of a CON2D simulation using a 41 x 3 mesh and 0.1s time step size are shown in Figure 2.16. Compared with Figure 2.9, it can be seen that both figures have same qualitative stress distribution. However, the stresses in Figure 2.16 are lower in magnitude and have a different shape. Including phase transformations further changes the stress pattern, and depends on the treatment of the thermal expansion and inelastic strain that occurs during the transformation [9].

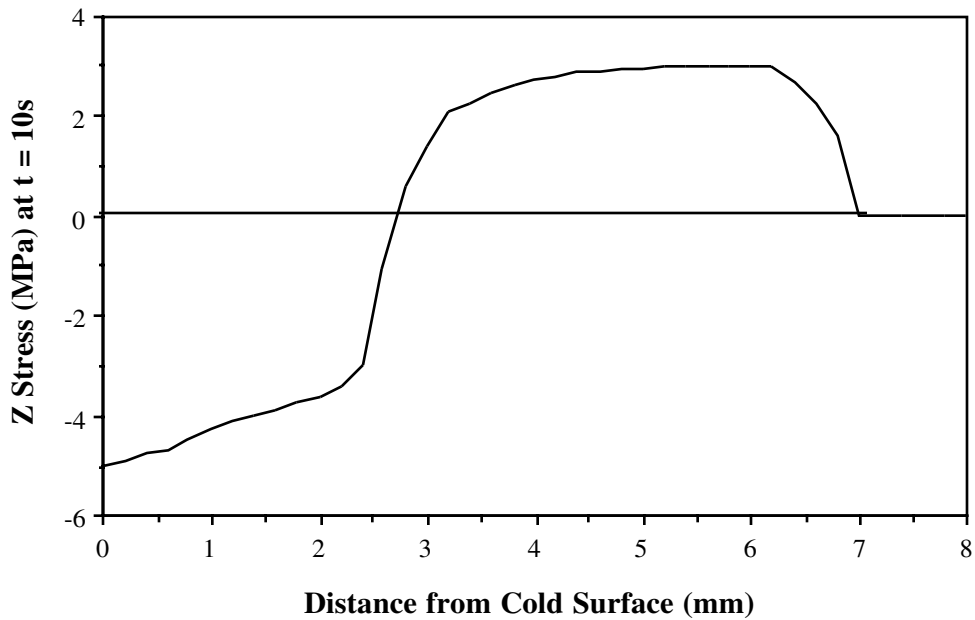


Figure 2.16 Stress distribution with realistic (steel) constitutive equation for solidification test problem

2.5 Summary and conclusions

A two-dimensional fixed-grid finite element model of thermal-mechanical behavior within solidifying bodies has been developed. This model features a robust numerical scheme to handle the highly-nonlinear unified constitutive equations employed to describe high-temperature mechanical behavior and appropriate two-dimensional assumptions to properly simplify the three-dimensional system. The mathematical consistency of the model has been verified using several known solutions. Based on this investigation, several conclusions can be made regarding stress analysis with solidification:

1) Fixed-grid methods present special numerical difficulties which require careful consideration:

a) liquid can be handled using one of several different methods.

b) accuracy in the undiscretized direction can be improved by choosing the appropriate condition. Generalized plane strain is best solved with a direct method using a variable band-width solution algorithm.

c) the additional term in the rate formulation of the constitutive equation due to temperature-dependency of the elastic modulus is important.

d) highly non-linear rate-dependent constitutive equations require a robust algorithm to avoid numerical difficulties.

2) Combining a local method to estimate stresses and inelastic strains implicitly at each material point with a global method to solve the finite element equations once each time step is a robust and efficient way to solve problems with highly nonlinear elastic-viscoplastic constitutive equations. Stable convergence can be achieved with large time step sizes.

3) A benchmark test problem for thermal-mechanical analysis of solidification with a known analytical solution has been developed, using a highly non-linear constitutive equation to create a severe numerical challenge. This test problem is ideal to compare finite element models for solving mechanical problems with solidification.

4) Decreasing time step size greatly increases accuracy. Accuracy within 3% is possible on a mesh with 17 elements across the solid shell.

5) Refining mesh size also improves accuracy, but only if the time step size is sufficiently small. An optimum mesh size likely exists for each time step size. Accuracy within 0.1% is possible with 1000 time steps and 170 elements across the solid shell.

6) The commercial FEM package (ABAQUS) has difficulty simulating realistic constitutive behavior during solidification. To solve a simple elastic test problem with

solidification, it requires an order of magnitude more computer time than the model presented here.

7) Quadratic-displacement elements perform better than linear-displacement elements.

As part of a larger project to develop and apply a comprehensive system of mathematical models of the continuous casting of steel slabs, this finite element model is being used to predict stress and deformation in the solidifying shell in continuous casting processes. The model can realistically treat many complex phenomena, including phase transformations, temperature-dependent properties, the effects of fluid flow, and intermittent contact with the mold. The results are being used to understand the mechanisms of formation of a variety of shape and crack problems which arise in the process. Owing to its general and robust nature, this model is also suited to study thermal-mechanical behavior in other materials processes such as foundry casting, welding and heat treatment.

2.6 References

1. Weiner, J.H. and B.A. Boley, Elasto-plastic thermal stresses in a solidifying body, *Journal of Mechanics of Physics and Solids* 11 (1963) 145-154.
2. Tien, R. and V. Kaump, Thermal stresses during solidification on basis of elastic model, *ASME Journal of Applied Mechanics* 36 (1969) 763-767.
3. Voller, V.R., C.R. Swaminathan, and B.G. Thomas, Fixed Grid Techniques for Phase Change Problems: A Review, *International Journal for Numerical Methods in Engineering* 30 (1990) 875-898.
4. Zabaras, N., Y. Ruan, and O. Richmond, Front Tracking Thermomechanical Model for Hypoelastic-Viscoplastic Behavior in a Solidifying body, *Computer Methods in Applied Mechanics and Engineering* 81 (1990) 333-364.
5. Lynch, D.R., and O'Neill, K., Continuously Deforming Finite Elements for the Solution of Parabolic Problems With and Without Phase Change., *International Journal for Numerical Methods in Engineering* 17 (1981) 81-96.
6. Ghosh, S., Heat Transfer Analysis of Solidification Processes by the Arbitrary Lagrangian-Eulerian Finite Element Method, in: J.S. Gunasekera and J.C. Malas, eds., *Computational Methods in Materials Processing*, (ASME, New York, 1992) 159-170.

7. Kelly, J.E., *et al.*, Initial Development of Thermal and Stress Fields in Continuously Cast Steel Billets, *Metallurgical Transactions A* 19 (1988) 2589-2602.
8. Huang, X., B.G. Thomas, and F.M. Najjar, The Removal of Superheat from Continuous Casting Molds, *Metallurgical Transactions B* 23 (1992) 339-356.
9. Moitra, A., B.G. Thomas, and W.R. Storkman, Thermo-Mechanical Model of Steel Shell Behavior in the Continuous Casting Mold, in: EPD Congress 1992, eds, (TMS Annual Meeting, San Diego, CA, March 1-5, 1992, TMS/AIME, Warrendale, PA.) .
10. Nishida, Y., W. Droste, and S. Engler, The Air-Gap Formation Process at the Casting-Mold Interface and the Heat transfer Mechanism through the Gap, *Metallurgical Transactions A* 17 (1986) 833-844.
11. Peterson, G.P. and L.S. Fletcher, Measurement of the thermal contact conductance and thermal conductivity of anodized aluminum coatings, *Journal of Heat Transfer* 112 (1990).
12. Song, R., G. Dhatt, and A.B. Cheikh, Thermo-mechanical finite element model of casting systems, *International Journal for Numerical Methods in Engineering* 30 (1990) 579-599.
13. Boehmer, J.R., F.N. Fett, and G. Funk, Analysis of High-temperature Behaviour of Solidified Material Within A Continuous Casting Machine, *Computers & Structures* 47 (1993) 683-698.
14. Fiaer, H.G. and A. Mo, ALSPEN - A mathematical model for thermal stresses in DC-cast Al billets, *Metallurgical Transactions B* 21 (1990) 1049-1061.
15. Armero, F. and J.C. Simo, A New Unconditionally Stable Fractional Step Method for Non-Linear Coupled Thermomechanical Problems, *International Journal for Numerical Methods in Engineering* 35 (1992) 737-767.
16. Doltsinis, I.S. and S. Nolting, Studies on parallel processing for coupled problems, *Computer Methods in Applied Mechanics and Engineering* 89 (1991) 497-521.
17. Simo, J.C. and T.A. Laursen, An Augmented Lagrangian Treatment of Contact Problems Involving Friction, *Computers & Structures* 42 (1992) 97-116.
18. Liu, J.C., *et al.*, Coupled Thermomechanical Model for Continuous Bar Casting, in: *Modelling of Casting, Welding, and Advanced Solidification Processes - V*, M. Rappaz, M.R. Ozgu, and K.W. Mahin, eds, (Davos, SW, 1990, TMS, Warrendale, PA) 229-236.
19. Hannart, B., F. Cialti, and R. Schalkwuk, Thermal Stresses in DC Casting of Aluminum Slabs: Application of a Finite Element Model, in: *Light Metals*, eds, 1994, 879-887.
20. Cross, M., Control volume model of fluid flow, solidification and stress, (Thames Polytechnic, London, 1992).
21. Hattel, J., P.N. Hansen, and L.F. Hansen, Analysis of Thermal Induced Stresses in Die Casting Using A Novel Control Volume FDM-Technique, in: *Modeling of Casting, Welding and Advanced Solidification Process VI*, T.S. Pivonka, V. Voller, and L. Katgerman, eds, (Palm Coast, FL, March 21-26, 1993, TMS-AIME) 585-592.

22. Heinlein, M., S. Mukherjee, and O. Richmond, A Boundary Element Method Analysis of Temperature Fields and Stresses During Solidification, *Acta Mech.* 59 (1986) 59-81.
23. Kristiansson, J.O., Thermo Mechanical Behavior of the Solidifying Shell within Continuous Casting Billet Moulds - A Numerical Approach, *Journal of Thermal Stresses* 7 (1984) 209-226.
24. Tszeng, T.C. and S. Kobayashi, Stress Analysis in Solidification Processes: Application to Continuous Casting, *Int. J. Mach. Tools Manufact.* 29 (1989) 121-140.
25. Inoue, T. and Z.G. Wang, Thermal and Mechanical Fields in Continuous Casting Slab - A Steady State Analysis Incorporating Solidification, *Ingenieur-Archiv* 58 (1988) 265-275.
26. Williams, J.R., R.W. Lewis, and K. Morgan, An Elasto-Viscoplastic Thermal Stress Model with Applications to Continuous Casting of Metals, *International Journal for Numerical Methods in Engineering* 14 (1979) 1-9.
27. Thomas, B.G., I.V. Samarasekera, and J.K. Brimacombe, Mathematical Model of the Thermal Processing of Steel Ingots, Part II: Stress Model, *Metallurgical Transactions B* 18 (1987) 131-147.
28. Smelser, R.E. and O. Richmond, Constitutive Model Effects on Stresses and Deformations in a Solidifying Circular Cylinder, in: *Modeling and Control of Casting and Welding Processes - IV*, A.F. Giamei and G.J. Abbaschian, eds, (Palm Coast, FL, 1988, The Metallurgical Society, Warrendale, PA) 313-328.
29. Manesh, A.A.I., Thermo-elastic Stress Analysis to Predict Design Parameters of Continuous Casting, *Journal of Material Sciences* 27 (1992) 4097-4106.
30. Dalin, J.B. and J.L. Chenot, Finite element computation of bulging in continuously cast steel with a viscoplastic model, *International Journal for Numerical Methods in Engineering* 25 (1988) 147-163.
31. Inoue, T. and D.Y. Yu, Simulation of solidification and viscoplastic stresses during vertical semicontinuous direct chill casting of aluminum alloy, *International Journal of Plasticity* 8 (1992) 161-183.
32. Mo, A. and E. Holm, On the Use of Constitutive Internal Variable Equations for Thermal Stress Predictions in Aluminium Casting, (Senter for Industriforskning, Norway, 1991).
33. Bammann, D.J. and A.R. Ortega, The Influence of the Bauschinger Effect and Yield Definition on the Modeling of Welding Processes, in: *Modeling of Casting, Welding and Advanced Solidification Process VI*, T.S. Pivonka, V. Voller, and L. Katgerman, eds, (Palm Coast, FL, March 21-26, 1993, TMS-AIME) 543-551.
34. Miller, A.K., An Inelastic Constitutive Model for Monotonic, Cyclic, and Creep Deformation: Part I and II, *ASME Journal of Engineering Materials and Technology* 98 (1976) 97-103.
35. Miller, A.K., *Unified Constitutive Equations for Creep and Plasticity*, (Elsevier Applied Science Publishers Ltd, Essex, United Kingdom, 1987).

36. Anand, L., Constitutive Equations for Hot-Working of Metals, *International Journal of Plasticity* 1 (1985) 213.
37. Krieg, R.D., Numerical Integration of Some New Unified Plasticity-Creep Formulations, in: *Proceeding of 4th International Conference on Structural Mechanics in Reactor Technology*, eds, 1977, M6/4.
38. Shih, C.F., H.G. Delorenzi, and M.A. K., A Stable Computational Scheme for Stiff Time-Dependent Constitutive Equations, in: *Proceedings of the 4th International Conference on Structural Mechanics in Reactor Technology*, eds, 1977, L2/2.
39. Zienkiewicz, O.C. and I.C. Corneau, Viscoplasticity -Plasticity and Creep in Elastic Solids - A Unified Numerical Solution Approach, *International Journal for Numerical Methods in Engineering* 8 (1974) 821-845.
40. Corneau, I., Numerical Stability in Quasi-Static Elasto/Visco-plasticity, *International Journal for Numerical Methods in Engineering* 9 (1975) 109-127.
41. Hughes, T.J.R. and R.L. Taylor, Unconditionally Stable Algorithm for Quasi-Static Elasto/Visco-Plastic Finite Element Analysis, *Computers and Structures* 8 (1978) 169-181.
42. Snyder, M.D. and K.J. Bathe, A Solution Procedure for Thermo-Elastic-Plastic and Creep Problems, *Nuclear Engineering and Design* 64 (1981) 49-80.
43. Hinter, E. and D.J.R. Owen, *Finite Elements in Plasticity: Theory and Practice*, (Pineridge Press, Swansea, Wales, 1980).
44. Peirce, D., C.F. Shih, and A. Needleman, A Tangent Modulus Method for Rate Dependent Solids, *Computers and Structures* 18 (1984) 875-887.
45. Tanaka, T.G. and A.K. Miller, Development of a Method for Integrating Time Dependent Constitutive Equations with Large or Negative Strain Rate Sensitivity, *International Journal for Numerical Methods in Engineering* 26 (1988) 2457-2485.
46. Wenner, M., A Generalized Forward Gradient Procedure for Rate Sensitive Constitutive Equations, *International Journal for Numerical Methods in Engineering* 36 (1993) 985-995.
47. Lush, A.M., S.B. Brown, and L. Anand, An Implicit Time-Integration Procedure for a Set of Internal Variable Constitutive Equations for Isotropic Elasto-Viscoplasticity, *International Journal of Plasticity* 5 (1989) 521-549.
48. Zabaras, N. and A.B.F.M. Arif, A Family of Integration Algorithms for Constitutive Equations in Finite Deformations Elasto-viscoplasticity, *International Journal for Numerical Methods in Engineering* 33 (1992) 59-84.
49. Chulya, A. and K.P. Walker, A New Uniformly Valid Asymptotic Integration Algorithm for Elasto-Plastic Creep and Unified Viscoplastic Theories Including Continuum Damage, *International Journal for Numerical Methods in Engineering* 32 (1991) 385-418.
50. Chang, T.Y.P., A.F. Saleeb, and I. Iskovitz, Finite Element Implementation of State Variable-based Viscoplasticity Models, *Computers and Structures* 46 (1993) 33-45.

51. Nemat-Nasser, S. and Y.F. Li, A New Explicit Algorithm for Finite-deformation Elastoplasticity And Elastoviscoplasticity: Performance Evaluation, *Computers & Structures* 44 (1992) 937-963.
52. Nemat-Nasser, S. and D.T. Chung, An explicit constitutive algorithm for large-strain, large-strain-rate elastic-viscoplasticity, *Computer Methods in Applied Mechanics and Engineering* 95 (1992) 205-219.
53. Stolle, D., An Interpretation of Initial Stress and Strain Methods, and Numerical Stability, *International Journal for Numerical and Analytical Methods in Geomechanics* 15 (1991) 399-416.
54. Simo, J.C. and R.L. Taylor, Consistent Tangent Operators for Rate-Independent Elastoplasticity, *Computer Methods in Applied Mechanics and Engineering* 48 (1985) 101-118.
55. Tien, O. and O. Richmond, Theory of Maximum Tensile Stresses in Solidifying Shell of a Constrained Rectangular Casting, *ASME Journal of Applied Mechanics* 49 (1982) 481-486.
56. Lewis, R.W., K. Morgan, and P.M. Roberts, Determination of Thermal Stresses in Solidification Problems, in: J.F.T. Pittman Zienkiewicz, O. C., Wood, R. D., Alexander, J. M., eds., *Numerical Analysis of Forming Processes*, (John Wiley & Sons, Swansea, 1984) 405-431.
57. Okamura, K. and K. Yamamoto, Coupled Analysis Between Thermal Deformation and Heat Transfer of Solidifying Shell in Continuous Casting Mold, in: *Modeling of Casting, Welding and Advanced Solidification Processes VI*, T.S. Piwonka, V. Voller, and L. Katgerman, eds, (Palm Beach, FL, 1993, TMS-AIME, Warrendale, PA) 535-541.
58. Moitra, A., H. Zhu, and B.G. Thomas, Thermo-mechanical model of steel shell behavior in the continuous casting mold, submitted to *Metallurgical Transactions B* (1995)
59. Yamanaka, A., *et al.*, Measurement of Critical Strain for Solidification Cracking, in: *Modelling of Casting, Welding, and Advanced Solidification Processes - V*, M. Rappaz, M.R. Ozgu, and K.W. Mahin, eds, (Davos, SW, 1990, TMS, Warrendale, PA) 279-284.
60. Denis, S., S. Sjostrom, and A. Simon, Coupled temperature, stress, phase transformation calculation model numerical illustration of the internal stresses evolution during cooling of a eutectoid carbon steel cylinder, *Metallurgical Transactions A* 18 (1987) 1203-1212.
61. Harste, K., Investigation of the shrinkage and the origin of mechanical tension during the solidification and successive cooling of cylindrical bars of Fe-C alloys., Dissertation (German), Technical University of Clausthal, 1989.
62. Bergheau, J.M. and J.B. Leblond, Coupling between heat flow, metallurgy and stress-strain computations in steels: the approach developed in the computer code Sysweld for welding or quenching, in: *Modelling of Casting, Welding, and Advanced Solidification Processes - V*, M. Rappaz, M.R. Ozgu, and K.W. Mahin, eds, (Davos, SW, 1990, TMS, Warrendale, PA) 203-210.

63. Leblond, J.B., G. Mottet, and J.C. Devaux, A Theoretical and Numerical Approach to the Plastic Behaviour of Steels During Phase Transformations-II. Study of Classical Plasticity for Ideal-plastic Phases, *Journal of Mechanics of Physics and Solids* 34 (1986) 411-432.
64. Leblond, J.B., G. Mottet, and J.C. Devaux, A Theoretical and Numerical Approach to the Plastic Behaviour of Steels During Phase Transformations-I. Derivation of General Relations, *Journal of Mechanics of Physics and Solids* 34 (1986) 395-409.
65. Rappaz, M., Modelling of microstructure formation in solidification processes, *International Material Review* 34 (1989) 93-123.
66. Das, S., *et al.*, Finite Element Modeling of a Single-pass GMA Weldment, in: *Modeling of Casting, Welding and Advanced Solidification Process VI*, T.S. Pivonka, V. Voller, and L. Katgerman, eds, (Palm Coast, FL, March 21-26, 1993, TMS-AIME) 593-601.
67. Kikuchi, N. and J.T. Oden, *Contact Problems in Elasticity: A Study of Variation Inequalities and Finite Element Methods*, (SIAM, Philadelphia, 1988).
68. Zhong, Z. and J. Mackerle, Static Contact Problems - A Review, *Engineering Computations* 9 (1992) 3-37.
69. Hughes, T.J.R., *et al.*, A Finite Element Method for a Class of Contact-Impact Problems, *Computer Methods in Applied Mechanics and Engineering* 8 (1976) 249-276.
70. Hallquist, J.O., G.L. Goudreau, and D.J. Benson, Sliding Interfaces with Contact-Impact in Large-Scale Lagrangian Computations, *Computer Methods in Applied Mechanics and Engineering* 51 (1985) 107-137.
71. Bathe, K.J. and A. Chaudhary, A Solution Method for Planar and Axisymmetric Contact Problems, *International Journal for Numerical Methods in Engineering* 21 (1985) 65-88.
72. Belytschko, T. and O.M. Neal, Contact-Impact by the Pinball Algorithm with Penalty, Projection and Lagrangian Methods, in: *Computational Techniques for Contact, Impact, Penetration and Performance of Solids*, L.E. Schwer, eds, (San Francisco, 1989, The Winter Annual Meeting of ASME).
73. Alart, P. and A. Curnier, A mixed formulation for frictional contact problems prone to Newton like solution methods, *Computer Methods in Applied Mechanics and Engineering* 92 (1991) 353-375.
74. Wriggers, P., J.C. Simo, and R.L. Taylor, Penalty and augmented Lagrangian formulations for contact problems, in: *NUMETA Conference*, eds, (Swansea, 1985).
75. Ohnaka, I. and Y. Yashima, Stress Analysis of Steel Shell Solidifying in Continuous Casting Mold, in: *Modelling of Casting and Welding Processes IV*, A.F. Giamei and G.J. Abbaschian, eds, (Palm Coast, FL, 1988, TMS, Warrendale, PA).
76. Bellet, M., M. Menai, and F. Bay, Finite Element Modeling of the Cooling Phase in Casting Processes, in: *Modeling of Casting, Welding and Advanced Solidification Process VI*, T.S. Pivonka, V. Voller, and L. Katgerman, eds, (Palm Coast, FL, March 21-26, 1993, TMS-AIME) 561-568.

77. Zavarise, G., *et al.*, A Numerical Model for Thermomechanical Contact Based on Microscopic Interface Laws, *International Journal for Numerical Methods in Engineering* 35 (1992) 767-785.
78. Wriggers, P. and G. Zavarise, Thermomechanical Contact - A Rigorous But Simple Numerical Approach, *Computers & Structure* 46 (1993) 47-53.
79. Zienkiewicz, O.C., Flow Formulation for Numerical Solution of Forming Processes, in: J.F.T. Pittman, *et al.*, eds., *Numerical Analysis of Forming Processes*, (John Wiley & Sons, 1984).
80. Okamura, K. and H. Kawashima, Three-dimensional Elasto-Plastic and Creep Analysis of Bulging in Continuously Cast Slabs, *ISIJ International* 29 (1989) 666-672.
81. Barber, B. and A. Perkins, Strand Deformation in Continuous Casting, *Ironmaking and Steelmaking* 16 (1989) 406-411.
82. Grill, A., J.K. Brimacombe, and F. Weinberg, Mathematical analysis of stresses in continuous casting of steel, *Ironmaking and Steelmaking* 3 (1976) 38-47.
83. Ghosh, S. and N. Kikuchi, An Arbitrary Lagrangian-Eulerian Finite Element Method for Large Deformation Analysis of Elastic-Viscoplastic solids, *Computer Methods in Applied Mechanics and Engineering* 86 (1991) 127-188.
84. Ghosh, S., Arbitrary Lagrangian-Eulerian Finite Element Analysis of Large Deformation in Contacting Bodies, *International Journal for Numerical Methods in Engineering* 33 (1992) 1891-1925.
85. Liu, W.K., T. Belytschko, and H. Chang, An Arbitrary Lagrangian-Eulerian Finite Element Method for Path-dependent Materials, *Computer Methods in Applied Mechanics and Engineering* 58 (1986) 227-245.
86. Liu, W.K., *et al.*, Arbitrary Lagrangian-Eulerian Petrov-Galerkin Finite Elements for Nonlinear Continua, *Computer Methods in Applied Mechanics and Engineering* 68 (1988) 259-310.
87. Haber, R.B., A Mixed Eulerian-Lagrangian Displacement Model for Large-Deformation Analysis in Solid Mechanics, *Computer Methods in Applied Mechanics and Engineering* 43 (1984) 277-292.
88. Benson, D.J., An Efficient, Accuracy, Simple Method for Nonlinear Finite Element Programs, *Computer Methods in Applied Mechanics and Engineering* 72 (1989) 305-360.
89. Harste, K., A. Jablonka, and K. Schwerdtfeger, Shrinkage and Formation of Mechanical Stresses during Solidification of Round Steel Strands, in: 4th Int. Conf. on Continuous Casting, eds, (Centres de Recherches Metallurgiques and Verein Deutscher Eisenhüttenleute, 1988, Stahl und Eisen, Brussels) 633-644.
90. Karlsson, L., *et al.*, Residual Stresses and Deformations in a Welded Thin-Walled Pipe", in: eds., *Weld Residual Stress and Plastic Deformation*, Book No. H0488, (ASME, PVP, 1989) 7-11.
91. Lindgren, L.E. and L. Karlsson, Deformations and stresses in welding of shell structures, *International Journal for Numerical Methods in Engineering* 25 (1988) 635-655.

92. Wimer, F.G., *et al.*, Theoretical Analysis of Strand Shell Behavior in the Mold, in: CCC'90, eds, (Linz/Austria,1990).
93. Kristiansson, J.O., Thermal Stresses in Early Stages of Solidification of Steel, *Journal of Thermal Stresses* 5 (1982) 315-330.
94. Wikander, L., L. Karlsson, and M. Nasstrom, Thermomechanical FE plane models of welding, in: *Modeling of Casting, Welding and Advanced Solidification Process VI*, T.S. Piwonka, V. Voller, and L. Katgerman, eds, (Palm Coast, FL, March 21-26,1993, TMS-AIME) 553-568.
95. ABAQUS, User's Manual, (Hibbitt, Karlsson & Sorensen, Inc.,Providence, RI,1990).
96. Marcellin, J., M. Abouaf, and J. Chenot, Analysis of residual stresses in hot-rolled complex beams, *Computer Methods in Applied Mechanics and Engineering* 56 (1986) 1-6.
97. Donea, J. and S. Giuliani, Creep Analysis of Transversely Isotropic Bodies Subjected to Time-Dependent Loading, *Nuclear Engineering and Design* 24 (1973) 410-419.
98. Bourdouxhe, M., R. Charlier, and S. Cescotto, A finite element for thermo-mechanical problems, in: *2nd Int. Conf. on Numerical Methods in Industrial Forming Processes*, K. Mattiasson, *et al.*, eds, (Gothenburg, Sweden,1986, A.A. Balkema, Rotterdam, Netherlands) 97-102.
99. Zienkiewicz, O.C., *The Finite Element Method*, (McGraw-Hall,New-York,Toronto,London,1977).
100. Reddy, M.P. and J.N. Reddy, Numerical simulation of forming processes using a coupled fluid flow and heat transfer model, *International Journal for Numerical Methods in Engineering* 35 (1992) 807-833.
101. Jablonka, A., K. Harste, and K. Schwerdtferger, Thermomechanical properties of iron and iron-carbon alloys: density and thermal contraction, *Steel Research* 62 (1991) 24-32.
102. Mendelson, A., *Plasticity - Theory and Applications*, (R.E. Krieger Publishing,Malabar, FL,1983).
103. Brown, S., K. Kim, and L. Anand, An Internal Variable Constitutive Model for Hot Working of Metals, *International Journal of Plasticity* 5 (1989) 95-130.
104. Anand, L., Constitutive Equations for the Rate-Dependent Deformation of Metals at Elevated Temperatures, *ASME Journal of Engineering Materials and Technology* 104 (1982) 12-17.
105. Kozlowski, P., *et al.*, Simple Constitutive Equations for Steel at High Temperature, *Metallurgical Transactions A* 23 (1992) 903-918.
106. Glowinski, R. and P.L. Talle, *Augmented Lagrangian and Operator-Splitting Methods in Non-linear Mechanics*, (SIAM,Philadelphia, PA,1989).
107. Douglas, J. and H.H. Rachford, On the Numerical Solution of the Heat Conduction problem in 2d and 3d Space Variable, *Trans. Amer.Math.Soc.* 82 (1956) 421-439.

108. Argyris, J.H., L.E. Vaz, and K.J. Willam, Improved Solution Methods for Inelastic Rate Problems, *Computer Methods in Applied Mechanics and Engineering* 16 (1978) 231-277.
109. Owen, D.R.J. and E. Hinton, *Finite Element in Plasticity: Theory and Practice*, (Pineridge Press Ltd., Swansea, UK, 1980).
110. Forsythe, G. and C. Moler, *Computer Solution of Linear Algebraic Systems*, (Prentice Hall, Englewood Cliffs, NJ, 1967).
111. Storkman, W.R. and B.G. Thomas, Heat Flow and Stress Models of Continuous Casting to Predict Slab Shape, in: *Modeling of Casting and Welding Processes*, eds, (Palm Coast, FL, 1988, TMS/AIME, April, 14-17).
112. Chen, Y. and I.C. Sheng, On the solid-fluid transition zone in welding analysis, *ASME Journal of Engineering Materials and Technology* 115 (1993) 17-23.
113. ABAQUS, The use of UMAT to model a phase change in an elastic material, 1992)
114. UBC, VBAND: UBC Matrix subroutines to solve systems of linear equations, (University of British Columbia Computing Center report, 1984)
115. Cook, R.D., *Concepts and Applications of Finite Element Analysis*, Second, (John Wiley and Sons, New York, 1984).
116. Sladek, J., V. Sladek, and I. Markechova, Boundary Element Methods Analysis of Stationary Thermoelasticity Problems in Non-homogenous Media, *International Journal for Numerical Methods in Engineering* 30 (1990) 505-516.
117. Carslaw, H.S. and J.C. Jaeger, *Conduction of Heat in Solids*, (Clarendon, Oxford, 1959).
118. Taylor, L.M. and E.B. Becker, Some Computational Aspects of Large Deformation Rate-Dependent Plasticity Problems, *Computer Methods in Applied Mechanics and Engineering* 41 (1983) 251-277.
119. Choi, J., Three-Dimensional Transient Finite Element Model for Residual Stress and Solidification in the GMAW Process for AISI 304 Stainless Steel, Ph.D. Dissertation, University of Illinois at Urbana-Champaign, 1995.
120. Thomas, B.G., I.V. Samarasekara, and J.K. Brimacombe, Comparison of Numerical Modeling Techniques for Complex, Two-Dimensional, Transient Heat-Conduction Problems, *Metallurgical Transactions B* 15 (1984) 307-318.
121. Wray, P.J., Effect of Carbon Content on the Plastic Flow of Plain Carbon Steels at Elevated Temperatures, *Metallurgical Transactions A* 13 (1982) 125-134.
122. Suzuki, H.G., S. Nishimura, and S. Yamaguchi, Physical Simulation of the Continuous Casting of Steels, in: *Physical Simulation of Welding, Hot Forming, and Continuous Casting*, eds, (May 2-4, 1988, CANMET, Canada).

Chapter 3

Comparison of Numerical Time-Integration Schemes and Finite-Element Implementations for Unified Temperature-Dependent Elastic-Viscoplastic Constitutive Models

Several robust and efficient numerical techniques have been implemented into finite element calculations of unified, isotropic, temperature-dependent elastic-viscoplastic models. Three numerical time-integration schemes are employed to integrate the constitutive behavior, including the explicit forward Euler scheme, the implicit backward Euler scheme and the alternating implicit-explicit scheme based on the operator-splitting technique. The latter two implicit-related methods involve transforming the tensor algorithm constitutive models for isotropic materials into two scalar equations to solve at each spatial integration point. This is similar to the uni-axial problem with prescribed strain rate. Several constitutive algorithms are examined to solve for the two unknowns of stress magnitude and inelastic strain magnitude. These "local" algorithms include the successive substitution method, the forward gradient method, the Newton-Raphson method, the bounded Newton method and the Nemat-Nasser's explicit prediction method. The performance of each combination of methods were compared using a computational-demanding solidification test problem with known solution. Results indicate that a formulation comprised of the alternating implicit-explicit time integration scheme and the bounded Newton method at the local level calculation is the most robust, accurate and efficient method. Thus it has been selected to analyze complex thermal-mechanical behavior in continuous casting.

3.1 Introduction

Many complex phenomena are involved in materials processing and manufacturing processes. These include internal structure evolution, severe thermal-mechanical loading, complex states and histories of temperature, stress and deformation.

The finite element method is usually employed for spatial integration during nonlinear analysis of these processes. The importance of understanding these phenomena to optimize the process has motivated the development of more accurate and realistic constitutive models to characterize mechanical behavior. To properly represent typical deformation phenomena such as strain hardening and rate-dependent creep-plasticity interactions over a wide range of temperatures encountered in elevated-temperature processes such as casting and welding, it is accepted that unified elastic-viscoplastic models are better than classic creep and plasticity theory [1-4]. However, there is a considerable challenge to utilize these models because the constitutive differential equations for rate-dependent unified elastic-viscoplastic models are both highly nonlinear and mathematically "stiff" [2, 5, 6]. This means that a small change of one state variable may result in a large change of other state variables. To overcome the stability problem inherent in numerical integration of these stiff differential equations, a very small time step size or a very sophisticated numerical algorithm with several iterations per time step is needed. As a consequence, prohibitively high computational time can make modeling a real process very expensive or even computationally impossible. Developing robust, accurate and efficient algorithms for large-scale finite element analysis of unified elastic-viscoplastic models is still a central problem of current research for modeling mechanical behavior in materials processing and manufacturing, although extensive progress has been made on this topic during the last two decades.

In general, transient finite element analysis involving rate-dependent nonlinear material behavior is performed in a discrete sequence of time increments using a time-marching method starting from given initial conditions. With a time-integration procedure, the rate-dependent constitutive model is transformed into a rate-independent algebraic formula in terms of the state variables stress, strain, inelastic strain and internal structure at the end of the time increment. This algebraic formula is also called an algorithmic constitutive model, to distinguish it from the rate form of the constitutive

model. Thus, besides the data that are known at the beginning of the time increment, the stress with respect to the strain increment also depends on the time-integration scheme and the related forms of inelastic strain rate. Numerical calculations on both the global level and the local level are usually involved in the large-scale computation with the material nonlinearity described by this kind of algorithmic constitutive model [7-10]. On the global level, incremental strain at the end of a time step is calculated using various Newton-Raphson schemes based on the finite element form of global equilibrium equations. These schemes use the data from the beginning of the increment as well as data from the local level calculation. On the local level, stress and inelastic strain are calculated at each "material point" at the end of the time increment by a constitutive algorithm to satisfy the algorithmic constitutive model in which the incremental strain is estimated by the global level calculation. These material points are the spatial numerical integration points of the finite element form of the equilibrium equations. To get a converged stress and strain field at the end of each time increment which satisfies both the algorithmic constitutive model and the finite element form of the equilibrium equations, either the nested iteration scheme or the simultaneous iteration scheme can be used to link the global and local level calculations. Due to the complexity of the finite-element implementation of a rate-dependent constitutive model, several numerical issues arise.

Although a large number of investigations have been made for nonlinear finite element analysis with unified constitutive models, a generally applicable method which is robust and efficient as well as easy for the finite element implementation has not been demonstrated. It is difficult to say which method is best because a method which performs well for some problems may not work for another. The constitutive model itself also plays a significant role for the choice of stress integration schemes. Hornberger and Stamm [11] showed that the explicit Euler scheme is more efficient than the backward Euler scheme for their finite element analysis with Robinson's model while Corts and Kollmann [12] pointed out that direct integration of Hart's model using an explicit

algorithm was not possible. Detailed studies of various stress integration schemes and constitutive algorithms for the specified constitutive models are necessary to characterize the related model and schemes before performing a large-scale finite element analysis. Furthermore, most of the schemes and algorithms developed are limited to their applications on the isothermal, hypoelastic unified constitutive models.

The first objective of this study is to develop finite element implementations of methods proposed in the literature for numerical integration of general isotropic temperature-dependent unified hyperelastic-viscoplastic models such as the model developed by Kozłowski et al [4] for the continuous casting process. Another objective is to compare the relative efficiency and robustness of these numerical implementations. Specifically, three numerical time-integration schemes are compared. These include the explicit forward Euler scheme, the implicit backward Euler scheme and the alternating implicit-explicit scheme based on the operator-splitting technique. The latter two method involves transforming the tensor algorithm constitutive model of an isotropic material into two simultaneous nonlinear equations in terms of two scalar unknowns of the stress magnitude and the inelastic strain magnitude. This is very similar to the uni-axial problem with prescribed strain rate. In addition, various constitutive algorithms are compared for solving this two-unknown equations at each material point. These include the successive substitution, the forward gradient method, the Newton-Raphson method, the two-level bounded Newton method and the Nemat-Nasser's method. Evaluation and comparison of the accuracy and efficiency of the proposed combined schemes are made through several numerical experiments including uni-axial calculations and finite element analysis of a numerically challenging problem of stress during solidification with a known solution.

3.2 Unified constitutive equations

Attention in this study is focused on "unified" temperature-dependent elastic-visco-plastic models for mechanical behavior of isotropic metals. The particular

phenomenological approach used here evaluates the effective inelastic strain rate as a function of the effective stress, the effective inelastic strain and temperature. Furthermore, the analysis is limited to classic small deformation theory, which implies that strains, displacements and rotations all have negligible effect on geometry. Each term in the following equations represents a field variable, which varies continuously over the spatial domain in 1, 2 or 3 dimensions. For simplicity of notation, no special notation is used to denote this. In this section, bold variables are tensors containing more than one such field variable component. The total strain rate tensor $\dot{\boldsymbol{\epsilon}}$ at a material point can be expressed by an additive decomposition into an elastic strain rate tensor $\dot{\boldsymbol{\epsilon}}^e$, an inelastic strain rate tensor $\dot{\boldsymbol{\epsilon}}^p$ and a thermal strain rate tensor $\dot{\boldsymbol{\epsilon}}^T$,

$$\dot{\boldsymbol{\epsilon}} = \dot{\boldsymbol{\epsilon}}^e + \dot{\boldsymbol{\epsilon}}^p + \dot{\boldsymbol{\epsilon}}^T . \quad (3.1)$$

From the generalized form of Hooke's law, the stress tensor $\boldsymbol{\sigma}$ can be written in the form

$$\boldsymbol{\sigma} = \mathbf{C} : \boldsymbol{\epsilon}^e , \quad (3.2)$$

or
$$\sigma_{ij} = \sum_{k=1}^3 \sum_{l=1}^3 C_{ijkl} \epsilon_{kl}^e$$

in which \mathbf{C} is a fourth-order isotropic elastic tensor with components :

$$C_{ijkl}(T) = \lambda(T) \delta_{ij} \delta_{kl} + \mu(T) (\delta_{ik} \delta_{jl} + \delta_{il} \delta_{jk}) , \quad (3.3)$$

where $\lambda(T)$ and $\mu(T)$ are temperature-dependent Lamé constants and $\boldsymbol{\delta}$ is the Kronecker delta ($\delta_{ij} = 1$, if $i=j$; otherwise $\delta_{ij} = 0$). The corresponding rate form of the constitutive relation can be written as

$$\dot{\boldsymbol{\sigma}} = \mathbf{C} : (\dot{\boldsymbol{\epsilon}} - \dot{\boldsymbol{\epsilon}}^T - \dot{\boldsymbol{\epsilon}}^p) + \dot{T} \frac{\partial \mathbf{C}}{\partial T} : (\boldsymbol{\epsilon} - \boldsymbol{\epsilon}^T - \boldsymbol{\epsilon}^p) . \quad (3.4)$$

The second term in the above equation, which is neglected in a hypoelastic form, is the contribution to the stress rate from temperature-dependent variation of the elastic tensor. Equation (3.4) reduces to classical hyperelasticity in the absence of inelastic deformation. For thermally isotropic materials, the thermal strain tensor $\boldsymbol{\epsilon}^T$ is written as

$$\boldsymbol{\epsilon}^T = (\text{TLE}(T) - \text{TLE}(T_0)) \boldsymbol{\delta}, \quad (3.5)$$

in which the state function TLE is the thermal linear expansion (m/m) caused by both temperature differences and phase changes. Thermal strain rate $\dot{\boldsymbol{\epsilon}}^T$ can be found by direct or numerical differentiation of Eqs. (3.5), knowing the temperature field history.

For associated plasticity flow, components of the inelastic strain rate $\dot{\boldsymbol{\epsilon}}^P$ are given by the Prandtl-Reuss relations

$$\dot{\boldsymbol{\epsilon}}^P = \sqrt{\frac{3}{2}} \frac{\dot{\bar{\epsilon}}^P}{\bar{\sigma}} \mathbf{N}, \quad (3.6)$$

where \mathbf{N} is the unit direction tensor of the inelastic strain rate, defined as:

$$\mathbf{N} = \sqrt{\frac{3}{2}} \frac{\boldsymbol{\sigma}'}{\bar{\sigma}}. \quad (3.7)$$

Here the deviatoric stress tensor $\boldsymbol{\sigma}'$ and the effective stress $\bar{\sigma}$ are defined by

$$\boldsymbol{\sigma}' = \boldsymbol{\sigma} - \frac{1}{3} \text{tr}(\boldsymbol{\sigma}) \boldsymbol{\delta}, \quad (3.8)$$

$$\bar{\sigma} = \sqrt{\frac{3}{2} \boldsymbol{\sigma}' \cdot \boldsymbol{\sigma}'}, \quad (3.9)$$

respectively ($\text{tr}(\boldsymbol{\sigma}) = \sum_{i=1}^3 \sigma_{ii}$, $\boldsymbol{\sigma} \cdot \boldsymbol{\sigma} = \sum_{i=1}^3 \sum_{j=1}^3 \sigma_{ij} \sigma_{ji}$). The effective inelastic strain rate $\dot{\bar{\epsilon}}^P$,

which represents all inelastic effects including creep and plasticity, is a scalar function of the current effective stress, the effective inelastic strain $\bar{\epsilon}^P$ and temperature T

$$\dot{\bar{\epsilon}}^P = f(\bar{\sigma}, \bar{\epsilon}^P, T). \quad (3.10)$$

3.3 Time-integration procedure

Adopting an incremental approach, state variables $(\boldsymbol{\sigma}, \boldsymbol{\varepsilon}, \boldsymbol{\varepsilon}^p, \mathbf{u})$ at time $t+\Delta t$ are related with known values of these quantities at time t through a time-integration of the given constitutive model. During each step $[t, t+\Delta t]$, thermal strain rate is assumed to be a constant and can be calculated from temperature, which is given by a separate thermal analysis.

Using Eqs (3.1), (3.2) and (3.6), the state $(\boldsymbol{\sigma}, \boldsymbol{\varepsilon}, \boldsymbol{\varepsilon}^p, \mathbf{u})$ at time $t+\Delta t$ can be expressed in terms of the states at time t as,

$$\boldsymbol{\varepsilon}_{t+\Delta t} = \boldsymbol{\varepsilon}_t + \Delta \boldsymbol{\varepsilon} , \quad (3.11)$$

$$\boldsymbol{\varepsilon}_{t+\Delta t}^p = \boldsymbol{\varepsilon}_t^p + \int_t^{t+\Delta t} \sqrt{\frac{3}{2}} \dot{\boldsymbol{\varepsilon}}^p \mathbf{N} \, dt , \quad (3.12)$$

$$\boldsymbol{\sigma}_{t+\Delta t} = \mathbf{C}_{t+\Delta t} : [\boldsymbol{\varepsilon}_t - \boldsymbol{\varepsilon}_t^T - \boldsymbol{\varepsilon}_t^p + \int_t^{t+\Delta t} (\dot{\boldsymbol{\varepsilon}} - \dot{\boldsymbol{\varepsilon}}^T - \sqrt{\frac{3}{2}} \dot{\boldsymbol{\varepsilon}}^p \mathbf{N}) dt] , \quad (3.13)$$

$$\mathbf{u}_{t+\Delta t} = \mathbf{u}_t + \Delta \mathbf{u} . \quad (3.14)$$

Theses equations, (3.11)-(3.14), together with the global level governing PDE, i.e., equilibrium equations, must be solved simultaneously using a time-stepping algorithm, which integrates over both the spatial and time domains. The standard finite-element method is used for spatial integration. The next section reviews various time-integration methods.

Some attempts [13, 14] have made to pursue nonlinear evolution of strain history within one time step. Nevertheless, most finite element routines for time-dependent nonlinear analysis assume constant strain rate on the time interval $[t, t+\Delta t]$, which implies a linear evolution of strain history. Non-linear strain histories naturally lead to relatively small time internals to control the inherent errors of this approximation. From this

assumption, $\boldsymbol{\sigma}_{t+\Delta t}$ can be determined by proper integration of the inelastic strain rate in Eqs. (3.13) which yields:

$$\boldsymbol{\sigma}_{t+\Delta t} = \mathbf{C}_{t+\Delta t} : [\boldsymbol{\epsilon}_t - \boldsymbol{\epsilon}_t^T - \boldsymbol{\epsilon}_t^p + \Delta \boldsymbol{\epsilon} - \dot{\boldsymbol{\epsilon}}^T \Delta t - \int_t^{t+\Delta t} (\sqrt{\frac{3}{2}} \dot{\boldsymbol{\epsilon}}^p \mathbf{N}) dt]. \quad (3.15)$$

Among the many numerical integration schemes which could be used to evaluate the time integrals in Eqs (3.15), three schemes encompassing the two most popular schemes and one promising but relative new scheme are employed in this study. These schemes are known as: (1) one-step forward Euler scheme; (2) one-step backward Euler scheme; and (3) two-step alternating implicit-explicit scheme from the operator-splitting technique [15]. Each of these schemes will be described in the next section and discussed from the point of view of numerical implementation as well as numerical stability and accuracy.

3.3.1 Explicit time integration / forward Euler scheme

Applying an explicit forward Euler scheme to the inelastic strain rate in Eqs. (3.15), the following a linear algorithmic constitutive model is obtained:

$$\boldsymbol{\sigma}_{t+\Delta t} = \mathbf{C}_{t+\Delta t} : [\boldsymbol{\epsilon}_t - \boldsymbol{\epsilon}_t^T - \boldsymbol{\epsilon}_t^p + \Delta \boldsymbol{\epsilon} - \dot{\boldsymbol{\epsilon}}^T \Delta t - \sqrt{\frac{3}{2}} \dot{\boldsymbol{\epsilon}}^p \mathbf{N}_t \Delta t], \quad (3.16)$$

Eqs. (3.16) is a classic implementation of the initial strain method [16-19]. The incremental strain $\Delta \boldsymbol{\epsilon}$ is found from spatial integration using the finite element method. Then $\boldsymbol{\sigma}_{t+\Delta t}$ and $\boldsymbol{\epsilon}_{t+\Delta t}^p$ are simply updated using through Eqs. (3.16) and (3.12). It is well-known that this scheme is first-order accurate and only conditionally-stable.

Compared with various multi-step integration schemes including the predictor-corrector, fourth-order Runge-Kutta and Gear's method, this simplest one-step forward Euler method has been found to perform better numerically [18, 20]. However, the conditional stability of this scheme may restrict the time step size to be far smaller than

that of the corresponding accuracy requirement [21]. Although Cormeau [21] found stability criteria for some simple viscoplasticity models, these stability criteria can not be expanded to general unified elastic-viscoplastic models. The danger of numerical instability or inaccuracy by manually controlling the time step size may lead to unreliable solution. The computational cost of this method depends on the time step size, which can be quite small.

3.3.2 Implicit time integration / backward Euler scheme

Several implicit time-integration schemes are available to treat the inelastic strain rate in Eqs. (3.15) [8, 11, 12, 16, 17, 22-28]. These schemes are designed to overcome the stability problems of the explicit method for integrating highly nonlinear rate-dependent constitutive models. Most of these schemes fall into one of two popular families of algorithms: the generalized trapezoidal rule and the generalized midpoint rule. Ortiz and Popov [12] studied the accuracy and stability of these algorithms for elasto-plastic models. These elasto-plastic models also can be transformed into rate-dependent constitutive models. The equivalent inelastic strain rate in these models is determined by the plastic consistency condition [12]. Their results show that both schemes are unconditionally stable for the relaxation factor ≥ 0.5 for a von Mises' flow and first order accurate of the local truncation error. The Euler backward scheme, a special case of both algorithms (relaxation factor is 1 for both algorithms), is unconditionally stable and has better accuracy for both large strain increment and small strain increment. The choice 0.5 of the relaxation factor leads to second-order accuracy for small strain increments. This conclusion is also consistent with the investigations for viscoplastic models in other similar studies [8, 22-26]. In fact, the backward Euler integration scheme of inelastic strain rate in the unified constitutive models is a generalization of the well known [25] "radial-return" algorithm of classic rate-independent plasticity [29, 30].

Applying the backward Euler scheme to both the inelastic strain rate in Eqs.(3.15) and the effective inelastic strain rate in Eqs.(3.10), the following nonlinear system of algebraic equations is obtained:

$$\boldsymbol{\sigma}_{t+\Delta t} = \mathbf{C}_{t+\Delta t} : [\boldsymbol{\epsilon}_t - \boldsymbol{\epsilon}_t^T - \boldsymbol{\epsilon}_t^p + \Delta \boldsymbol{\epsilon} - \dot{\boldsymbol{\epsilon}}^T \Delta t - \sqrt{\frac{3}{2}} f(\bar{\boldsymbol{\sigma}}_{t+\Delta t}, \bar{\boldsymbol{\epsilon}}_{t+\Delta t}^p, T) \mathbf{N}_{t+\Delta t} \Delta t], \quad (3.17)$$

$$\bar{\boldsymbol{\epsilon}}_{t+\Delta t}^p = \bar{\boldsymbol{\epsilon}}_t^p + f(\bar{\boldsymbol{\sigma}}_{t+\Delta t}, \bar{\boldsymbol{\epsilon}}_{t+\Delta t}^p, T) \Delta t. \quad (3.18)$$

Again, $\Delta \boldsymbol{\epsilon}$ is found from the finite element calculation or global calculation. The algorithmic constitutive model in Eqs.(3.17) and (3.18) is then solved for $\boldsymbol{\sigma}_{t+\Delta t}$ and $\bar{\boldsymbol{\epsilon}}_{t+\Delta t}^p$. Numerical implementation of this scheme is relative complex due to strong non-linearity of these equations. A nested iteration scheme is usually used to perform this type of nonlinear analysis. The outer equilibrium iterations seek the end-of-incremental displacement or the strain rate from the finite element equilibrium equations at time $t+\Delta t$ based on the estimated $\boldsymbol{\sigma}_{t+\Delta t}$ and $\bar{\boldsymbol{\epsilon}}_{t+\Delta t}^p$. The inner constitutive iterations enforce $\boldsymbol{\sigma}_{t+\Delta t}$ and $\bar{\boldsymbol{\epsilon}}_{t+\Delta t}^p$ to satisfy the algorithmic constitutive model at each material point with the estimated $\Delta \boldsymbol{\epsilon}$ from global level calculation. Final convergence to the solution of $\Delta \boldsymbol{\epsilon}$, $\boldsymbol{\sigma}_{t+\Delta t}$ and $\bar{\boldsymbol{\epsilon}}_{t+\Delta t}^p$ should simultaneously satisfy the algorithmic constitutive model and the finite element equilibrium equations. Instead of using the nested iteration scheme, Hughes and Taylor [31] developed a simultaneous iteration scheme to communicate between the global and local level calculations. In their simultaneous iteration scheme, the algorithmic constitutive model is linearized using a truncated Taylor series of the inelastic strain rate in order to avoid the local level iteration.

3.3.3 Mixed implicit-explicit time integration / alternating implicit-explicit scheme

Three types of mixed implicit-explicit time integration schemes have been developed to take the advantage of both the implicit and explicit time integration schemes.

The first is the forward gradient method [10, 17, 32-35]. In this scheme, the algorithmic constitutive equations are linearized to avoid expensive global-level iterations. Local level iteration is avoided by implicit integration of the inelastic strain rates and expansion of at least one of the state variables in a truncated Taylor series about the current time step. Time step size restriction for stability is less stringent than the explicit Euler scheme, although these semi-implicit schemes are still conditionally stable. Their shortcoming is less accuracy over the knee of the stress-strain curve, which leads to inaccurate solutions for large time step size or large strain increment.

The second method is the spatial-explicit-implicit scheme in which the space domain is divided into an implicit part and an explicit part. Chen and Hsu [36] employed this scheme for creep stress analysis. However, for complex thermo-mechanical processes such as casting, this scheme is obviously not suitable due to the difficulty of separating space domain into implicit and explicit parts.

The last mixed time-integration scheme is the alternating implicit-explicit scheme. This scheme is based on an operator-splitting technique which alternates between implicit and explicit forms of the total strain rate and inelastic strain rate in two time steps when evaluating the time integrals in Eqs.(3.13). Glowinski and Talle [15] used this scheme to integrate a steady state creep model with a constant elastic tensor and no thermal strain, which is a special case of the constitutive model in the present study. This scheme originated from the well-known ADI scheme of Douglas and Rachford [37] for spatial integration of the transient heat conduction problems. The most attractive feature of this scheme is avoiding expensive global-level iteration without incurring the numerical instability problems of conditional stability inherent to fully explicit schemes. This scheme is similar to the forward Euler integration algorithm with non-iterative sub-incrementing, which has been found to be computationally efficient for some viscoplastic analysis [9, 38, 39]. However, instead of using sub-incrementing for local level numerical

integration, the unconditionally stable backward Euler method is used to integrate the inelastic strain rate in this scheme. This makes the solution more reliable and accurate at the price of local level iteration. This relatively new two-step time integration is the third scheme evaluated in this study.

In the first “local” step, stress and inelastic strain rate are estimated through implicit time integration at each material point, knowing the total strain rate at time t from the previous time step:

$$\hat{\boldsymbol{\sigma}}_{t+\Delta t} = \mathbf{C}_{t+\Delta t} : [\boldsymbol{\epsilon}_t - \boldsymbol{\epsilon}_t^T - \boldsymbol{\epsilon}_t^p + (\dot{\boldsymbol{\epsilon}}_t - \dot{\boldsymbol{\epsilon}}^T - \sqrt{\frac{3}{2}} f(\hat{\boldsymbol{\sigma}}_{t+\Delta t}, \hat{\boldsymbol{\epsilon}}_{t+\Delta t}^p, T) \hat{\mathbf{N}}_{t+\Delta t}) \Delta t] , \quad (3.19)$$

$$\hat{\boldsymbol{\epsilon}}_{t+\Delta t}^p = \bar{\boldsymbol{\epsilon}}_t^p + f(\hat{\boldsymbol{\sigma}}_{t+\Delta t}, \hat{\boldsymbol{\epsilon}}_{t+\Delta t}^p, T) \Delta t . \quad (3.20)$$

In the second “global” step, stress and total strain rate are found through implicit spatial integration using the finite element method, based on explicit time integration using $\hat{\boldsymbol{\sigma}}_{t+\Delta t}$ and $\hat{\boldsymbol{\epsilon}}_{t+\Delta t}^p$ from step 1:

$$\boldsymbol{\sigma}_{t+\Delta t} = \mathbf{C}_{t+\Delta t} : [\boldsymbol{\epsilon}_t - \boldsymbol{\epsilon}_t^T - \boldsymbol{\epsilon}_t^p + (\dot{\boldsymbol{\epsilon}}_{t+\Delta t} - \dot{\boldsymbol{\epsilon}}^T - \sqrt{\frac{3}{2}} f(\hat{\boldsymbol{\sigma}}_{t+\Delta t}, \hat{\boldsymbol{\epsilon}}_{t+\Delta t}^p, T) \hat{\mathbf{N}}_{t+\Delta t}) \Delta t] . \quad (3.21)$$

In these equations, \wedge represents intermediate, estimated terms.

In the first step, total strain rates based on the known incremental displacement field calculated in the previous time step are used to update the current stress and inelastic strain at each material point. Eqs. (3.19)-(3.20) and (3.6-3.10) thus constitute a system of nonlinear equations with 15 unknowns (two tensors and three scalars) to find at every material point of a three dimensional analysis. Various constitutive algorithms, which will be discussed in the next section, may be used to calculate these stress and inelastic strain. The same local level calculations are needed in the implicit backward Euler scheme in section (3.32). Details of this solution procedure are given in the next section.

In the second step, the inelastic strain rate is based on the estimate in the first step. Thus, Eq.(3.21) can be regarded as a simple elastic constitutive equation with an initial strain or initial stress. The current total strain rate is found by solving the elastic constitutive equation and the system equilibrium equations using a global numerical method for spatial integration such as the finite element method.

It should be noted that, $\hat{\boldsymbol{\sigma}}_{t+\Delta t}$, used to calculate the end of the increment inelastic strain in the second step of this scheme, does not satisfy the finite element equilibrium equations at either time $t+\Delta t$ or time t .

3.4 The constitutive algorithm

For both the backward Euler and the alternating implicit-explicit schemes, the nonlinear constitutive equations including Eqs.(3.17) and (3.19) should be solved for the current stress and inelastic strain, based on the estimated incremental strain from either the previous time step solution or the current time step solution. The method used to accomplish this is called the "constitutive" algorithm or the "local" algorithm.

Defining the estimated incremental strain as $\Delta \hat{\boldsymbol{\epsilon}}$, the nonlinear constitutive equations in section 3.3.2 and 3.3.3 can be rewritten as

$$\boldsymbol{\sigma}_{t+\Delta t} = \mathbf{C}_{t+\Delta t} : [\boldsymbol{\epsilon}_t - \boldsymbol{\epsilon}_t^T - \boldsymbol{\epsilon}_t^p + \Delta \hat{\boldsymbol{\epsilon}} - \dot{\boldsymbol{\epsilon}}^T \Delta t - \sqrt{\frac{3}{2}} f(\bar{\boldsymbol{\sigma}}_{t+\Delta t}, \bar{\boldsymbol{\epsilon}}_{t+\Delta t}^p, T) \mathbf{N}_{t+\Delta t} \Delta t], \quad (3.22)$$

$$\bar{\boldsymbol{\epsilon}}_{t+\Delta t}^p = \bar{\boldsymbol{\epsilon}}_t^p + f(\bar{\boldsymbol{\sigma}}_{t+\Delta t}, \bar{\boldsymbol{\epsilon}}_{t+\Delta t}^p, T) \Delta t. \quad (3.23)$$

For brevity, the intermediate stress and the inelastic strain corresponding to the estimate incremental strain $\Delta \hat{\boldsymbol{\epsilon}}$ are simply express as $\boldsymbol{\sigma}_{t+\Delta t}$, $\boldsymbol{\epsilon}_{t+\Delta t}^p$ in this section. Equations (3.22) and (3.23) constitute a system of nonlinear equations with 14 scalar unknowns (two tensors and two scalars) in a three dimensional analysis. This problem could be solved by various Newton-Raphson based iterative schemes [5, 6, 11, 12, 23, 24, 28, 39, 40],

successive substitution [21] or the Nemat-Nasser's non-iterative scheme [41, 42]. With so many unknowns, this would be very computationally expensive however. Several attempts have been made to reduce the number of unknowns in this local level calculation. Hornberger and Stamm [11] used a projection method to transform an algorithmic constitutive model, based on Robinson's viscoplastic model by generalized midpoint rule, into only two nonlinear equations with two unknowns. Considering that the inelastic flow direction can be determined before solving any nonlinear equations when using the generalized trapezoidal rule for von Mises flow, Lush et al [24] reduced an isotropic single internal variable model into two scalar equations. Furthermore, the number of unknowns can be reduced to 1 when implicit integrating the inelastic strain rate and explicit integrating the internal variable rate at the same time [25, 43]. Walker et al [38, 44] proposed an asymptotic integration algorithm by recasting the state evolution equation into integral form and approximating the integrals as a uniformly valid asymptotic series. This reduced a class of state-variable based viscoplastic models from 19 for 3D problem [39] to 3 unknowns.

In this work, equations (3.22) and (3.23) are transformed into two unknown equations following a method similar to that of Lush [24].

Substituting Eqs. (3.3) into Eqs. (3.22), gives:

$$\boldsymbol{\sigma}_{t+\Delta t} = \boldsymbol{\sigma}_{t+\Delta t}^* - \sqrt{6} \mu_{t+\Delta t} f(\bar{\boldsymbol{\sigma}}_{t+\Delta t}, \bar{\boldsymbol{\epsilon}}_{t+\Delta t}^p, T) \mathbf{N}_{t+\Delta t} \Delta t, \quad (3.24)$$

where

$$\boldsymbol{\sigma}_{t+\Delta t}^* = \mathbf{C}_{t+\Delta t} : [\boldsymbol{\epsilon}_t - \boldsymbol{\epsilon}_t^T - \boldsymbol{\epsilon}_t^p + \Delta \hat{\boldsymbol{\epsilon}} - \dot{\boldsymbol{\epsilon}}^T \Delta t]. \quad (3.25)$$

By taking the deviatoric part of (3.24), substituting $\boldsymbol{\sigma}_{t+\Delta t}' = \sqrt{\frac{2}{3}} \bar{\boldsymbol{\sigma}}_{t+\Delta t} \mathbf{N}_{t+\Delta t}$, gives:

$$\boldsymbol{\sigma}_{t+\Delta t}^{*'} = \left(\sqrt{\frac{2}{3}} \bar{\boldsymbol{\sigma}}_{t+\Delta t} + \sqrt{6} \mu_{t+\Delta t} f(\bar{\boldsymbol{\sigma}}_{t+\Delta t}, \bar{\boldsymbol{\epsilon}}_{t+\Delta t}^p, T) \Delta t \right) \mathbf{N}_{t+\Delta t}, \quad (3.26)$$

which means that $\mathbf{N}_{t+\Delta t}$ and $\boldsymbol{\sigma}_{t+\Delta t}^{*,\prime}$ have the same direction. Thus ,

$$\mathbf{N}_{t+\Delta t} = \sqrt{\frac{3}{2}} \frac{\boldsymbol{\sigma}_{t+\Delta t}^{*,\prime}}{\bar{\sigma}_{t+\Delta t}^*} , \quad (3.27)$$

and

$$\boldsymbol{\sigma}_{t+\Delta t}^{*,\prime} = \bar{\sigma}_{t+\Delta t}^* \frac{\boldsymbol{\sigma}_{t+\Delta t}^{*,\prime}}{\bar{\sigma}_{t+\Delta t}^*} . \quad (3.28)$$

Combining Eqs. (3.26) and (3.28) produces:

$$\bar{\sigma}_{t+\Delta t}^* = \bar{\sigma}_{t+\Delta t}^* - 3 \mu_{t+\Delta t} f(\bar{\sigma}_{t+\Delta t}^*, \bar{\epsilon}_{t+\Delta t}^p, T) \Delta t . \quad (3.29)$$

Equations (3.29) and (3.23) form a pair of nonlinear scalar equations with two unknowns $\bar{\sigma}_{t+\Delta t}^*$ and $\bar{\epsilon}_{t+\Delta t}^p$.

Summary of the constitutive algorithm

Step 1. Estimate incremental strain $\Delta \hat{\boldsymbol{\epsilon}}$ from the incremental displacement at time t or current time $t+\Delta t$.

Step 2. Calculate $\boldsymbol{\sigma}_{t+\Delta t}^*$ using equation (3.25) .

Step 3. Calculate the deviatoric part and the effective stress of $\boldsymbol{\sigma}_{t+\Delta t}^*$.

Step 4. Solve equations (3.29) and (3.23) for $\bar{\sigma}_{t+\Delta t}^*$ and $\bar{\epsilon}_{t+\Delta t}^p$.

Step 5. Calculate stress $\boldsymbol{\sigma}_{t+\Delta t}$ by:

$$\boldsymbol{\sigma}_{t+\Delta t} = \bar{\sigma}_{t+\Delta t}^* \frac{\boldsymbol{\sigma}_{t+\Delta t}^{*,\prime}}{\bar{\sigma}_{t+\Delta t}^*} + \frac{1}{3} \text{tr}(\boldsymbol{\sigma}_{t+\Delta t}^*) \boldsymbol{\delta} .$$

Step 6. Calculate $\dot{\bar{\epsilon}}_{t+\Delta t}^p$ and $\bar{\epsilon}_{t+\Delta t}^p$.

The problem in step 4 is very similar to a uniaxial problem with prescribed strain rate which is integrated by the implicit backward Euler scheme. It is necessary to develop a solution strategy for the nonlinear equations in step 4. Several methods including the successive substitution, the Newton-Raphson method, the forward gradient method, the bounded Newton-Raphson method and the Nemat-Nasser's explicit prediction method are implemented and compared in this study. Although the problem in step 4 can be further simplified as a nonlinear equation with one unknown, all methods except the bounded Newton-Raphson method are still based on the original equations with two unknowns in step 4 in order to illustrate their physical nature.

Rewriting the equations in step 4, gives:

$$\mathbf{y} = \mathbf{g}(\mathbf{y}) , \quad (3.30)$$

in which $\mathbf{y} = (y_1, y_2)^T = (\bar{\sigma}_{t+\Delta t}, \bar{\epsilon}_{t+\Delta t}^p)^T$ and $\mathbf{g} = (g_1, g_2)^T$ are defined as

$$y_1 = g_1(y_1, y_2) = \bar{\sigma}_{t+\Delta t} = \bar{\sigma}_{t+\Delta t}^* - 3 \mu_{t+\Delta t} f(\bar{\sigma}_{t+\Delta t}, \bar{\epsilon}_{t+\Delta t}^p, T) \Delta t , \quad (3.31)$$

$$y_2 = g_2(y_1, y_2) = \bar{\epsilon}_{t+\Delta t}^p = \bar{\epsilon}_t^p + f(\bar{\sigma}_{t+\Delta t}, \bar{\epsilon}_{t+\Delta t}^p, T) \Delta t . \quad (3.32)$$

If an iterative method is employed to solve Eqs. (3.30), convergence criteria is selected as

$$|\mathbf{e}| = |\mathbf{y} - \mathbf{g}(\mathbf{y})| \leq 10^{-5} \mathbf{y}_c , \quad (3.33)$$

in which $\mathbf{y}_c = (\bar{\sigma}_{t+\Delta t}^*, \bar{\epsilon}_t^p)^T$ is the characteristic magnitude of \mathbf{y} .

3.4.1 The successive substitution (Picard method)

Successive substitution is the simplest iterative method. The value of \mathbf{y} at $(i+1)$ -th iteration is defined from \mathbf{y} at the i -th iteration

$$\mathbf{y}^{i+1} = \mathbf{g}(\mathbf{y}^i) , \quad (3.34)$$

with $\mathbf{y}^0 = (\bar{\boldsymbol{\sigma}}_t, \bar{\boldsymbol{\varepsilon}}_t^p)^T$.

This method is fast and easy to code but the convergence rate is slow and divergence may occur for large time step sizes when the nonlinearity is great [45]. Numerical experiments for rate-dependent constitutive models reached a similar conclusion. Cormeau found that the unconditional stable backward Euler integration scheme with this method as the constitutive algorithm suffers from a similar time-step restriction as the forward Euler scheme algorithm due to convergence problems [21]. Krieg also showed an example where this method fails to converge [5].

3.4.2 The Newton-Raphson method

This method is known to have a fast convergence rate. Iteration proceeds as follows:

$$\mathbf{y}^{i+1} = \mathbf{y}^i + (\mathbf{g}(\mathbf{y}^i) - \mathbf{y}^i) (\mathbf{I}_2 - \frac{\partial \mathbf{g}}{\partial \mathbf{y}}(\mathbf{y}^i))^{-1} , \quad (3.35)$$

with $\mathbf{y}^0 = (\bar{\boldsymbol{\sigma}}_t, \bar{\boldsymbol{\varepsilon}}_t^p)^T$, where \mathbf{I}_2 is an identity matrix of order 2 and the Jacobian $\frac{\partial \mathbf{g}}{\partial \mathbf{y}}$ is a 2×2 matrix. This method requires a substantial additional computational effort to evaluate the Jacobian $\frac{\partial \mathbf{g}}{\partial \mathbf{y}}$ and to invert the matrix $(\mathbf{I}_2 - \frac{\partial \mathbf{g}}{\partial \mathbf{y}}(\mathbf{y}^i))$ at each iteration.

3.4.3 The forward gradient method

Instead of solving the nonlinear Eqs. (3.30) directly, it is linearized by using a truncated Taylor series to approximate \mathbf{g} at reference point $\mathbf{y}^0 = (\bar{\boldsymbol{\sigma}}_t, \bar{\boldsymbol{\varepsilon}}_t^p)^T$,

$$\mathbf{y} = \mathbf{g}(\mathbf{y}^0) + \frac{\partial \mathbf{g}}{\partial \mathbf{y}}(\mathbf{y}^0)(\mathbf{y} - \mathbf{y}^0) . \quad (3.36)$$

Solving linear equation (3.36), obtained:

$$\mathbf{y} = (\mathbf{g}(\mathbf{y}^0) - \mathbf{y}^0 \frac{\partial \mathbf{g}}{\partial \mathbf{y}}(\mathbf{y}^0))(\mathbf{I}_2 - \frac{\partial \mathbf{g}}{\partial \mathbf{y}}(\mathbf{y}^0))^{-1} . \quad (3.37)$$

It is obvious that this method only approximates the solution, but it has the advantage of no iteration. This method is just the first iteration of the Newton-Raphson method.

3.4.4 The bounded Newton-Raphson method

Due to the very stiff nature of most rate-dependent constitutive models, the Newton-Raphson method with 2 unknowns equations may still cause the convergence problems [46]. This problem can be improved by a bounded N-R algorithm based on the dual forms of unified constitutive models including a stress driven form and a strain driven form [46].

Eqs. (3.31) and (3.32) can be further transformed as

$$y_2 = y_2(y_1) = \bar{\epsilon}_t^p - \frac{y_1 - \bar{\sigma}_{t+\Delta t}^*}{3 \mu_{t+\Delta t}} , \quad (3.38)$$

$$y_1 = \bar{\sigma}_{t+\Delta t}^* - 3 \mu_{t+\Delta t} f(y_1, y_2(y_1)) \Delta t . \quad (3.39)$$

Equation (3.39) is a nonlinear equation with only one unknown y_1 . Lush et al [24] developed a two-level iterative scheme based on the bounded Newton-Raphson method to solve their governing equations with two unknowns of the effective stress and structure variable. This is found more efficient and robust than either the standard Newton-Raphson method or the forward gradient method. Here, a similar scheme is implemented to solve equation (3.39).

At first, the lower bound $y_{1\text{-lower}}$ and the upper bound $y_{1\text{-upper}}$ are initialized, assuring y_1, y_2 and f are always positive,

$$y_1 \leq \bar{\sigma}_{t+\Delta t}^* , \quad (3.40)$$

$$f(y_1, y_2(y_1)) \leq \frac{\bar{\sigma}_{t+\Delta t}^*}{3 \mu_{t+\Delta t} \Delta t} , \quad (3.41)$$

$$y_2 \leq \bar{\epsilon}_t^p + \frac{\bar{\sigma}_{t+\Delta t}^*}{3 \mu_{t+\Delta t}} . \quad (3.42)$$

Assuming that equation (3.10) can be inverted as

$$\bar{\sigma} = f^{-1}(\dot{\bar{\epsilon}}^p, \bar{\epsilon}^p) , \quad (3.43)$$

Equation (3.41) and (3.42) give

$$y_1 \leq f^{-1} \left(\frac{\bar{\sigma}_{t+\Delta t}^*}{3 \mu_{t+\Delta t} \Delta t} , \bar{\epsilon}_t^p + \frac{\bar{\sigma}_{t+\Delta t}^*}{3 \mu_{t+\Delta t}} \right) , \quad (3.44)$$

in which f^{-1} is assumed to be a incremental function with respect to $\dot{\bar{\epsilon}}^p$ and $\bar{\epsilon}^p$. Equation (3.40) and (3.41) correspond to the two limiting cases where elastic and inelastic strain increments dominate the respond respectively. Thus we can initialize

$$y_{1\text{-lower}} = 0 , \quad (3.45)$$

$$y_{1\text{-upper}} = \min \left(\bar{\sigma}_{t+\Delta t}^* , f^{-1} \left(\frac{\bar{\sigma}_{t+\Delta t}^*}{3 \mu_{t+\Delta t} \Delta t} , \bar{\epsilon}_t^p + \frac{\bar{\sigma}_{t+\Delta t}^*}{3 \mu_{t+\Delta t}} \right) \right) . \quad (3.46)$$

Applying the Newton-Raphson scheme to Eq.(3.39), the Newton-Raphson correction for the i -th iteration $\Delta y_{1\text{-NR}}^i$ is obtained as

$$\Delta y_{1-NR}^i = \frac{\bar{\sigma}_{t+\Delta t}^* - 3 \mu_{t+\Delta t} \Delta t f(y_1^i, y_2(y_1^i)) - y_1^i}{1 + 3 \mu_{t+\Delta t} \Delta t \frac{\partial f}{\partial y_1}(y_1^i, y_2(y_1^i)) - \Delta t \frac{\partial f}{\partial y_2}(y_1^i, y_2(y_1^i))} , \quad (3.47)$$

The maximum allowable correction Δy_{1-max}^i is calculated using a quasi-bisection scheme. If $\Delta y_{1-NR}^i < 0$, then set

$$y_{1-upper} = y_1^i , \quad (3.48)$$

and the maximum allowable correction is

$$\Delta y_{1-max}^i = \frac{1}{2} (y_{1-lower} - y_1^i) ; \quad (3.49)$$

If $\Delta y_{1-NR}^i > 0$, then set

$$y_{1-lower} = y_1^i , \quad (3.50)$$

and the maximum allowable correction is

$$\Delta y_{1-max}^i = (y_{1-upper} - y_1^i) . \quad (3.51)$$

The correction Δy_1^i is determined as

$$\Delta y_1^i = \Delta y_{1-max}^i , \text{ if } |\Delta y_{1-NR}^i| > |\Delta y_{1-max}^i|. \quad (3.52)$$

Otherwise,

$$\Delta y_1^i = \Delta y_{1-NR}^i . \quad (3.56)$$

Finally, y_1^{i+1} is updated :

$$y_1^{i+1} = y_1^i + \Delta y_1^i . \quad (3.57)$$

The corresponding y_2^{i+1} is calculated from equation (3.38).

3.4.5 The Nemat-Nasser's explicit prediction method

Nemat-Nasser et al [41, 42] developed an explicit constitutive algorithm for their isothermal hypoelastic-viscoplastic models. Their algorithm includes a plastic predictor followed by an elastic corrector and can be considered as a special case of forward gradient method with the proper initial solution by exploiting the fact that most of the deformation in incremental inelastic deformation is due to plastic flow with a very small elastic deformation. Based on their numerical experiments for several constitutive models, they concluded this algorithm is robust, stable and very accurate for any large or small time increments. The appealing aspect of this algorithm is its "explicit" characteristic, which means no iteration in the local level calculation.

Following the process they employed, a temperature-dependent version for hyperelastic-viscoplastic models is obtained to solve the problem in step 4.

Rearrange equation (3.29) as

$$\bar{\sigma}_{t+\Delta t} - \bar{\sigma}_t = 3 \mu_{t+\Delta t} \Delta t (\dot{\bar{\epsilon}}_{t+\Delta t}^0 - \dot{\bar{\epsilon}}_{t+\Delta t}^p), \quad (3.58)$$

in which the initial approximation of the inelastic strain rate $\dot{\bar{\epsilon}}_{t+\Delta t}^0$ is defined

$$\dot{\bar{\epsilon}}_{t+\Delta t}^0 = \frac{\bar{\sigma}_{t+\Delta t}^* - \bar{\sigma}_t}{3 \mu_{t+\Delta t} \Delta t}, \quad (3.59)$$

initial approximations of the effective inelastic strain and the effective stress from equations (3.23) and (3.43) are obtained:

$$\bar{\epsilon}_{t+\Delta t}^0 = \bar{\epsilon}_t^p - \dot{\bar{\epsilon}}_{t+\Delta t}^0 \Delta t, \quad (3.60)$$

$$\bar{\sigma}_{t+\Delta t}^0 = f^{-1}(\dot{\bar{\epsilon}}_{t+\Delta t}^0, \bar{\epsilon}_{t+\Delta t}^0). \quad (3.61)$$

Approximating f^{-1} in equation (3.43) at time $t+\Delta t$ by a truncated Taylor series t with the initial approximations of inelastic strain rate and effective inelastic strain as,

$$\bar{\sigma}_{t+\Delta t} = \bar{\sigma}_{t+\Delta t}^0 + \frac{\partial f^{-1}}{\partial \bar{\epsilon}^p} \Big|_0 (\dot{\bar{\epsilon}}_{t+\Delta t}^p - \dot{\bar{\epsilon}}_{t+\Delta t}^{p0}) + \frac{\partial f^{-1}}{\partial \bar{\epsilon}^p} \Big|_0 (\bar{\epsilon}_{t+\Delta t}^p - \bar{\epsilon}_{t+\Delta t}^{p0}), \quad (3.62)$$

combining Eqs. (3.62), (3.60), (3.58) and (3.23), the effective stress and the effective inelastic strain are updated as follows:

$$\bar{\sigma}_{t+\Delta t} = \frac{\eta \bar{\sigma}_t + \bar{\sigma}_{t+\Delta t}^0}{1 + \eta}, \quad (3.63)$$

$$\bar{\epsilon}_{t+\Delta t}^p = \bar{\epsilon}_t^p + \dot{\bar{\epsilon}}_{t+\Delta t}^{p0} \Delta t - \frac{\bar{\sigma}_{t+\Delta t}^0 - \bar{\sigma}_t}{3 \mu_{t+\Delta t} (1 + \eta)}, \quad (3.64)$$

where

$$\eta = \left(\frac{\partial f^{-1}}{\partial \bar{\epsilon}^p} \Big|_0 \frac{1}{\Delta t} + \frac{\partial f^{-1}}{\partial \bar{\epsilon}^p} \Big|_0 \right) \frac{1}{3 \mu_{t+\Delta t}}. \quad (3.65)$$

Eqs. (3.63)-(3.65) give an approximate solution for step 4 when the material response is essential inelastic. Compared with the forward gradient method discussed in section 3.4.3, this method has a relative "good" reference point for the truncated Taylor series.

Once the material response is essential elastic, which is characterized by the condition $\bar{\epsilon}_{t+\Delta t}^p < \bar{\epsilon}_t^p$ from equation (3.64), the alternative solution suggested by Nemat-Nasser et al [42] is

$$\bar{\sigma}_{t+\Delta t} = \bar{\sigma}_{t+\Delta t}^* - 3 \mu_{t+\Delta t} f(\bar{\sigma}_t, \bar{\epsilon}_t^p, T) \Delta t, \quad (3.66)$$

$$\bar{\epsilon}_{t+\Delta t}^p = \bar{\epsilon}_t^p + f(\bar{\sigma}_t, \bar{\epsilon}_t^p, T) \Delta t. \quad (3.67)$$

3.5 Spatial integration / finite element implementation

The different time-integration schemes must be implemented into a numerical scheme for spatial integration. The standard finite element method is employed in this work.

Using the standard Galerkin's method[47], the quasi-static boundary value problem can be transformed into the following system of algebraic equations at each node in the finite element domain:

$$\sum_{e=1}^{ne} \int_{V_e} ([B]^e)^T \{\sigma\} dV = \sum_{e=1}^{ne} \int_{V_e} ([N]^e)^T \mathbf{b} dV + \sum_{e=1}^{ne} \int_{A_{te}} ([N]^e)^T \mathbf{\bar{t}} dA , \quad (3.68)$$

in which ne is total number of elements, the summation symbol represents the global assembly operation, $[B]^e$ is the standard strain-displacement matrix for element e defined by spatial differentiation of the shape functions, $[N]^e$ is the shape function matrix for the element e , $\{\sigma\}$ is a 6x1 component vector for the stress tensor, $\{\sigma\} = \{\sigma_{11}, \sigma_{22}, \sigma_{33}, \sigma_{12}, \sigma_{23}, \sigma_{31}\}^T$, \mathbf{b} represents the body force vector and $\mathbf{\bar{t}}$ expresses the prescribed surface traction on domain boundaries. The left hand side of the equation is the internal force vector and the right-hand side of the equation is the applied load vector. This equilibrium equation must be satisfied at every time step of the simulation.

Various global solution procedures have been developed for global-level iteration with the finite element method when non-linear materials are simulated [16, 19, 24]. These include the tangent stiffness method or fully Newton-Raphson method and the initial strain method or modified Newton-Raphson method. The former is widely used for plasticity problems while the latter is popular for creep analysis. One advantage of the initial strain method is that the global stiffness matrix remains constant for each iteration although it is partially offset by its lower convergence rate which is best at linear. The tangent stiffness method, on the other hand, must reform the global stiffness matrix for

each iteration at given time step but its convergence rate is asymptotic quadratic as compensation. It should be pointed out that , to maintain the quadratic rate of asymptotic convergence for fully Newton-Raphson method, the tangent operator must be consistent with the numerical method employed to integrate the inelastic strain rate equation [24, 48-50]. Consistency implies that the stress increment predicted by the tangent operator acting on the strain increment matches the stress increment predicted by the integration procedure to first order [49]. In this investigation, the initial strain method is employed.

Substituting the algorithmic constitutive models from the numerical integration schemes discussed in section 3 into the finite element equilibrium equation (3.68) at time $t+\Delta t$ and using the strain / displacement relation

$$\{\Delta \boldsymbol{\epsilon}\}^e = [\mathbf{B}]^e \{\Delta \mathbf{u}\}^e , \quad (3.69)$$

the following algebraic system of finite element equations is obtained:

$$\begin{aligned} \sum_{e=1}^{ne} \int_{V_e} ([\mathbf{B}]^e)^T [\mathbf{C}] [\mathbf{B}]^e dV \{\Delta \mathbf{u}\}_{t+\Delta t} &= \sum_{e=1}^{ne} \int_{V_e} ([\mathbf{N}]^e)^T \mathbf{b} dV + \sum_{e=1}^{ne} \int_{A_{te}} ([\mathbf{N}]^e)^T \mathbf{t} dA \\ &- \sum_{e=1}^{ne} \int_{V_e} ([\mathbf{B}]^e)^T \{\boldsymbol{\sigma}\} dV + \sum_{e=1}^{ne} \int_{V_e} ([\mathbf{B}]^e)^T [\mathbf{C}] \{\Delta \boldsymbol{\epsilon}\} dV , \end{aligned} \quad (3.70)$$

in which $[\mathbf{C}]$ is the matrix form of the 4th order elastic tensor at time $t+\Delta t$, $\{\boldsymbol{\sigma}\}$ and $\{\Delta \boldsymbol{\epsilon}\}$ are current estimate of the stress and incremental strain vectors. This will be discussed respectively for each numerical integration scheme.

For the explicit Euler forward scheme,

$$\Delta \boldsymbol{\epsilon} = \dot{\boldsymbol{\epsilon}}_t \Delta t , \quad (3.71)$$

$$\boldsymbol{\sigma} = \mathbf{C}_{t+\Delta t} : [\boldsymbol{\epsilon}_t - \boldsymbol{\epsilon}_t^T - \boldsymbol{\epsilon}_t^p + \Delta \boldsymbol{\epsilon} - \dot{\boldsymbol{\epsilon}}^T \Delta t - \sqrt{\frac{3}{2}} \dot{\boldsymbol{\epsilon}}^p_t \mathbf{N}_t \Delta t] . \quad (3.72)$$

For the alternating implicit-explicit scheme,

$$\Delta \boldsymbol{\varepsilon} = \dot{\boldsymbol{\varepsilon}}_t \Delta t, \quad (3.73)$$

$$\boldsymbol{\sigma} = \hat{\boldsymbol{\sigma}}_{t+\Delta t} = \mathbf{C}_{t+\Delta t} : [\boldsymbol{\varepsilon}_t - \boldsymbol{\varepsilon}_t^T - \boldsymbol{\varepsilon}_t^p + \Delta \boldsymbol{\varepsilon} - \dot{\boldsymbol{\varepsilon}}^T \Delta t - \sqrt{\frac{3}{2}} f(\hat{\boldsymbol{\sigma}}_{t+\Delta t}, \hat{\boldsymbol{\varepsilon}}_{t+\Delta t}^p, T) \hat{\mathbf{N}}_{t+\Delta t} \Delta t], \quad (3.74)$$

in which $\hat{\boldsymbol{\sigma}}_{t+\Delta t}$ is calculated at the first step of this scheme.

For both of the above time integration schemes, the equation (3.70) is a system of linear equations to solve for the incremental displacements.

For the implicit backward Euler scheme,

$$\Delta \boldsymbol{\varepsilon} = \Delta \boldsymbol{\varepsilon} = \dot{\boldsymbol{\varepsilon}}_{t+\Delta t} \Delta t, \quad (3.75)$$

$$\boldsymbol{\sigma} = \boldsymbol{\sigma}_{t+\Delta t} = \mathbf{C}_{t+\Delta t} : [\boldsymbol{\varepsilon}_t - \boldsymbol{\varepsilon}_t^T - \boldsymbol{\varepsilon}_t^p + \Delta \boldsymbol{\varepsilon} - \dot{\boldsymbol{\varepsilon}}^T \Delta t - \sqrt{\frac{3}{2}} f(\bar{\boldsymbol{\sigma}}_{t+\Delta t}, \bar{\boldsymbol{\varepsilon}}_{t+\Delta t}^p, T) \mathbf{N}_{t+\Delta t} \Delta t], \quad (3.76)$$

equation (3.70) becomes nonlinear so has to be solved in an iterative manner due to the coupling of $\Delta \boldsymbol{\varepsilon}$ and $\boldsymbol{\sigma}$ with the current incremental displacement. Assuming $\boldsymbol{\sigma}^{(k)}$ is the solution from local level calculation with the k th estimate of the incremental strain $\Delta \boldsymbol{\varepsilon}^{(k)}$, the $(k+1)$ th equilibrium iteration is carry out by solving the following system of linear equations:

$$\begin{aligned} \sum_{e=1}^{ne} \int_{V_e} ([\mathbf{B}]^e)^T [\mathbf{C}] [\mathbf{B}]^e dV \{\Delta \mathbf{u}\}_{t+\Delta t}^{(k+1)} &= \sum_{e=1}^{ne} \int_{V_e} ([\mathbf{N}]^e)^T \mathbf{b} dV + \sum_{e=1}^{ne} \int_{A_{te}} ([\mathbf{N}]^e)^T \mathbf{t} dA \\ &- \sum_{e=1}^{ne} \int_{V_e} ([\mathbf{B}]^e)^T \{\boldsymbol{\sigma}^{(k)}\} dV + \int_{V_e} ([\mathbf{B}]^e)^T [\mathbf{C}] \{\Delta \boldsymbol{\varepsilon}^{(k)}\} dV. \end{aligned} \quad (3.76)$$

After updating the estimated incremental strain $\Delta \boldsymbol{\varepsilon}^{(k+1)}$ with the incremental displacement $\{\Delta \mathbf{u}\}_{t+\Delta t}^{(k+1)}$ from the $(k+1)$ th equilibrium iteration, $\boldsymbol{\sigma}^{(k+1)}$ is obtained using a proper constitutive algorithm for the current estimate $\Delta \boldsymbol{\varepsilon}^{(k+1)}$ of the incremental strain to satisfy the algorithmic constitutive model at every material point. This process is repeated with k until the equilibrium iteration converges within a specified tolerance of equation (3.70) with $\boldsymbol{\sigma}^{(k+1)}$.

From the above discussion, it is clear that the alternating implicit-explicit scheme requires only the first equilibrium iteration part of the solution procedure of the backward Euler scheme.

3.6 Results and discussion

3.6.1 Specified constitutive models

Two constitutive models used in our example problems can be written in the following form:

$$\dot{\bar{\epsilon}}^p = f(\bar{\sigma}, \bar{\epsilon}^p, T) = A \times [\max(\bar{\sigma}, \sigma_Y) - \sigma_Y]^n. \quad (3.78)$$

The first model is the rate-dependent elastic-viscoplastic model III of Kozłowski [4]. This model was developed to match tensile test results of Wray [51] and creep data of Suzuki [52] over a wide range of strain rates and high temperature (T (k)) and varying carbon contents (%C) for plain-carbon steel under continuous casting conditions:

$$A = f_c \exp\left(-\frac{Q}{T}\right),$$

$$\sigma_Y = f_1 \bar{\epsilon}^{f_2},$$

$$n = f_3,$$

where

$$Q = 44650 \text{ (K}^{-1}\text{)},$$

$$f_c = 4.655 \times 10^4 + 7.14 \times 10^4 (\%C) + 1.2 \times 10^5 (\%C)^2,$$

$$f_1 = 130.5 - 5.128 \times 10^{-3} T,$$

$$f_2 = -0.6289 + 1.114 \times 10^{-3} T,$$

$$f_3 = 8.132 - 1.54 \times 10^{-3} T .$$

The second model is a rate-independent elastic-perfectly-plastic model with temperature-dependent yield stress. This is transformed into an elastic-viscoplastic model using a penalty approach by setting $A = 1.0 \times 10^8$, $n = 5.0$ in equation (3.79). Although a first order power law with a very large fluidity constant A can accurately characterize the rate-independent material behavior [28], large n is used in order to increase the non-linearity and consequent numerical difficulties of the problem.

3.6.2 Uniaxial calculations

The performances of the discussed time integration schemes as well as the constitutive algorithms for the selected rate-dependent constitutive models were evaluated using uniaxial test problems with fixed total strain histories. Only the forward Euler and the backward Euler schemes are employed in this study because the alternative implicit-explicit scheme is exactly identical to the backward Euler scheme for this case. Numerical experiments for the tensile test and the stress relaxation test are reported here.

The first uniaxial problem involved a tensile test with constant strain rate (0.0024 sec^{-1}) until 6% total strain at 950°C for 0.005%C steel. An accurate reference solution was obtained using 25,000 time steps (2.4×10^{-6} strain increment) of the simple forward Euler scheme. Figure 3.1 shows the effective inelastic strain-stress curves with different time increments for the forward Euler scheme. It can be seen at least 250 time steps (2.4×10^{-4} strain increment) are needed to overcome the stability problems inherent in this scheme. Compared with the reference solution, the solution with 250 time steps is quite accurate with only 0.03% error in stress at 5% effective inelastic strain.

The backward Euler scheme with successive substitution failed to reach a converged solution with 250 time steps (2.4×10^{-4} strain increment). The solution from

500 time steps (1.2×10^{-4} strain increment) is same as the result from the forward Euler scheme with same number of time steps. The results from the backward Euler scheme with the forward gradient method are shown in Figure 3.2. It is clear that this method is less accuracy for relatively large time step sizes (i.e., 1.2×10^{-3} strain increment) during the knee range of the stress-strain curve. The Newton-Raphson method and the bounded Newton-Raphson method for the backward Euler scheme gave the same result (shown in Figure 3.3) without any convergence problem for any time step size. The results from just one time step or 6% strain increment showed that the relative error of the stress at 6% strain is just 0.18%. Corresponding to 5 time steps (1.2% strain increment) and 1 time step (6% strain increment), the total number of iterations for the one-unknown bounded Newton-Raphson scheme are 26 and 5 respectively as opposed to 38 and 31 of the two-unknowns Newton-Raphson scheme. For this test problem, the Nemat-Nasser's explicit prediction method employed in the backward Euler scheme also worked very well for different time steps including 6% strain increment. Some of the results from this method are illustrated Figure 3.4.

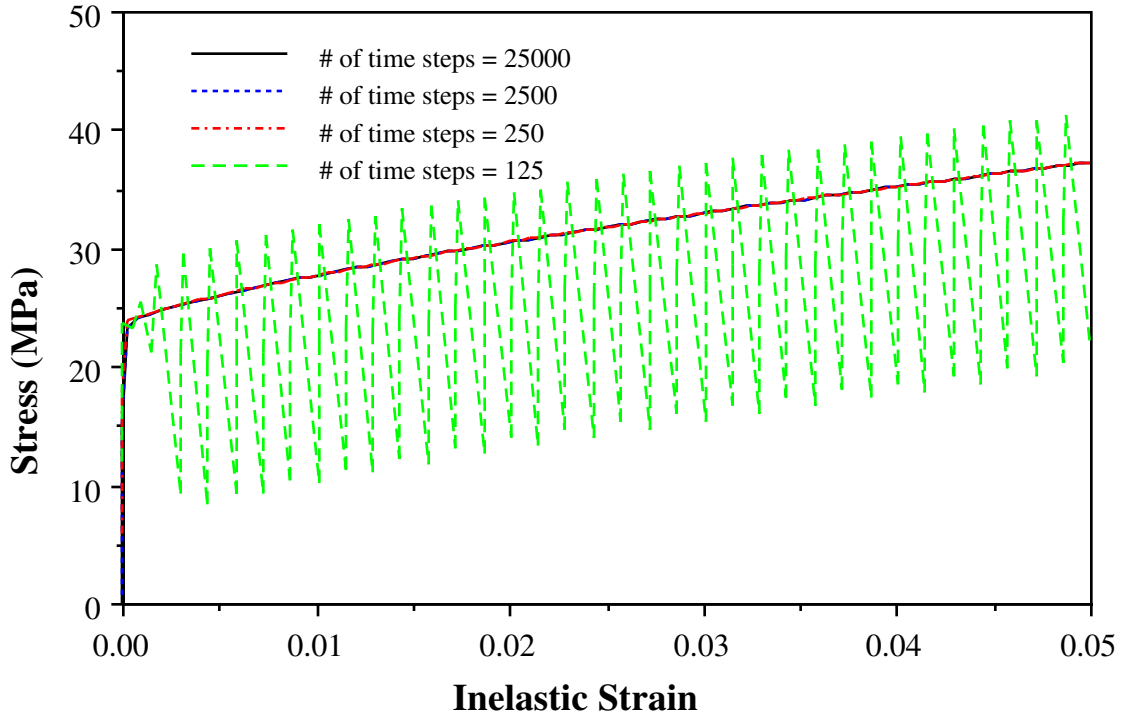


Figure 3.1 Uniaxial tension result from forward Euler scheme

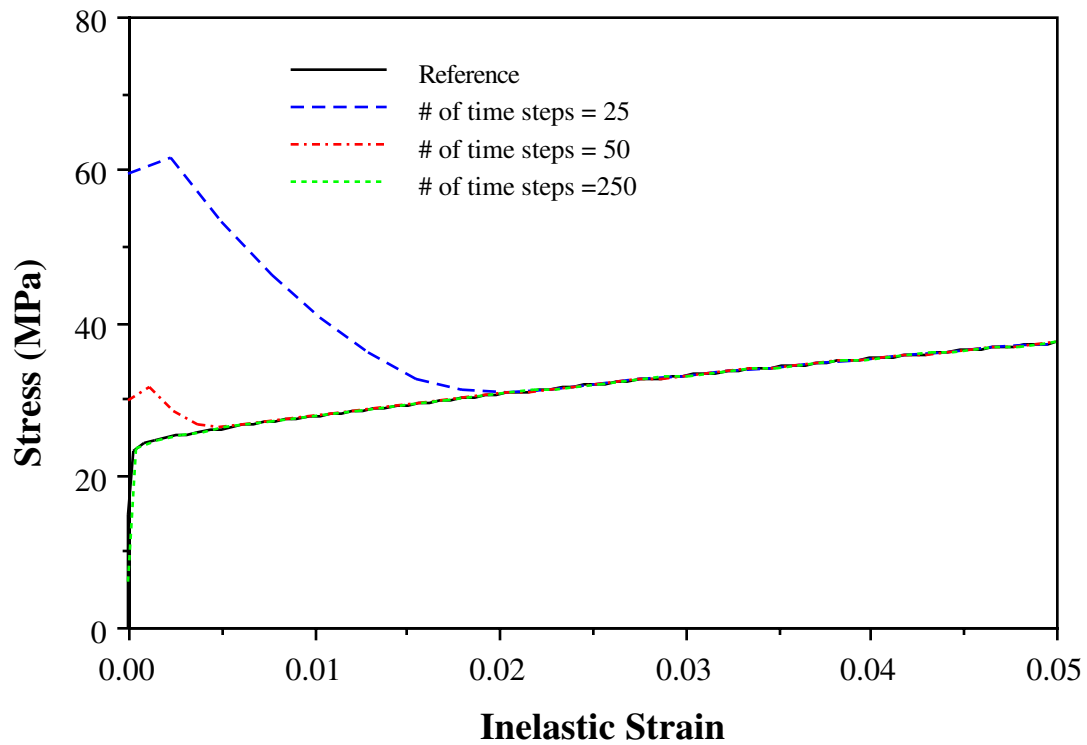


Figure 3.2 Uniaxial tension results from forward gradient method

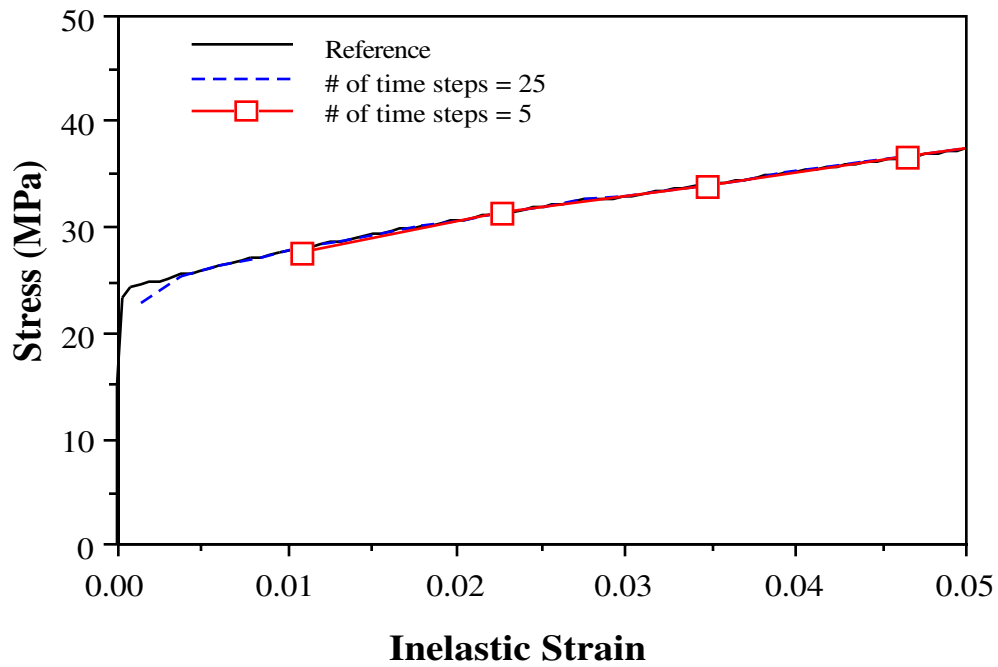


Figure 3.3 Uniaxial tension results from backward Euler scheme with N-R iteration

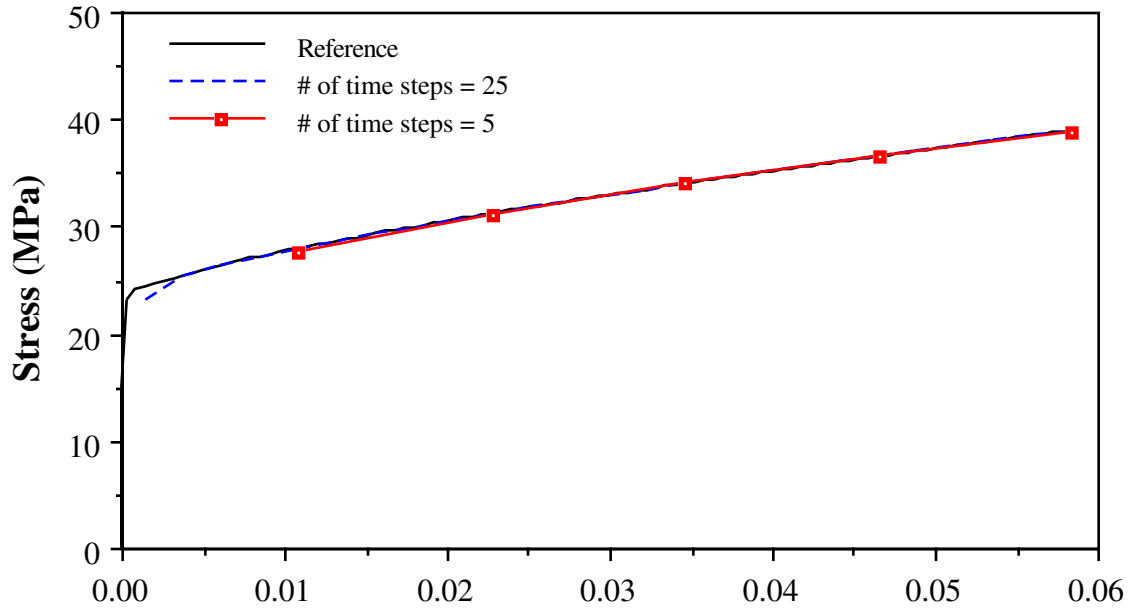


Figure 3.4 Uniaxial tension results from backward Euler scheme with Nemat-Nasser prediction method

The second uniaxial test problem simulated an abrupt change in load history. It started with 25 seconds tension with a constant strain rate 0.0004 sec^{-1} until total strain of 1% was reached at 900°C for 0.18%C steel. This was followed by 175 seconds of stress relaxation, with total strain remaining fixed at 1%. The reference solution gained from the forward Euler scheme with 200,000 time steps showed that the stress gradually increases for the first 25 seconds as the stress-strain curve is followed. Stopping the tension produced a rapid decrease in stress for the next 10 seconds then rapidly decreased in next 10 seconds, which levels towards a steady state solution, as shown in Figure 3.5. This figure also shows that the maximum time step size of the forward Euler scheme without the instability is 400 time steps.

Similar to the result of the tension test, the backward Euler scheme with the successive substitution method met a convergence problem with the relative small time step size (800 time steps) which is less than the critical time step size of the forward Euler

scheme. The results from the forward gradient method are showed in Figure 3.6. For this typical problem, the forward gradient method allowed relative large time step size (200 time steps) without the accuracy and stability problems. For large time step size (40 time steps) this scheme still suffered accuracy problems. In Figure 3.7, both Newton-Raphson type iterative methods in the backward Euler scheme captured the main phenomena even for large time step size (16 time steps or one time step during the tension region). However the accuracy of the stress during the range in which the stress rapidly decreases is relative lower. This is due to the first order characteristic of the backward Euler scheme and relative large time step size used here which spans whole transition range of the stress. Corresponding to 40 time steps and 16 time steps, the total iteration numbers of the one-unknown bounded Newton-Raphson scheme are 84 and 27 respectively as opposed to 128 and 52 of the two-unknowns Newton-Raphson. Unlike the result of the tension test, the Nemat-Nasser local method in the backward Euler scheme failed to produce the correct stress pattern during the relaxation range, although it exactly duplicated the results for the tension range as shown in Figure 3.8. This is partly because the reference point for the truncated Taylor series is not a good approximation for the case including the higher stress with zero strain rate.

From above uniaxial calculations, it can be concluded for the specified constitutive model that the backward Euler scheme with either the successive substitution method or the forward gradient method offer little or no advantage compared with the forward Euler scheme. Two type Newton-Raphson methods with the backward Euler scheme are robust and accurate although the bounded Newton-Raphson method is more efficient. The Nemat-Nasser's prediction method performed very well for the tension problem while it failed for the stress relaxation problem. Based on these results, several combined finite element schemes for the unified constitutive models will be further evaluated in the next example.

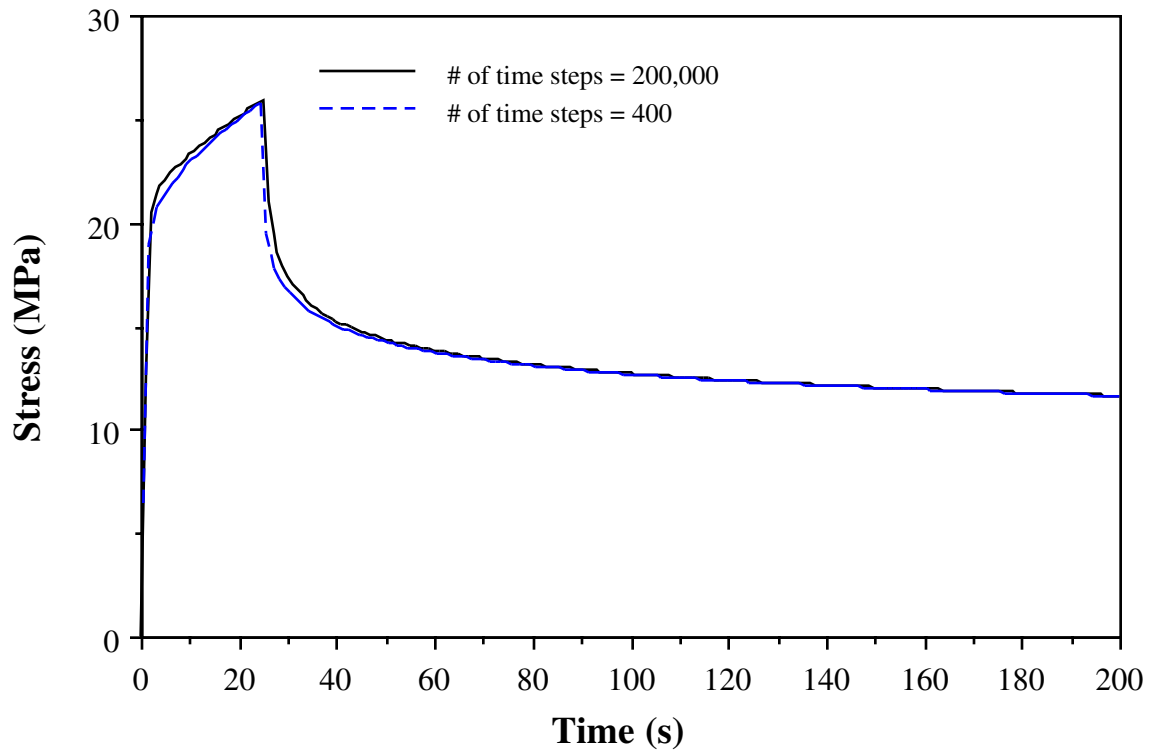


Figure 3.5 Stress relaxation results from forward Euler scheme

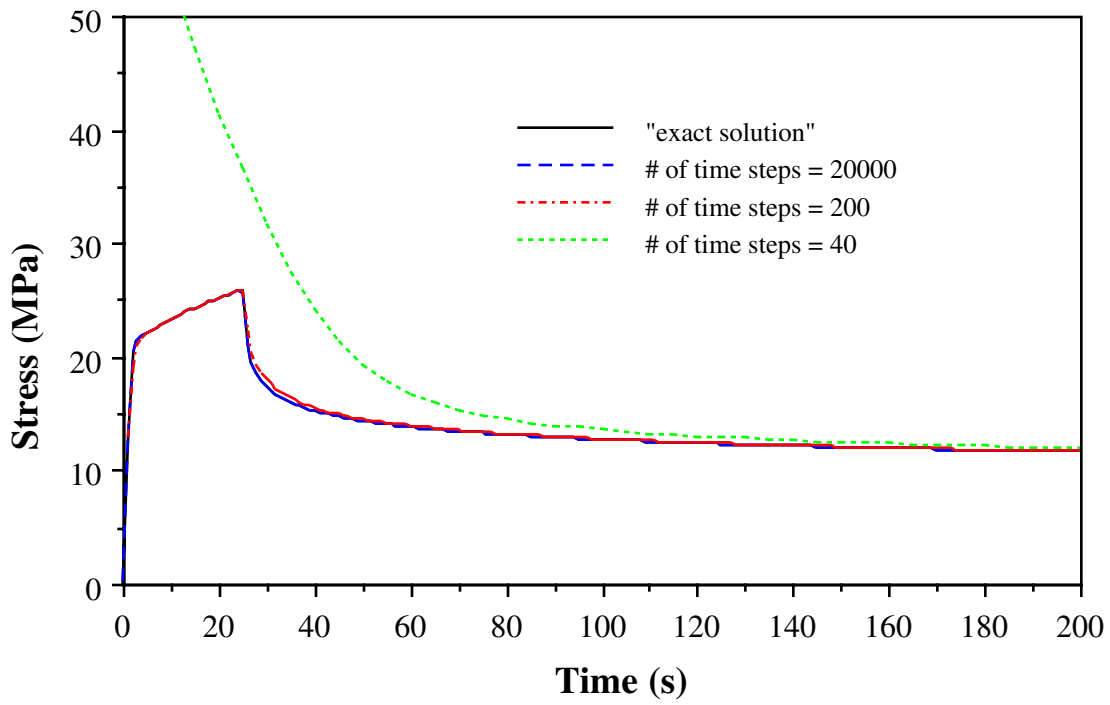


Figure 3.6 Stress relaxation results from forward gradient method

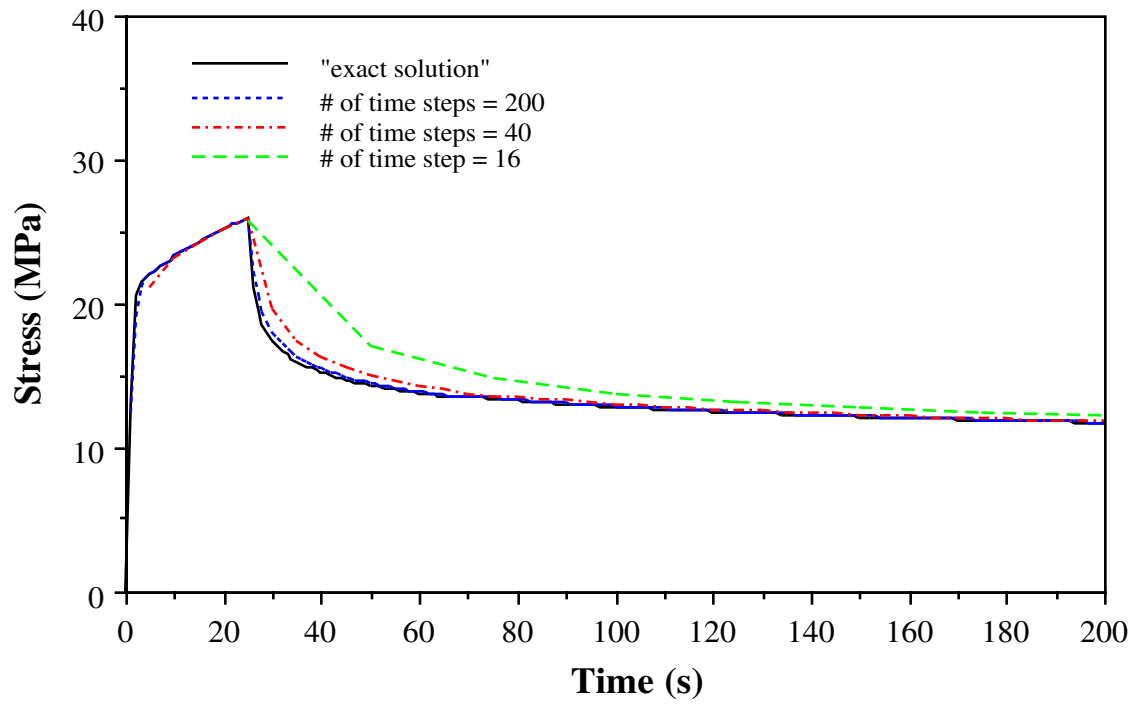


Figure 3.7 Stress relaxation results from backward Euler scheme with N-R iteration

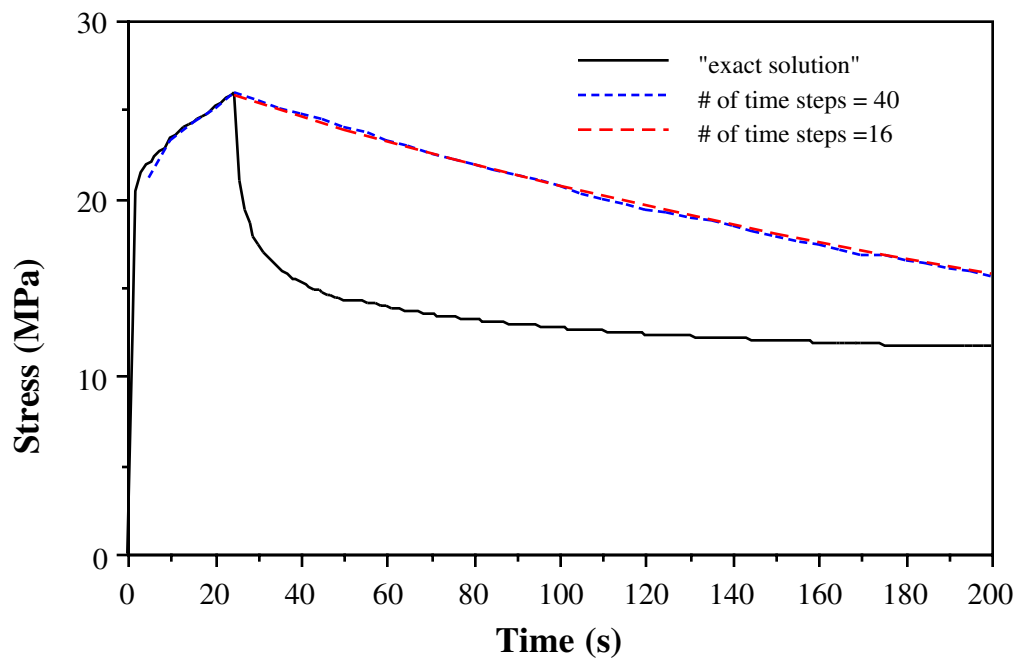


Figure 3.8 Stress relaxation results from backward Euler scheme with the Nemat-Nasser prediction method

3.6.3 Thermal stress analysis in a solidifying slab

Weiner and Boley developed an exact analytical solution of thermal stress during 1-D solidification of a slab with temperature-dependent, rate-independent, elastic-perfectly-plastic material behavior [53]. This problem has been transformed into a benchmark test problem which has gained extensive investigations with an elastic-viscoplastic constitutive equation [54]. Here, this test problem is employed to evaluate the proposed algorithms for the elastic-viscoplastic analysis. Detailed discussions for the treatment of liquid elements in the fixed-grid method, generalized plane strain implementation as well as the effect of time step and mesh size can be found elsewhere [54].

As shown in Figure 3.9, the problem involves one-dimensional solidification (x direction) in a semi-infinite domain. Initially, the domain contains liquid at a uniform temperature equal to the unique solidification temperature, T_s . At time $t = 0$, the surface ($x=0$) is suddenly chilled to T_f . The elastic-perfectly-plastic constitutive behavior includes a yield stress σ_Y , which decreases linearly from 20 MPa at T_f to zero at T_s as shown in Figure 3.10. Other thermal and mechanical properties are constants based on steel properties used by Kristiansson [55] : $\rho = 7400 \text{ kg/m}^3$, $c = 700 \text{ J/kgK}$, $K = 33 \text{ W/mK}$, latent heat $L = 272 \text{ kJ/kg}$, $T_s = 1468^\circ\text{C}$, $T_f = 1300^\circ\text{C}$, $\nu = 0.35$, $\alpha = 0.00002 \text{ K}^{-1}$, $E = 40 \text{ GPa}$.

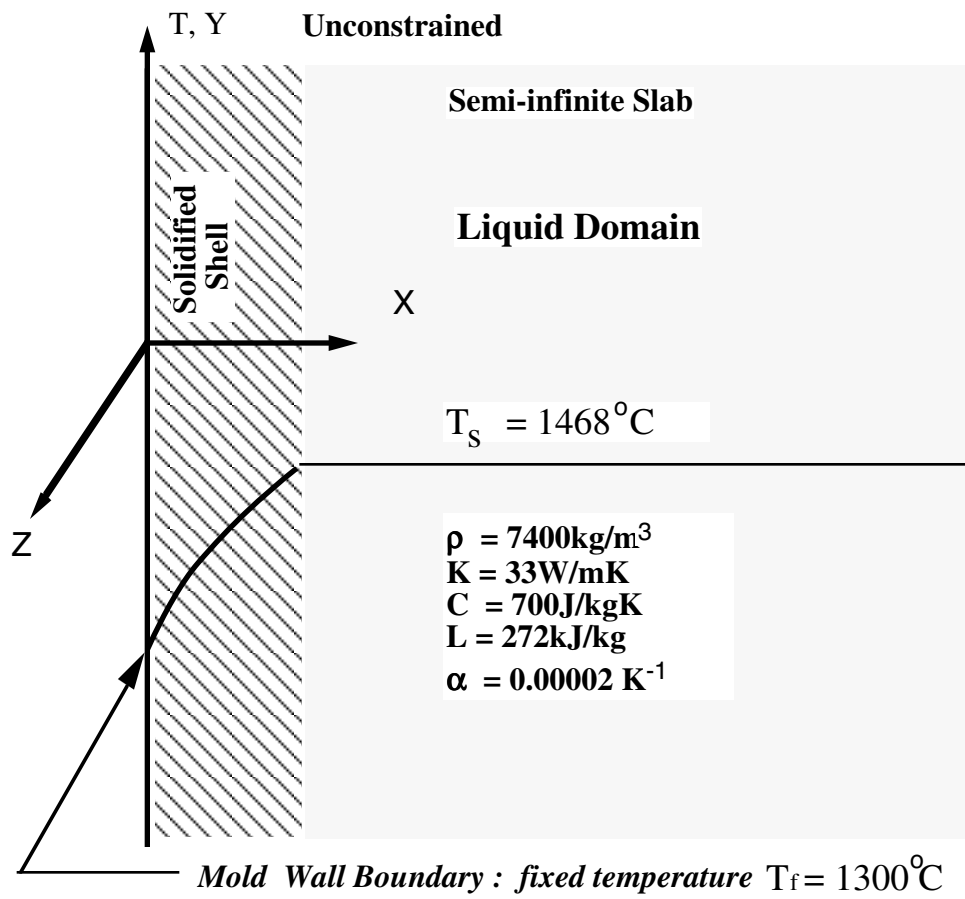


Figure 3.9 Chilled slab with one-dimensional solidification

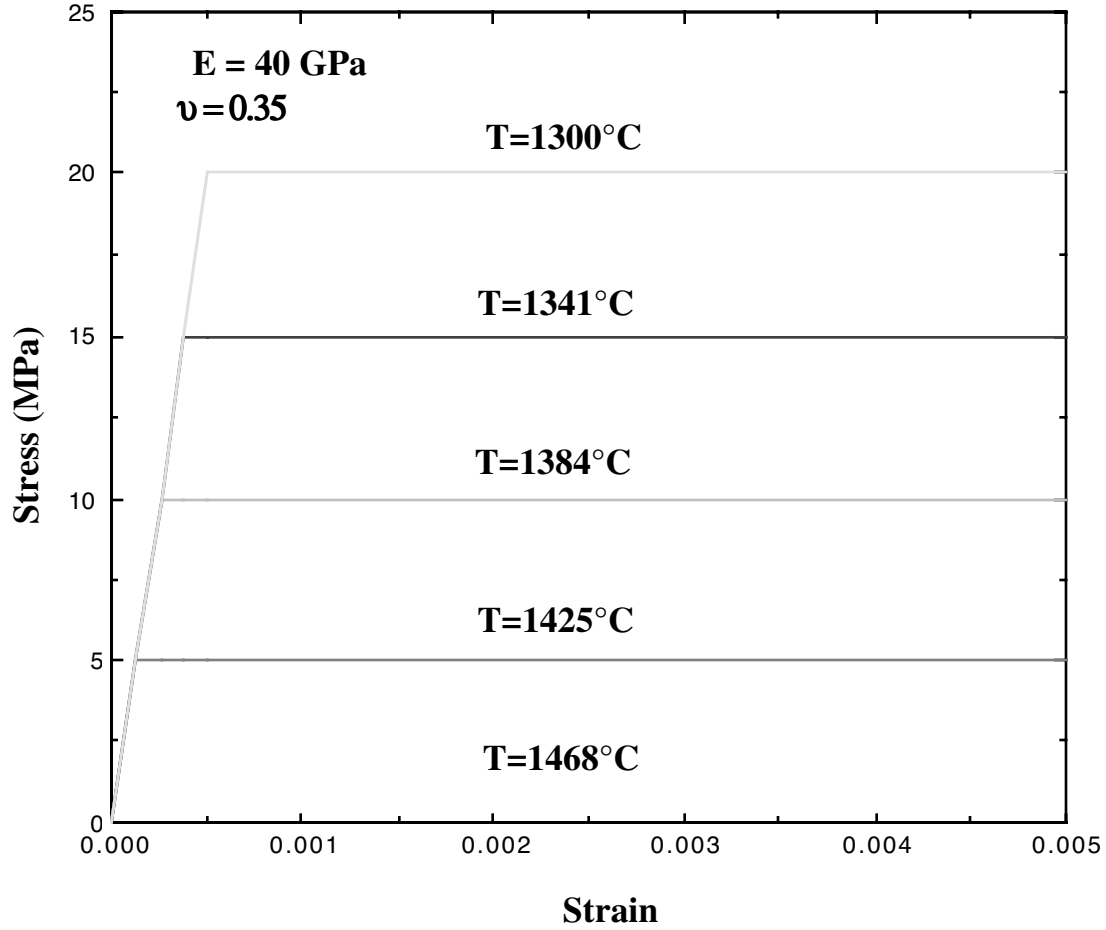


Figure 3.10 Constitutive behavior assumed in solidification test problem

The transient temperature distribution and the solidified shell thickness for this Stefan problem with a unique solution temperature can be found in Carslaw [56]. It is illustrated in Figure 3.11 at several different times. Stress across the solidified shell is given by Weiner and Boley [53] assuming generalized plane strain states in both y and z directions. The transverse stresses σ_y , σ_z are equal and vary with x while other components of stress are zero.

The numerical model was used to analyze the stress in this one-dimensional solidification test problem. The two-dimensional finite-element domain and mesh pictured in Figure 3.12 was adopted. Generalized plane strain conditions were assumed

in both y and z directions. The generalized plane strain state in the y direction was implemented by imposing the constraint that the vertical displacements are equal on the top side.

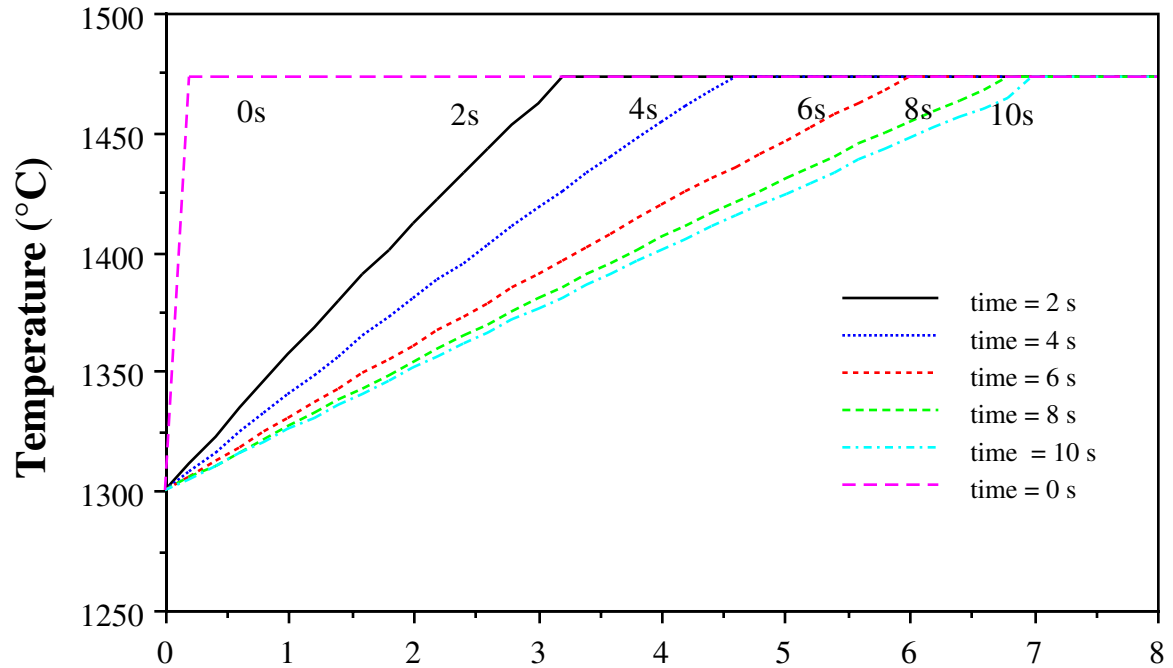


Figure 3.11 Temperature distribution in solidification test problem from analytical solution

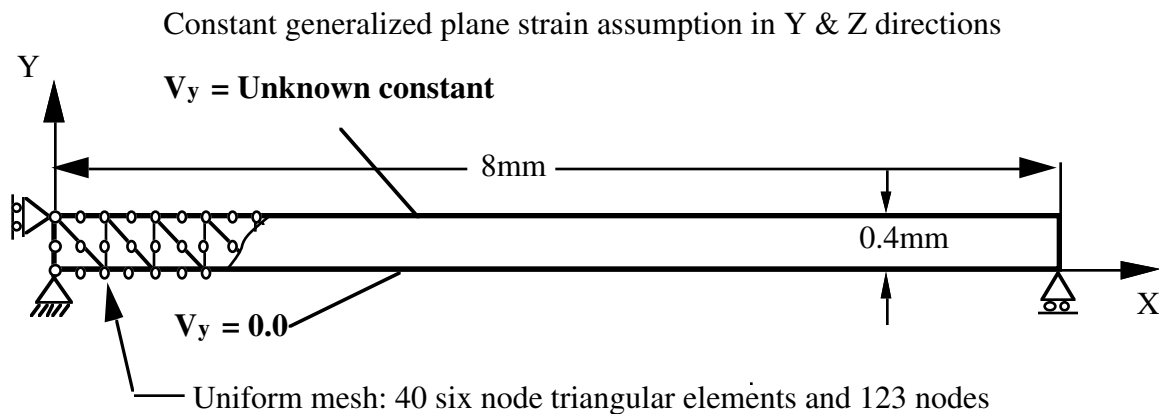


Figure 3.12 Finite element model of solidification test problem

To test the rate-dependent constitutive behavior, the elastic-perfectly-plastic constitutive model adopted in the present problem was transformed into an elastic-viscoplastic model using the nonlinear penalty function rate equation for the inelastic strain rate as discussed on section 3.6.1. This is a particularly rigorous test of the numerical algorithms due to the severe challenge required to model a time-independent constitutive equation with a strong nonlinear elastic-viscoplastic function.

To compare the numerical solutions with the analytical result, the relative error in norm L_2 is defined as

$$L_2 = \left(\frac{\sum |\sigma_{zn} - \sigma_{za}|^2}{\sum |\sigma_{za}|^2} \right)^{1/2}, \quad (3.78)$$

in which Σ from 1 to total nodes number of the simulation domain, σ_{zn} represents z stress from the numerical model, σ_{za} is z stress from the analytical solution.

Five different combinations of the time-integration schemes and constitutive algorithms including the explicit forward Euler scheme, the implicit backward Euler scheme with the bounded Newton-Raphson method (Implicit-BNR), the implicit backward Euler scheme with the Nemat-Nasser's prediction method (Implicit-NPM), the scheme alternating implicit-explicit with the bounded Newton-Raphson method (AIE-BNR) and the alternating implicit-explicit scheme with the Nemat-Nasser's prediction method (AIE-NPM) are employed to analyze the test problem. The 8 x 0.4 mm domain was modeled for 10s using 40 six-node generalized plane strain elements and time step size of 0.1s. This combined time step size and mesh size was found to be an optimum combination for controlling the relative error L_2 within 4% [54]. The σ_z stress distributions of different algorithms from the numerical model at $t = 10s$ are compared to the analytical solution in Figure 3.13. The relative errors and CPU times on IRIS 4D/25 of different algorithms are summarized in Table 3.1. For this special penalty-type

constitutive model, the explicit forward Euler scheme completely failed to get the correct solution since it suffered from stability problems even for very small time size (0.0001s) while the results of other four algorithms are in excellent agreement with the analytical solution without any stability problem for this relatively large 0.1s time step size. For both types of constitutive algorithms, the simulation process of the alternative implicit-explicit scheme is 6-7 times faster than the implicit backward Euler scheme. Compared with the CPU times of the implicit backward Euler scheme with different constitutive algorithms, the constitutive level iterations took approximate 12% percent of the total CPU time. Although the CPU time of the alternating implicit-explicit scheme with the Nemat-Nasser's prediction method is slightly less than that of the alternative implicit-explicit scheme with the bounded Newton-Raphson method, the alternating implicit-explicit scheme with the bounded Newton-Raphson method is still selected to analyze complex thermal-mechanical behavior with the unified constitutive models due to its better reliability.

More realistic constitutive behavior was simulated for solidifying plain-carbon steel using the rate-dependent elastic-viscoplastic model III of Kozlowski [4] instead of the penalty-type constitutive model while all of other simulation conditions were kept same as before. It is found that the explicit forward Euler scheme worked for this constitutive model with the limited time step size 0.005s with CPU time 412s without numerical overflow while the CPU time of the alternating implicit-explicit scheme with the bounded Newton-Raphson method is just 27 seconds. The Z stress results of this realistic constitutive model are shown in Figure 3.14.

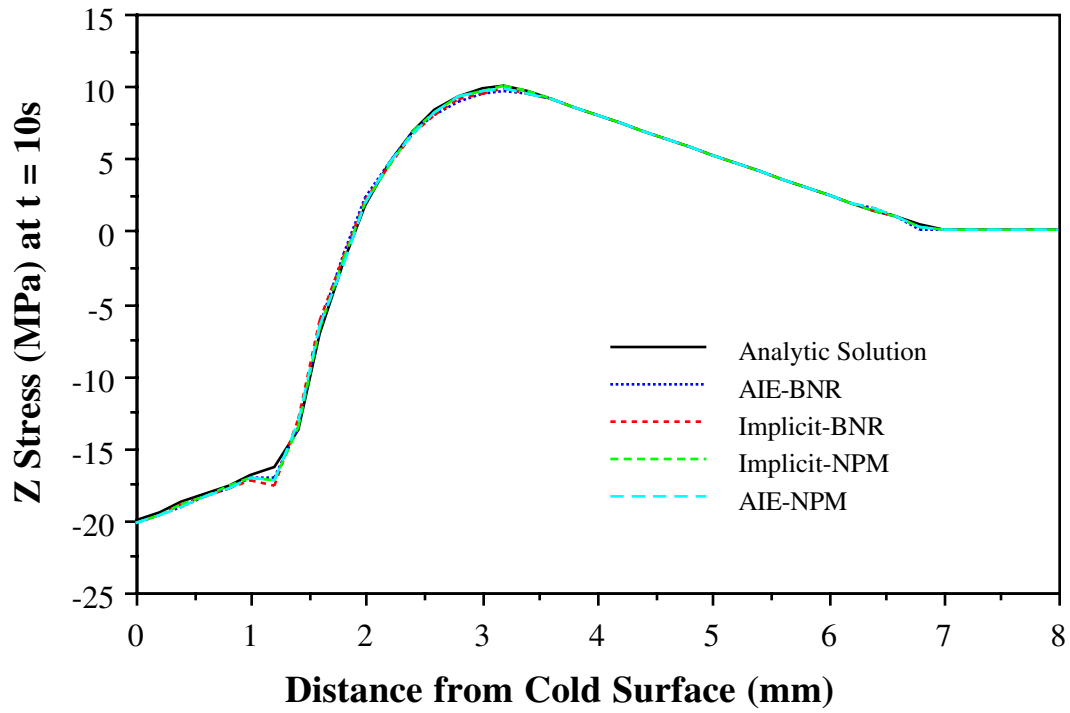


Figure 3.13 Comparison of analytic solution and FEM solutions for solidification with different algorithms

Table 3.1. Comparison of Accuracy and Cost of Different Elastic-viscoplastic FEM Algorithms

Method	Relative Error	CPU time (s)
	L_2 (%)	on IRIS4D/25
AIE-BNR	3.7	22
AIE-NPM	3.3	21
Implicit-BNR	4.1	143
Implicit-NPM	3.1	128
Explicit	numerical overflow	>20000

* the explicit scheme has numerical overflow even for 0.0001s time step size

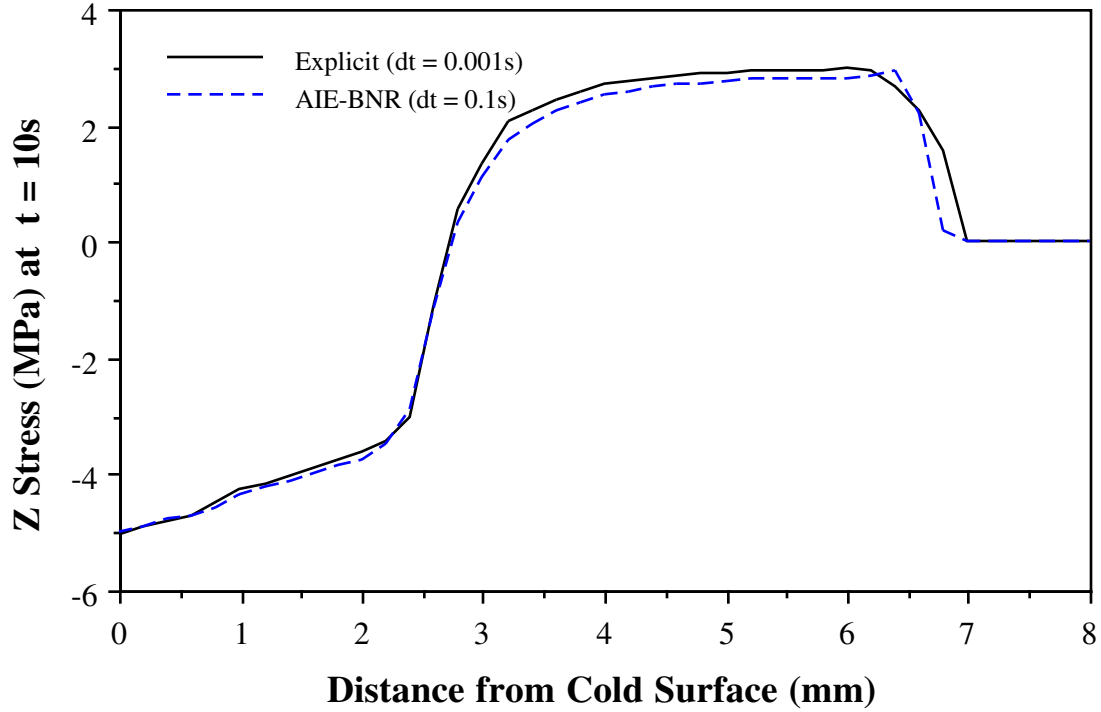


Figure 3.14 Comparison FEM solutions with realistic constitutive equation

3.7 Conclusion

Several robust and efficient numerical techniques have been implemented into a finite element calculation of unified, isotropic, temperature-dependent hyperelastic-viscoplastic models. Three numerical time-integration schemes are employed to integrate the constitutive models, including the explicit forward Euler scheme, the implicit backward Euler scheme and the alternating implicit-explicit scheme based on the operator-splitting technique. Various constitutive algorithms corresponding the successive substitution method, the forward gradient method, the Newton-Raphson method, the bounded Newton method and the Nemat-Nasser's explicit prediction method are examined after transforming the tensor algorithm constitutive models of the isotropic materials into problems with two scalar unknowns of the stress magnitude and the inelastic strain

magnitude. Based on some numerical experiments for the specified constitutive models for the high temperature plain-carbon steel, the following conclusion can be stated:

1. The alternating implicit-explicit scheme is stable and efficient compared with the forward Euler scheme and the backward Euler scheme. The implicit backward Euler scheme with proper constitutive algorithms takes 7 times more CPU time than this scheme while the explicit forward Euler scheme suffered stability problems.

2. The implicit backward Euler scheme with the successive substitution method and non-iterative forward gradient method was equal or slightly worse than the explicit forward Euler scheme. The successive substitution method has a convergence problem while the forward gradient method lost accuracy with large time step size.

3. Although both Newton-Raphson's methods performed very well, the bounded Newton-Raphson method is slightly more efficient.

4. The Nemat-Nasser's prediction method worked very well for some problems and failed with others.

5. The alternating implicit-explicit scheme with the bounded Newton-Raphson iteration is most robust, accurate and efficient combination of methods investigated. Thus, it has been chosen for future thermomechanical analysis of the solidification problem.

3.7 Reference

1. E.W. Hart, A phenomenological theory for plastic deformation of polycrystalline metals, *Acta Met.*, vol. 18 (1970) 599-610.
2. A.K. Miller, *Unified Constitutive Equations for Creep and Plasticity*, (Elsevier Applied Science Publishers Ltd, Essex, United Kingdom, 1987).
3. L. Anand, Constitutive Equations for the Rate-Dependent Deformation of Metals at Elevated Temperatures, *ASME Journal of Engineering Materials and Technology*, vol. 104 (1982) 12-17.
4. P. Kozlowski, B.G. Thomas, J. Azzi and H. Wang, Simple Constitutive Equations for Steel at High Temperature, *Metallurgical Transactions A*, vol. 23 (March) (1992) 903-918.

5. R.D. Krieg, Numerical Integration of Some New Unified Plasticity-Creep Formulations, Proceeding of 4th International Conference on Structural Mechanics in Reactor Technology, (1977) M6/4.
6. C.F. Shih, H.G. Delorenzi and M.A. K., A Stable Computational Scheme for Stiff Time-Dependent Constitutive Equations, Proceedings of the 4th International Conference on Structural Mechanics in Reactor Technology, (1977) L2/2.
7. T.J.R. Hughes, Numerical Implementation of Constitutive Models: Rate-Independent Deviatoric Plasticity. Theoretical Foundation for Large-Scale Computations of Nonlinear Material Behavior. (1984) 29-57.
8. N. Zabaras and A.B.F.M. Arif, A Family of Integration Algorithms for Constitutive Equations in Finite Deformations Elasto-viscoplasticity, International Journal for Numerical Methods in Engineering, vol. 33 (1992) 59-84.
9. T.Y.P. Chang, J.Y. Chen and S.C. Chu, Viscoplastic Finite Element Analysis by Automatic Subincrementing Technique, ASCE Journal of Engineering Mechanics, vol. 114 (1) (1988) 80-96.
10. T.G. Tanaka and A.K. Miller, Development of a Method for Integrating Time Dependent Constitutive Equations with Large or Neglect Strain Rate Sensitivity, International Journal for Numerical Methods in Engineering, vol. 26 (1988) 2457-2485.
11. K. Hornberger and H. Stamm, An Implicit Integration with a Projection Method for Viscoplastic Constitutive Equations, International Journal for Numerical Methods in Engineering, vol. 28 (1989) 2397-2421.
12. D. Cordts and F.G. Kollmann, An Implicit Time Integration Scheme for Inelastic Constitutive Equations with Internal State Variables, International Journal for Numerical Methods in Engineering, vol. 23 (1986) 533-554.
13. P. Poiss, P. Bussy and P. Ladeveze, A new approach in non-linear mechanics: the large time increment method, International Journal for Numerical Methods in Engineering, vol. 29 (1990) 647-663.
14. J.Y. Cognard and P. Ladeveze, A large time increment approach for cyclic viscoplasticity, International Journal of Plasticity, vol. 9 (1993) 141-157.
15. R. Glowinski and P.L. Talle, Augmented Lagrangian and Operator-Splitting Methods in Non-linear Mechanics, Vol. 9, Studies in Applied Mathematics, (SIAM, Philadelphia, PA, 1989).
16. O.C. Zienkiewicz and I.C. Corneau, Viscoplasticity -Plasticity and Creep in Elastic Solids - A Unified Numerical Solution Approach, International Journal for Numerical Methods in Engineering, vol. 8 (1974) 821-845.
17. K.J. William, Numerical Solution of Inelastic Rate Problems, Computers and Structures, vol. 8 (1978) 511-531.
18. V. Kumer, M. Morjaria and S. Mukherjee, Numerical Integration of Some Stiff Constitutive Models of Inelastic Deformation, ASME Journal of Engineering Materials and Technology, vol. 102 (1980) 92-96.

19. D. Stolle, An Interpretation of Initial Stress and Strain Methods, and Numerical Stability, *International Journal for Numerical and Analytical Methods in Geomechanics*, vol. 15 (1991) 399-416.
20. W.E. Haisler and P.K. Imbrie, Numerical Considerations in the Development and Implementation of Constitutive Models, *Nonlinear Constitutive Relations for High Temperature Application-1984*, NASA Conference Publication (1984) 169-185.
21. I. Cormeau, Numerical Stability in Quasi-Static Elasto/Visco-plasticity, *International Journal for Numerical Methods in Engineering*, vol. 9 (1975) 109-127.
22. T.J.R. Hughes and R.L. Taylor, Unconditionally Stable Algorithm for Quasi-Static Elasto/Visco-Plastic Finite Element Analysis, *Computers and Structures*, vol. 8 (1978) 169-181.
23. M.D. Snyder and K.J. Bathe, A Solution Procedure for Thermo-Elastic-Plastic and Creep Problems, *Nuclear Engineering and Design*, vol. 64 (1981) 49-80.
24. A.M. Lush, S.B. Brown and L. Anand, An Implicit Time-Integration Procedure for a Set of Internal Variable Constitutive Equations for Isotropic Elasto-Viscoplasticity, *International Journal of Plasticity*, vol. 5 (1989) 521-549.
25. S. Tjøtta, On the Numerical Integration of Internal State Variable Constitutive Models at Large Strains, *International Journal for Numerical Methods in Engineering*, (1994) in press.
26. J.C. Simo and S. Govindee, Non-linear B-stability and Symmetry preserving return mapping algorithms for plasticity and viscoplasticity, *International Journal for Numerical Methods in Engineering*, vol. 31 (1991) 151-176.
27. M. Kleiber, Computational coupled non-associate thermo-plasticity, *Computer Methods in Applied Mechanics and Engineering*, vol. 90 (1991) 943-967.
28. L.M. Taylor and E.B. Becker, Some Computational Aspects of Large Deformation Rate-Dependent Plasticity Problems, *Computer Methods in Applied Mechanics and Engineering*, vol. 41 (1983) 251-277.
29. M.L. Wilkins, Calculation of Elastic-Plastic Flow, in *Methods in Computational Physics*, Vol. 3, A.e. al., eds., Academic Press, New York, (1964)
30. R.D. Krieg and D.B. Krieg, Accuracies of Numerical Solution Methods for Elastic Perfectly Plastic Model, *ASME Journal Pressure Vessel Technology*, vol. 99 (1977) 510-515.
31. T.J.R. Hughes, Unconditionally Stable Algorithms for Nonlinear Heat Conduction, *Computer Methods in Applied Mechanics and Engineering*, vol. 10 (1977) 135-139.
32. D.R.J. Owen and E. Hinton, *Finite Element in Plasticity: Theory and Practice*, (pineridge Press Ltd., Swansea,UK, 1980).
33. D. Peirce, C.F. Shih and A. Needleman, A Tangent Modulus Method for Rate Dependent Solids, *Computers and Structures*, vol. 18 (1984) 875-887.

34. L. Anand, A. Lush, M.F. Briceno and D.M. Parks, A time-integration procedure for a set of internal variable type elasto-viscoplastic constitutive equations, Department of Mechanical Engineering, MIT, Report, 1985.
35. M. Wenner, A Generalized Forward Gradient Procedure for Rate Sensitive Constitutive Equations, International Journal for Numerical Methods in Engineering, vol. 36 (1993) 985-995.
36. G.G. Chen and T.R. Hsu, A Mixed Explicit-implicit Algorithm for Creep Stress Analysis, Int. J. Num. Meth. Engng., vol. 26 (1988) 511-524.
37. J. Douglas and H.H. Rachford, On the Numerical Solution of the Heat Conduction problem in 2d and 3d Space Variable, Trans. Amer.Math.Soc., vol. 82 (1956) 421-439.
38. A. Chulya and K.P. Walker, A New Uniformly Valid Asymptotic Integration Algorithm for Elasto-Plastic Creep and Unified Viscoplastic Theories Including Continuum Damage, International Journal for Numerical Methods in Engineering, vol. 32 (1991) 385-418.
39. T.Y.P. Chang, A.F. Saleeb and I. Iskovitz, Finite Element Implementation of State Variable-based Viscoplasticity Models, Computers and Structures, vol. 46 (1) (1993) 33-45.
40. C.W. Heaps and L. Mansfield, An Improved Solution Procedure for Creep Problems, International Journal for Numerical Methods in Engineering., vol. 23 (1986) 525-532.
41. S. Nemat-Nasser and Y.F. Li, A New Explicit Algorithm for Finite-deformation Elastoplasticity And Elastoviscoplasticity: Performance Evaluation, Computers & Structures, vol. 44 (5) (1992) 937-963.
42. S. Nemat-Nasser and D.T. Chung, An explicit constitutive algorithm for large-strain, large-strain-rate elastic-viscoplasticity, Computer Methods in Applied Mechanics and Engineering, vol. 95 (1992) 205-219.
43. B. Moran, M. Ortiz and C.F. Shih, Formulation of Implicit Finite Element Methods for Multiplicative Finite Deformation Plasticity, International Journal for Numerical Methods in Engineering., vol. 29 (1990) 483-514.
44. K.P. Walker, A Uniformly Valid Asymptotic Integration Algorithm for Unified Viscoplastic Constitutive Models, in Advances in Inelastic Analysis, S.e.a. Nakazawa, eds., ASME-AMD- vol.88, PED-vol.28, N.Y., (1987) 13-27.
45. S.O. Fatunla, Numerical Methods for Initial Value Problems in Ordinary Differential Equations, (ACADEMIC PRESS, INC., 1988).
46. J.G. Slater and S. Nakazawa, A Method for Efficient Finite Element Analysis of Problems Containing Unified Constitutive Laws, in Advances in Inelastic Analysis, S.e.a. Nakazawa, eds., ASME-AMD- vol.88, PED-vol.28, N.Y., (1987) 57-73.
47. O.C. Zienkiewicz, The Finite Element Method, (McGraw-Hall, New-York,Toronto,London, 1977).

48. J.C. Simo and R.L. Taylor, Consistent Tangent Operators for Rate-Independent Elastoplasticity, *Computer Methods in Applied Mechanics and Engineering*, vol. 48 (1985) 101-118.
49. R.H. Dodds, Numerical Techniques for Plasticity Computations in Finite Element Analysis, *Computers and Structures*, vol. 26 (5) (1987) 767-779.
50. J.W. Wu, Consistent Tangent Moduli for a New Class of Viscoplasticity, *ASCE Journal of Engineering Mechanics*, vol. 116 (1990) 1764-1779.
51. P.J. Wray, Effect of Carbon Content on the Plastic Flow of Plain Carbon Steels at Elevated Temperatures, *Metallurgical Transactions A*, vol. 13 (1) (1982) 125-134.
52. T. Suzuki, K.H. Tacke, K. Wunnenberg and K. Schwerdtfeger, Creep Properties of Steel at Continuous Casting Temperatures, *Ironmaking and Steelmaking*, vol. 15 (2) (1988) 90-100.
53. J.H. Weiner and B.A. Boley, Elasto-plastic thermal stresses in a solidifying body, *Journal of Mechanics of Physics and Solids*, vol. 11 (1963) 145-154.
54. H. Zhu and B.G. Thomas, Evaluation of Finite Element Methods for Simulation of Stresses During Solidification, *University of Illinois, Report*, 1994.
55. J.O. Kristiansson, Thermal Stresses in Early Stages of Solidification of Steel, *Journal of Thermal Stresses*, vol. 5 (1982) 315-330.
56. H.S. Carslaw and J.C. Jaeger, *Conduction of Heat in Solids*, (Clarendon, Oxford, 1959).

Thermal Distortion of Solidifying Shell near Meniscus in Continuous Casting of Steel

A two-dimensional, transient, finite-element model has been developed to simulate temperature, shape, and stress development in the steel shell, during the initial stages of solidification in the mold. The model is applied to predict the distorted shape of a vertical section through the shell, during a sudden fluctuation in liquid level at the meniscus. The calculation includes the effects of temperature-dependent properties, thermal shrinkage, phase transformations, and creep, using an elastic-viscoplastic constitutive equation for low carbon steel. The model features a robust, efficient algorithm to integrate the highly temperature- and stress-dependent constitutive equation for the inelastic-creep strain rate. The results show that thermal stress causes the exposed portion of the thin shell to bend towards the liquid, when there is a severe, sudden drop in liquid level. In addition, the axial temperature gradient creates high transverse stresses. The subsequent rise in liquid level increases the bending. These results illustrate an important mechanism contributing to the formation of transverse surface depressions and short longitudinal surface cracks associated with severe liquid level fluctuations.

4.1 Introduction

Most of the surface defects in continuous casting are suspected to initiate during the early stages of solidification in the mold, especially near the meniscus pictured in Figure 4.1. These defects include deep oscillation marks, surface depressions, longitudinal and transverse surface cracks. Although a body of empirical knowledge and evidence exists, the exact mechanisms for many of these problems are still unclear.

Undoubtedly, there are several different causes of different types of surface depressions. Oscillation marks have been proposed to originate from pressure buildup in the lubricating flux channel between the shell tip and mold during the negative strip time [1].

Interaction between the initial shell and the solid flux rim [2] or negative taper of the mold wall in the meniscus region [3] has been proposed to further add to this mechanism. Alternatively, if the meniscus freezes, this leads to a “meniscus mark” depression, often beneath a subsurface “hook” [1], when the liquid steel level overflows the meniscus each oscillation cycle [4].

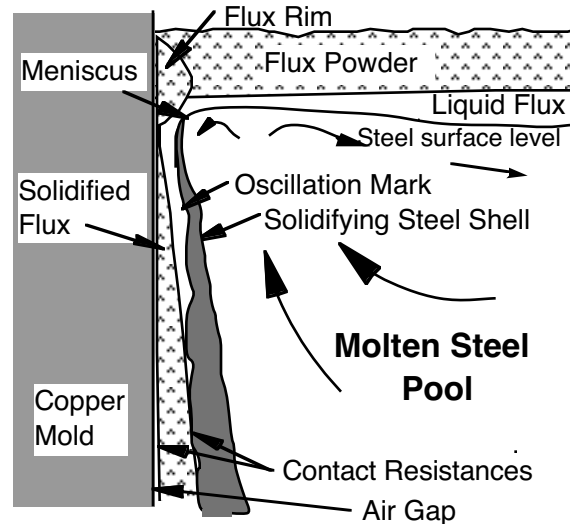


Figure 4.1 - Schematic of initial solidification near meniscus

Other depressions are not related directly to oscillation. A depression characterized by a double skin, with a carburized outer layer, has been reported by Kusano et al [5]. This defect was attributed to carbon pickup by the steel touching the powder flux layer directly and forming a lower melting point steel that ran over the meniscus during level fluctuations. Jenkins et al [6] have shown that another kind of depression may form during the peaks in large, slowly cycling mold level, possibly due to interaction of the newly solidifying shell with the slag rim. Depressions or “laps” in high carbon steel billets have been shown to originate near the meniscus [7]. They were attributed to boiling of the lubricating oil, bleeding through partial tears of the weak shell, and liquid level fluctuations [7]. A different type of surface depression may form longitudinally along the off-corner region of the slab wideface. These have been shown to originate due to inadequate shell growth in the affected region,

compression of the shell by excessive taper in the lower part of the mold, and bulging between rolls just below the mold [8].

Finally, large, random surface depressions, or “ripple marks”, have been observed which can extend to depths exceeding 1 mm, especially in steels with carbon content near 0.1% [4, 9]. These depressions have been attributed to thermal stresses due to the large shrinkage of the delta ferrite to austenite phase transformation of these steels. In addition, the peritectic phase transformation favors a high coherency temperature near the equilibrium solidus temperature, and a relatively strong shell [10]. Other grades, particularly steels with higher carbon contents, exhibit segregation, particularly of sulfur and phosphorus. This creates liquid films at the grain boundaries, which persist to much lower temperatures, leading to a coherency temperature far below the equilibrium solidus temperature and a relatively weak shell for a given amount of heat extraction [10]. The weaker shells presumably flatten due to ferrostatic pressure, so are less prone to depressions.

Many previous studies have correlated surface defects, including shallow surface depressions and longitudinal cracks, with fluctuations in the level of the liquid steel meniscus at the top surface of the mold. For example, a study of twin roll casting of stainless steel strip found that shallow surface depressions and longitudinal cracks were both suppressed by taking measures to minimize liquid level fluctuations [11].

Longitudinal surface cracks often exhibit similar symptoms and are attributed to similar causes as surface ripple depressions. They are both particularly severe in 0.1% C steels. They are also associated with large variations in mold temperature with time [12]. Longitudinal cracks have been found to depend on factors influencing mold flow conditions, such as the nozzle geometry and submergence depth [12, 13]. This is believed to be due to their increasing likelihood with higher amplitude surface waves [13].

To alleviate longitudinal cracking, it has been proposed that heat flux from the shell to the mold be reduced at the meniscus [14]. Wolf suggests that transverse depressions in 0.1 %C steels and certain stainless steels also are lessened by avoiding local overcooling

near the meniscus, which causes contraction due to a “plastic hinge effect” and rebending [15]. They can be reduced by lowering heat flux, via higher casting speed, higher superheat and an optimized mold flux. Specifically, depressions are found to lessen in 0.1% C steels when using a high melting point, low viscosity flux [16].

Clearly, the phenomena which occur during the initial stages of initial solidification in the mold of a continuous casting machine are extremely complex. Despite the body of empirical evidence pointing to the importance of initial shell deformation and mold level variations on surface depressions and cracks, very few previous attempts have been made to quantify and understand these phenomena using mathematical models.

One of the few previous studies used the MARC finite element program to predict the deformed shape of the initial shell during an oscillation cycle due to pressure variation in the flux channel [17]. The results agreed qualitatively with some observed trends of oscillation marks, but disagreed with others and differed by an order of magnitude with measured depression depths. No previous deformation model has studied the effect of mold level variations.

Finite-element models of heat transfer and stress have been developed to simulate the transient, two-dimensional temperature, shape, and stress distributions in the solidifying steel shell [18]. In this work, these models are applied to examine temperature and stress development during a brief, but severe fluctuation in liquid level at the meniscus. The results reveal a mechanism by which level fluctuations can lead to surface depressions and cracks.

4.2 Model Description.

A transient, thermal-elastic-viscoplastic finite-element model, CON2D [18], has been developed to follow the thermal and mechanical behavior of a section of the solidifying steel shell, as it moves down the mold at the casting speed. It is applied in this work to simulate behavior of a longitudinal slice down the centerline of the wide face shell near the meniscus.

4.2.1 Heat transfer model formulation

Using a Lagrangian frame of reference fixed on the strand moving at constant velocity (the casting speed) in the z-direction and considering that the deformation rate is small compared with the casting speed, the equation (2.1) governing heat transfer in the continuously-cast strand reduces to :

$$\frac{\partial}{\partial x} (k_x \frac{\partial T}{\partial x}) + \frac{\partial}{\partial z} (k_z \frac{\partial T}{\partial z}) = \rho C_p \frac{\partial T}{\partial t} . \quad (4.1)$$

The finite element domain is a thin longitudinal slice of steel along the mid wideface of the mold wall, containing the initially solidifying shell as shown in Figure 4.2. The heat flow in the transverse (y) direction is negligible along the wideface far from the corner. So a 2D model in the x-z plane is considered.

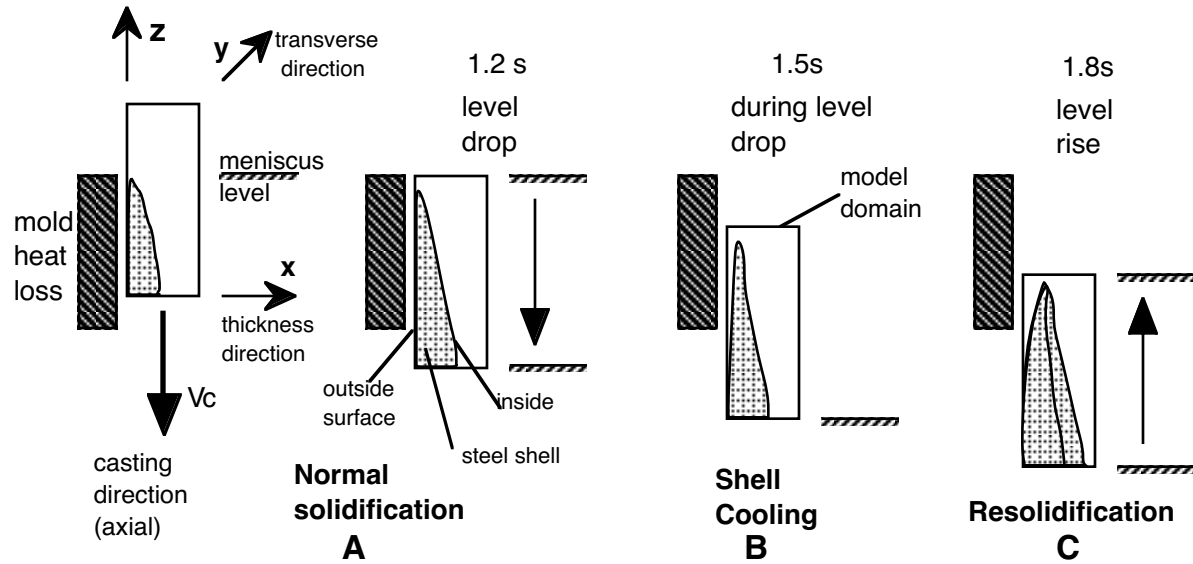


Figure 4.2 - Movement of longitudinal slice model domain during simulation

Applying the standard Galerkin finite element formulation [19] to Eq. (4.1) yields the following matrix equations:

$$[K]\{T\} + [C]\{\dot{T}\} = \{Q\} , \quad (4.2)$$

where $[K]$ is the conductance matrix , $[C]$ is the capacitance matrix including the effects of solidification, and $\{Q\}$ is the heat flow vector. Terms in these matrices were evaluated exactly using the standard consistent formulation [20] as detailed in Appendix A.

The latent heat of solidification is incorporated into Eq. (4.2) through an effective specific heat in $[C]$, which is evaluated using the spatial averaging technique suggested by Lemmon [21],

$$C_{p\text{eff}} = \frac{\partial H}{\partial T} = \frac{\| \text{grad } H \|}{\| \text{grad } T \|}, \quad (4.3)$$

where, $\| \cdot \|$ represents the norm. Here, $H(T)$ is the temperature-dependent enthalpy function for the steel alloy which includes the latent heat of solidification and is defined in terms of nodal values and element shape functions in the same manner as temperature.

This model employs the Dupont [22] three level time-stepping technique, which utilizes results of two previous time steps to approximate the temperature $\{T\}$ and the time derivative of temperature $\{\dot{T}\}$ as,

$$\{\dot{T}\} = \left\{ \frac{T^{t+\Delta t} - T^t}{\Delta t} \right\}, \quad (4.4)$$

$$\{T\} = \frac{1}{4} \{3T^{t+\Delta t} + T^{t-\Delta t}\}, \quad (4.5)$$

where $\{T^{t+\Delta t}\}$ are the unknown temperatures, for which the current equations are being solved, $\{T^t\}$ are the temperature at the last time step, and $\{T^{t-\Delta t}\}$ are the temperature at the time step before $\{T^t\}$. This scheme is an optimal compromise between stability and accuracy [20].

Applying this technique to Eq. (4.2) yields the recurrision formula,

$$\left[\frac{3}{4} [K] + \frac{[C]}{\Delta t} \right] \{T^{t+\Delta t}\} = \{Q\} - \frac{1}{4} [K] \{T^{t-\Delta t}\} + \frac{[C]}{\Delta t} \{T^t\}. \quad (4.6)$$

Eq. (4.6) is then solved at each time step for the unknown temperatures $\{T^{t+\Delta t}\}$ using the standard Choleski decomposition solution routine [23].

Since the fixed-grid method is employed here to simulate heat transfer, special treatment is needed to handle the liquid level drop / rising phenomena, which will discussed later.

4.2.2 Mechanical model formulation

The stress model solves for the stresses, strains, and displacements, by interpolating the previously-calculated thermal loads onto a fixed-grid finite-element mesh of 6-node triangles [18, 24, 25]. Detailed discussion about the governing equations, finite element formulation and solution procedure can be found in Chapter 2. The effects of volume changes due to temperature changes and phase transformation are incorporated through a temperature- dependent thermal-linear-expansion (TLE) function.

The out-of-plane (y-direction) stress is characterized by the state of generalized plane strain. This allows the 2-D model to reasonably estimate the complete 3-D stress state, for the wide, thin shell of interest. This is the best assumption in the absence of friction, because the longitudinal slice is constrained by the rest of the shell to remain planar as it moves down the mold.

Constitutive behavior for solidifying plain-carbon steel was simulated using the rate-dependent, elastic-viscoplastic model III of Kozlowski [26]. This model was developed to match tensile test measurements of Wray [27] and creep data of Suzuki [28] over a range of strain rates, temperatures, and carbon contents to simulate austenite under continuous casting conditions. The elastic modulus varied with temperature (800 °C to solidus) according to the following polynomial, based roughly on measured data from Mizukami et al [29]:

$$E \text{ (GPa)} = 674 - 1.53 T(^{\circ}\text{C}) + 0.0012 T(^{\circ}\text{C})^2 - 0.000000317 T(^{\circ}\text{C})^3. \quad (4.7)$$

These constitutive equations are integrated using a new two-level algorithm, which alternates between solutions at the local node point and the global system equations [30]. Elements containing liquid as defined by the specified coherency temperature, are set to have no elastic strain. Validation of this model using both analytical solutions and measurements from operating slab casters is described elsewhere [31].

4.2.3 Special treatment for liquid level dropping / rising

For the heat transfer analysis, a drop in liquid level is simulated by suddenly turning the liquid elements into " air elements" with zero latent heat. These air elements have very small conductivity, specific heat, density and enthalpy, which greatly lowers heat transfer rate. The temperature of liquid nodes is fixed to the ambient temperature during this cooling stage. The internal heat transfer boundary between the solidified shell and the air is turned on to cool down the solidified shell. Once the liquid level rises, the properties of the air elements are suddenly changed back to those liquid elements and their temperature is replaced by the pouring temperature.

The mechanical analysis requires no change, as the air elements are treated as the liquid element with zero elastic strain as discussed in chapter 2.

4.2.4 Thermo-mechanical property data

Accurate material property data is a key to the successful prediction of any model. Therefore careful selections were made for the property data used in these simulations. The majority of the data for plain-carbon steel was obtained from the work of Harste [32] and the data for stainless steel was obtained from Pehlke [33] .

4.2.4.1 Thermal conductivity

The temperature dependent thermal conductivity function used in the model is shown in Figure 4.3, which also shows the effect of carbon content on the thermal conductivity function.

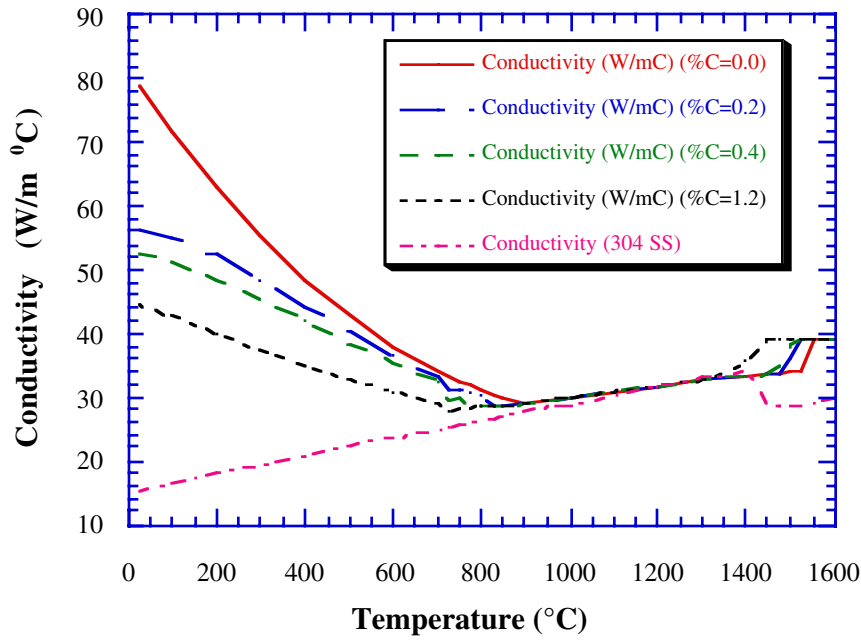


Figure 4.3 Thermal conductive of Carbon and Stainless steel as a function of temperature

4.2.4.2 Enthalpy

The enthalpy H , which represents the total heat content, is shown as function of temperature and carbon in Figure 4.4. The curve for stainless steel is also plotted in the same figure.

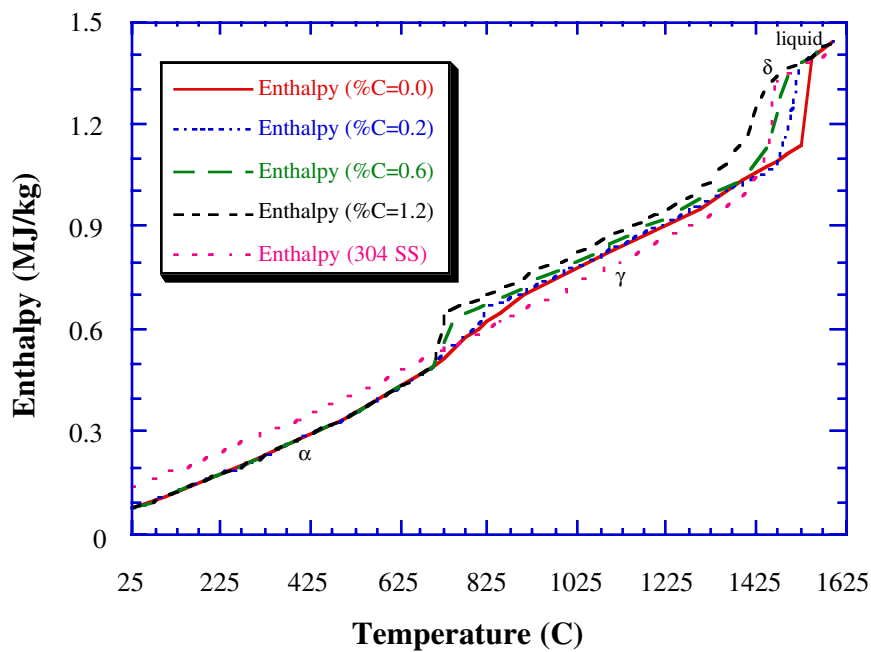


Figure 4.4 Enthalpy of carbon steel and stainless steel used in the model

4.2.4.3 Thermal linear expansion

The thermal linear expansion (TLE) function used in the model is shown in Figure 4.5 as a function of both temperature and carbon percentage for plain carbon steels. The TLE function for autenitic stainless steel (taken from [33]) used in the model is mainly based on the expansion of austenite and also shown in Figure 4.5. For carbon steel, the function, which is taken from [32], shows a sharp transition representing the δ - γ transformation.

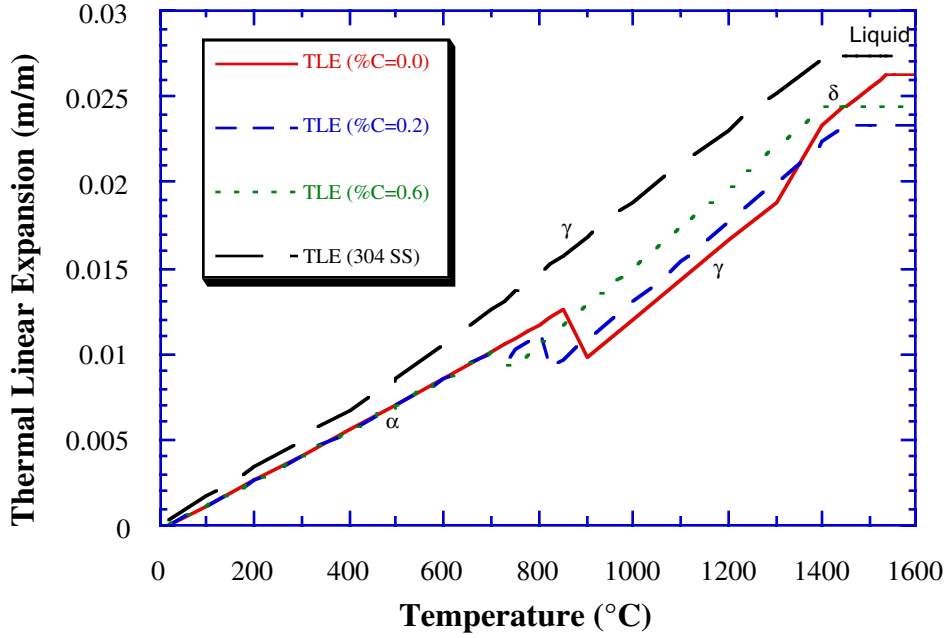


Figure 4.5 Thermal linear expansion curves for carbon and stainless steel

4.2.5 Boundary conditions

A Lagrangian formulation is adopted, so the model domain is initially assumed to contain stress-free liquid at uniform temperature, T_0 . The shell is assumed to form continuously below a sharp meniscus and move downward at the casting speed, as illustrated in Figure 4.2. Thus, the heat flow model imposes a zero heat flux condition on those portions of the mesh above the liquid level prior to the level drop.

$$q = 0, \quad \text{for } z > V_c t \text{ and } x = 0. \quad (4.8)$$

$$q = h_c (T - T_m), \quad \text{for } z < V_c t \text{ and } x = 0. \quad (4.9)$$

After the shell has moved downward 20 mm (1.2s), the liquid level is suddenly dropped for 0.6s. This roughly approximates the duration of an oscillation cycle or a random flow transient. During this time, liquid elements are ignored and the following boundary condition is imposed along the exposed solid shell, defined by the location of the solidus isotherm at the time of the level drop:

$$q = h_a (T - T_a), \quad \text{for } 1.2s < t < 1.8s. \quad (4.10)$$

Finally, the level is raised again at 1.8s, by restoring the liquid elements at the initial temperature, and allowing solidification to continue. Note that the level is restored only to the top of the shell tip, so that overflow of the meniscus is not simulated. Heat transfer coefficients and temperatures are given in Table 4.1. Zero heat flux is assumed across the top, bottom, and liquid-steel sides of the domain.

All external surface tractions were set equal to zero, except for fixing three nodal displacements at the domain bottom to prevent rigid body motion. This stress-free condition models shell behavior in the absence of mold friction, pressure in the flux channel, or ferrostatic pressure.

Table 4.1 Simulation Conditions

Material properties		Ultra-low carbon steel (ULC)
	Composition	0.003%C
	Liquidus Temperature	1535.76 °C
	Solidus Temperature	1534.63 °C
Casting Conditions		
T _o	Initial temperature	1537 °C
	Superheat	1.24 °C
V _c	Casting speed	16.7 mm/s (1 m/min)
T _m	Mold temperature	250 °C
h _c	Mold / shell heat transfer coefficient	2000 W/m ² K
	Mold friction	none
Level fluctuation conditions		
	duration	0.6 s
	Distance of level drop	30 mm
	Distance of subsequent level rise	20 mm
T _a	Ambient temperature	35 °C
h _a	Ambient heat transfer coefficient	272 W/m ² K
Simulation conditions		
	Domain size	3 x 20 mm
	Stress state	generalized plane strain

4.2.6 Discussion of model assumptions

This work considers a very severe drop in liquid level, (20-30 mm) in order to examine the maximum expected effect of thermal distortion of the solidifying shell caused by a level fluctuation. Level fluctuations of this size are possible in practice by rare circumstances which generate an abnormal surface wave, such as the entrapment and release of large argon bubble(s) in the nozzle, sudden release of a nozzle clog, sudden bulging (as a depression moves beneath a roll) below the mold or temporary loss of level control. These events are generally accompanied by severe surface defects, which this work aims to explain. Understanding how these severe defects are formed should also shed light on the formation of defects caused by lesser fluctuations, including oscillation marks.

Ultra-low carbon steel (0.003%C) was selected for this initial work for several reasons. First, this alloy is almost pure iron, so exhibits very little segregation. Thus, the mushy zone (between solidus and liquidus temperature) is very thin and the coherency temperature (at which the shell can bear a load) is assumed equal to the solidus temperature.

This simplifies development of the model considerably. Secondly, the high coherency temperature of this alloy is expected to make it behave in a similar manner to the defect-sensitive 0.1 %C peritectic steels. Finally, ultra-low carbon steel is commercially important in its own right.

The model neglects pressure forces which act on the shell. This includes ferrostatic pressure, which tends to flatten out the distorted shell when the level is high. The model also ignores pressure variations in the molten flux, which tend to enhance bending of the meniscus and shell towards the liquid, which is one of the causes of oscillation marks. These pressures are both on the order of 1 kPa. To include them properly requires a transient flow analysis of both the molten flux and the molten steel. Although these effects are important, they are not expected to completely overshadow thermal distortion of the shell, if it has a fully solid layer.

The model ignores the drop in heat transfer that should occur when the shell loses contact with the mold and bends towards the liquid. Including this coupled phenomenon would increase surface temperature and lead to even more bending toward the liquid than predicted here.

The model ignores the curvature of the meniscus and further assumes zero heat flow above the meniscus. It also ignores nonuniform dissipation of superheat due to flow in the liquid pool. This means that meniscus solidification cannot be modeled. Including this effect would presumably allow prediction of the shape of subsurface hooks and oscillation marks.

Relatively slow heat transfer is assumed, representing conditions for an optimal mold powder for depression-sensitive grades, with good coverage and lubrication in the meniscus region. Thus, defects caused by nonuniform heat flow are not simulated. Nucleation undercooling effects are also ignored.

The model neglects mold friction. Sticking of the shell to the mold naturally would generate tensile stress, which may contribute to cracks. For example, sticking of the shell to the mold on either side of a longitudinal depression would concentrate strain at the hottest,

weakest portion of the shell. This is another likely mechanism contributing to longitudinal cracks.

Slag entrainment during the level drop was ignored. In addition to creating subsurface inclusion defects, this would slow down resolidification after the level rises. The results presented here show very fast resolidification due to the perfect contact assumed between the liquid and shell after the level rise.

The model ensures no elastic strain in the liquid, so thermal stress and distortion are generated only by thermal contraction in the solid state. Strain on the liquid is assumed to generate fluid flow, as necessary. For high coherency-temperature materials, such as considered in this work, this assumption is probably reasonable. In regions of high solid fraction in grades with dense columnar mushy zones, it might not be.

4.3 Results

Two simulations were performed. The first considers thermal stress development in a section of solidifying shell that is fully constrained from thermal distortion. Figure 4.6 shows the temperature profile across the shell at three important times before, during, and after the sudden 0.6s drop in liquid surface level. A portion of the shell 20 mm below the meniscus at the time of the level drop is considered. Figure 4.7 shows the corresponding axial (z) stress distributions through the shell. Calculated nodal values, shown as points in this figure, show oscillation due to the course mesh, so a smooth curve is drawn through each set. Because there is no external stress, such as mold friction, the stress profiles across the shell must average zero to maintain equilibrium, so the tensile and compression regions must balance. Finally, note that stress must decrease to zero at the solid / liquid interface, as defined by the coherency temperature (assumed to be the solidus). This is required because liquid always solidifies stress-free.

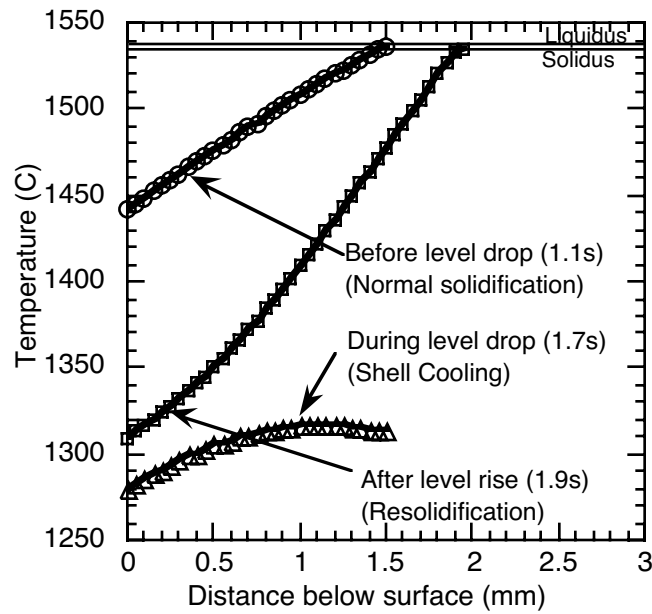


Figure 4.6 - Temperature profile through shell

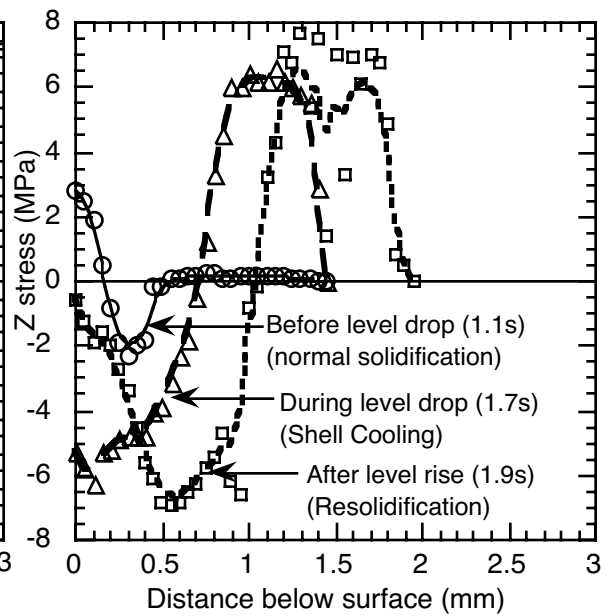


Figure 4.7 - Axial (z) stress profiles
through constrained shell

The second simulation allows completely free bending of the shell. Temperature contours within this shell are shown in Figure 4.8, superimposed on the distorted shape, which is magnified two times. The computed axial stresses are negligible, having been replaced by bending of the shell. Stresses through the thickness (x direction) are also negligible. However, Figure 4.9 shows the maximum transverse (y) stress distribution along the surface, with the corresponding temperature profile, which occurs at the end of the level drop. These results are discussed together in chronological order.

Figure 4.8 Distorted shell shape with temperature contours (°C) (magnified 2X)

A) Normal solidification

max. x. surface gap

-0.06 mm

1.1s

B) During mold level drop

max. x surface gap

+ 0.45 mm

1.7s

C) After level rise

max. x. surface gap

+ 1.65 mm

1.9s

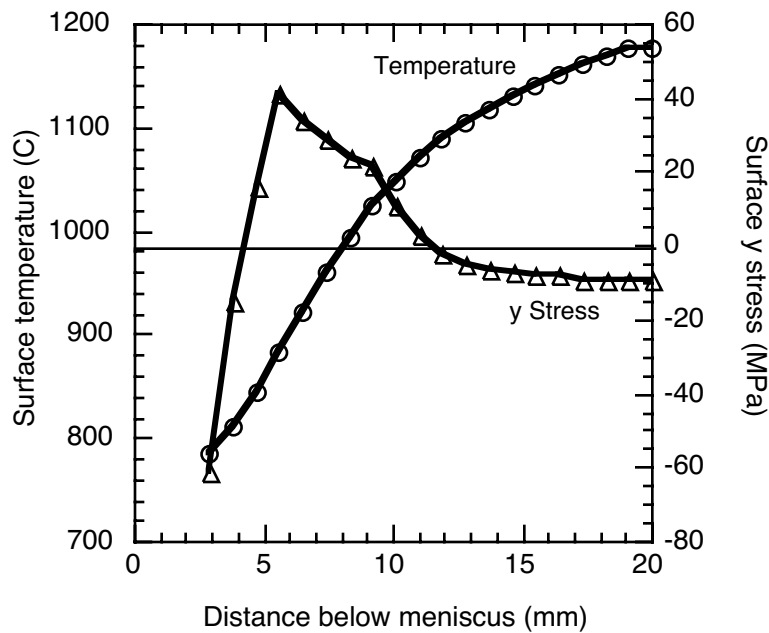


Figure 4.9 - Y stress and temperature down shell surface (1.8s)

A. During solidification

The nature of both the stress distribution and corresponding shape of the solidifying shell depends on the cooling history, as defined by the heat transfer coefficient, h_c , on the boundary of the shell facing the mold. Figures 4.6 and 4.8a) show the temperature distribution during the initial stages of uniform solidification near the meniscus. Relatively high temperature gradients exist through the shell thickness, as the shell surface is cooling rapidly.

When the cooling rate is high after initial solidification, a significant temperature gradient is also created in the casting direction (z). Thus, the shell surface cools and contracts rapidly. When constrained, this generates a slight z -tensile stress within the surface layer of the shell, balanced by slight compression beneath it. Stresses during solidification are low, on the order of only 2 MPa, due to the rapid creep relaxation and low elastic modulus at these high temperatures. The predicted stress levels are consistent with flow stress measurements of 1 - 5 MPa, made on solidifying shells by Hiebler et al [34].

When unconstrained, these z-stresses cause the shell to bend slightly in a concave shape toward the mold walls. This is illustrated in Figure 4.8a). The depth of the depression is very small however, being less than 0.1 mm over the 20 mm length of shell simulated. The remaining z-stresses are still tensile at the surface and compressive in the subsurface. However, their magnitude is almost negligible, due to the rapid stress relaxation at these high temperatures.

These results contrast with conditions later during solidification, when the surface cooling rate is slow. In this case, reported elsewhere [30], the surface temperature becomes relatively uniform. Then subsurface cooling and contraction generates subsurface tension, which induces compression at the surface of the shell. This tends to reverse the slight bending of the shell from the mold, presenting a slightly convex shape toward the mold walls instead.

B. During drop in level

Figure 4.6 shows that temperature throughout the shell tip decreases rapidly during the short 0.6s level drop, falling about 200 °C even 20 mm below the meniscus. Without the heat supplied from the molten metal, the mold is able to extract sensible heat from the thin shell very quickly, even with the relatively small heat transfer coefficient assumed in this work.

Temperature gradients across the shell thickness disappear also, as temperature within the thin shell equilibrates. This means that the shell inside cools more than the outside. This is naturally accompanied by a greater contraction of the inside of the shell, relative to the outside surface. When constrained, this generates large subsurface tensile stresses, (6 MPa) seen in Figure 4.7. Corresponding compression stresses are generated at the surface.

When unconstrained, this internal contraction causes the shell to bend significantly toward the liquid, leaving a convex shape facing the mold. This contraction is calculated to reach 0.45 mm over the 20 mm length of shell modeled, as shown in Figure 4.8b). This

prediction appears roughly consistent with the measured shape of 5 mm high, ultra-low carbon and peritectic steel droplets quenched on a copper chill [35]. These researchers observed bending which produced a concave shape toward the mold and gaps of 0.2 mm over a length of 8 mm.

Equally important to the large distortion of the shell toward the liquid are the stresses generated. Stress levels in the shell thickness (x) and casting directions (z) remain very low. However, Figure 4.9 shows that the calculated y-stress along the shell surface reaches a maximum of over 40 MPa at the end of the level drop. This is caused by the large axial temperature gradient combined with constraint by the rest of the wide face shell. Naturally, the average stress is zero, due to the assumption of no friction. The shell tip is compressive due to the δ to γ volume expansion. However, just below the tip, thermal contraction is relatively large. This creates high tensile stress across the entire shell over an axial distance of 6mm for this 20mm level drop.

These high tensile stresses are consistent with viscoplastic deformation at these low temperatures. However, in crack-sensitive peritectic grades, this might be sufficient to generate longitudinal surface cracks.

C. After rise in level

Figures 4.6 and 4.8c) show the rapid increase in temperature, shell thickness, and distortion which is predicted to occur after the liquid level is suddenly raised back up to the tip of the shell. Reestablishing contact with the liquid causes solidification to continue, generating a “newly solidified” shell on top of the existing solid shell. The initial rate of the new solidification is rapid because perfect contact is assumed between the liquid steel and the existing shell. This new solidification quickly heats the inside of the existing shell, restoring the high temperature gradient through the shell typical of normal solidification (Figure 4.8a).

The increased average temperature of the older solidified layer causes it to expand. However, the newly solidified layer restrains this expansion, if it is of sufficient strength, which is the case for the ultra-low steel layer studied here. Moreover, this newly solidified

layer itself is cooling and contracting. Unlike initial solidification against the mold, this new layer is attached to the older shell layer, so is unable to contract free of stress and distortion during its initial cooling stages. The result is further bending of the shell towards the liquid. The increase in tip distortion is significant, reaching 1.65 mm, as illustrated in Figure 4.8c).

4.4 Mechanism of surface depressions and longitudinal cracks

The results presented in the previous section illustrate a detailed mechanism to form shallow surface depressions and short longitudinal cracks due to a sudden level fluctuation. First, a severe drop in liquid level at the meniscus causes bending of the shell away from the mold toward the liquid. The subsequent rise in liquid level increases this bending. Finally, overflowing of the shell tip after the level rise begins creation of a new shell closer to the mold wall. This leaves behind a surface depression to travel down the mold.

Deeper and longer level drops obviously should create deeper depressions. The location of the depressions should naturally concentrate at locations on the strand perimeter where level fluctuations are frequent. Due to the random nature of level fluctuations, these depressions should occur randomly, with irregular but generally transverse shapes. They may also have oxides beneath the outer layer of steel, if the level drop entraps liquid mold flux.

A severe level drop also causes rapid cooling of the shell tip and high transverse stresses. These stresses could generate longitudinal cracks along the shell tip, if the steel grade is susceptible. These cracks are predicted to be shallow, longitudinal surface cracks, less than 1 mm deep and 5-10 mm long, depending on the extent of the level fluctuation.

4.5 Discussion

This work shows how meniscus level fluctuations can directly initiate a particular type of transverse surface depression and / or short, shallow longitudinal surface cracks, by generating thermal distortion and stress in the initial shell. This mechanism complements

other mechanisms involving indirect effects of mold level changes on defects, such as disrupting the uniform feeding of lubricating flux into the mold / shell gap.

These defects initiated by level changes can be aggravated later by other mechanisms. For example, as each transverse depression moves down the mold, it causes a local reduction in the heat transfer rate beneath it, especially if there was a lubrication problem leading to a local air gap. This produces a drop in mold temperature which is delayed by the casting speed and distance below the meniscus. This is consistent with the strong statistical correlation between mold level fluctuations and mold temperature fluctuations that has been observed experimentally [36]. Furthermore, solidification at the reduced cooling rate should produce a courser dendrite arm spacing beneath each depression. The hotter shell beneath each depression is weaker, so any additional tensile stress, such as generated by mold friction due to a lack of lubrication, would be expected to concentrate at the existing longitudinal surface crack, propagating it longer and deeper, possibly connecting with subsurface cracks [37]. The tensile stress also encourages macrosegregation of interdendritic liquid toward the surface, further weakening the shell and enabling crack growth.

The bending mechanism shown in this work is expected to produce the deepest depressions in solidifying shell tips that have the highest solid-state contraction and the highest coherency temperature relative to the surface temperature. This may explain the observed effect of steel grade on ripple mark depression susceptibility. The mechanism has been modeled here only for ultra-low carbon steel. Solidifying shell tips of this pure metal have a high coherency temperature, owing to their narrow mushy zone and lack of segregation.

It is suspected that steels near 0.1% C should also be prone to the proposed bending mechanism, for reasons explained by Wolf [10]. First, these peritectic steels experience the most solid state thermal and phase transformation contraction. Second, peritectic steels also exhibit a high coherency temperature, only slightly below the equilibrium solidus

temperature. Finally, these steels also experience interdendritic weakness, making them more prone to cracks than the ultra-low carbon steel.

Steels with a wide mushy zone and segregation, such as high carbon steels, are likely not susceptible to this depression mechanism. This is because these steels retain a liquid fraction at the surface for distances down the mold far greater than the maximum likely liquid level fluctuation. With the complete shell above the coherency temperature, bending strain cannot develop.

The bending mechanism shown here might contribute to the formation of deep oscillation marks. At any time during the oscillation cycle, if the surface level dropped to expose the shell tip, then the predicted bending of the shell away from the mold would amplify the depth of that oscillation mark. This might help to explain why peritectic steel grades tend, on average, to have deeper oscillation marks [16] than other steel grades. It also predicts that deep oscillation marks are more likely at positions around the mold perimeter where level fluctuations are most frequent.

The bending mechanism shown here is not expected to explain the shape of subsurface “hooks”, caused by meniscus freezing. These hooks have more curvature than the gradual depressions calculated in this work because they take their shape from the original curved liquid meniscus. Meniscus shape is controlled by surface tension balanced with gravity, dynamic forces in the liquid and pressure in the flux channel, which were not modeled in the present work.

The obvious practical implication of this work is that severe, sudden drops in meniscus level are detrimental to surface quality, even with an optimal flux practice, adequate lubrication, and otherwise uniform conditions. Thus, measures should be taken to control meniscus level in the mold to avoid these fluctuations. This involves careful choice of nozzle geometry, argon injection practice, and other casting conditions affecting liquid steel flow near the meniscus.

4.6 Conclusions

Two-dimensional, transient finite-element model simulations have shown how a sudden drop in liquid level affects temperature gradients, thermal distortion, and stress distribution in the solidifying steel shell near the meniscus.

- 1) These results illustrate an important mechanism assisting the formation of surface depressions and longitudinal cracks at the meniscus.
- 2) A severe, sudden level drop induces significant thermal distortion of the shell towards to liquid. The subsequent rise in liquid level causes the shell to bend even further inward. Shell distortion greater than 1 mm is predicted for a 0.6s level fluctuation of 20 mm. Subsequent overflow of the bent shell would create a transverse surface depression.
- 3) Large, rapid level drops induce large axial temperature gradients, which create high transverse tensile stresses in the shell, even in the absence of mold friction. This may be a cause of short, shallow, longitudinal surface cracks.
- 4) Ultra-low carbon steels and peritectic steels are expected to be particularly prone to this mechanism, owing to their high coherency temperature, which leads to strong initial shells that can resist flattening by ferrostatic pressure.

This mechanism emphasizes the vital importance of controlling mold level in order to avoid surface depressions, longitudinal cracks, and other defects.

4.7 References

1. E. Takeuchi and J.K. Brimacombe, The formation of oscillation marks in the continuous casting of steel slabs, *Met. Trans B*, vol. 15B (Sept) (1984) 493-509.
2. R.B. Mahapatra, J.K. Brimacombe and I.V. Samarasekera, Mold Behavior and its Influence on Product Quality in the Continuous Casting of Slabs: Part II. Mold Heat Transfer, Mold Flux Behavior, Formation of Oscillation Marks, Longitudinal Off-corner Depressions, and Subsurface Cracks, *Metallurgical Transactions*, vol. 22B (December) (1991) 875-888.
3. I.V. Samarasekera, J.K. Brimacombe and R. Bommaraju, Mold Behavior and Solidification in the Continuous Casting of Steel Billets, *Trans. I.S.S.*, vol. 5 (1984) 79-93.
4. I.G. Saucedo, Early Solidification during the Continuous Casting of Steel, in *Mold Operation for Quality and Productivity*, Iron and Steel Society, Warrendale, PA, (1992) 43-53.

5. A. Kusano, N. Sato, M. Okimori, S. Fukunaga and R. Nishihara, Improvement of Mold Fluxes for Stainless and Titanium Bearing Steels, in *Steelmaking Conference Proceedings*, Vol. 74, Iron and Steel Society, Warrendale, PA, (1991) 147-151.
6. M.S. Jenkins, B.G. Thomas, W.C. Chen and R.B. Mahapatra, Investigation of Strand Surface Defects using Mold Instrumentation and Modelling, in *Steelmaking Conference Proceedings*, Vol. 77, Iron and Steel Society, Warrendale, PA, (1994) 337-345.
7. S. Kumar, B.N. Walker, I.V. Samarasekera and J.K. Brimacombe, Chaos at the Meniscus - the Genesis of Defects in Continuously Cast Steel Billets, in *PTD Conference Proceedings*, Vol. 13, Iron and Steel Society, Warrendale, PA, (1995) 119-141.
8. B.G. Thomas, A. Moitra and R. McDavid, Simulation of Longitudinal Off-Corner Depressions in Continuously-Cast Steel Slabs, in *PTD Conference Proceedings*, Vol. 13, Iron and Steel Society, Warrendale, PA, (1995) 143-156.
9. S.N. Singh and K.E. Blazek, Heat Transfer and Skin Formation in a Continuous Casting Mold as a Function of Steel Carbon Content, in *Open Hearth Proceedings*, Vol. 57, Iron and Steel Society, Warrendale, PA, (1974) 16-36.
10. M. Wolf and W. Kurz, The Effect of Carbon Content on Solidification of Steel in the Continuous Casting Mold, *Metallurgical Transactions B*, vol. 12B (3) (1981) 85-93.
11. H. Yasunaka, K. Taniguchi, M. Kokita and T. Inoue, Surface Quality of Stainless Steel Type 304 Cast by Twin-roll Type Strip Caster, *ISIJ*, vol. 35 (6) (1995) 784-789.
12. S.G. Thornton and N.S. Hunter, The Application of Mould Thermal Monitoring to Aid Process and Quality Control When Slab Casting for Heavy Plate and Strip Grades, in *Steelmaking Conference Proceedings*, Vol. 73, Iron and Steel Society, Warrendale, PA, (1990) 261-274.
13. E. Hoffken, H. Laz and G. Pietzko, Development of Improved Immersion Nozzles for Continuous Slab Casting, in *Proceedings of the 4th International Conference Continuous Casting*, Stahl & Eissen, Brussels, (1988) 461-473.
14. K. Nakai, M. Kawasaki, K. Nakajima, T. Sakashita and Y. Sugitani, Improvement of Surface Quality of Continuously Cast Slab by Reducing Heat Flux Density in Mould, in *Continuous Casting '85 Proceedings*, Institute of Metals, London, UK, (1985) paper 71.
15. M. Wolf, Strand Surface Quality of Austenitic Steels: Part I. Macroscopic Shell Growth and Ferrite Distribution, *Ironmaking and Steelmaking*, vol. 13 (5) (1986) 248-257.
16. M.M. Wolf, Mold Heat Transfer and Lubrication Control - Two Major Functions of Caster Productivity and Quality Assurance, in *PTD Conference Proceedings*, Vol. 13, Iron and Steel Society, Warrendale, PA, (1995) 99-117.
17. S. Takeuchi, Y. Miki, S. Itoyama, K. Kobayashi, K. Sorimachi and T. Sakuraya, Control of Oscillation Mark Formation during Continuous Casting, in *Mold Operation for Quality and Productivity*, Iron and Steel Society, Warrendale, PA, (1992) 37-41.
18. A. Moitra, Thermo-mechanical model of Steel Shell Behavior in Continuous Casting, Ph.D. Thesis, University of Illinois at Urbana-Champaign (1993).
19. O.C. Zienkiewicz, *The Finite Element Method*, third ed., (McGraw Hill, New York, NY, 1977).

20. B.G. Thomas, I.V. Samarasekera and J.K. Brimacombe, Comparison of Numerical Modeling Techniques for Complex, Two-Dimensional, Transient Heat Conduction Problems, *Metall. Trans.*, vol. 15B (1984) 307-318.
21. E.C. Lemmon, Multidimensional Integral Phase Change Approximations for Finite Element Conduction Codes. *Numerical Methods in Heat Transfer*. (1981) 201-213.
22. T. Dupont, G. Fairweather and J. Johnson, Three-level Galerkin Methods for Parabolic Equations, *SIAM Journal of Numerical Analysis*, vol. 11 (1974) 392-410.
23. G. Forsythe and C. Moler, *Computer Solution of Linear Algebraic Systems*, (Prentice Hall, Englewood Cliffs, 1967).
24. A. Moitra and B.G. Thomas, Application of a Thermo-Mechanical Finite Element Model of Steel Shell Behavior in the Continuous Slab Casting Mold, in *Steelmaking Proceedings*, Vol. 76, Iron and Steel Society, (1993) 657-667.
25. B.G. Thomas and H. Zhu, Evaluation of Finite Element Methods for Simulation of Stresses During Solidification, *World Conference on Computational Mechanics III*, (1994) .
26. P. Kozlowski, B.G. Thomas, J. Azzi and H. Wang, Simple Constitutive Equations for Steel at High Temperature, *Metall. Trans. A*, vol. 23A (March) (1992) 903-918.
27. P.J. Wray, Effect of Carbon Content on the Plastic Flow of Plain Carbon Steels at Elevated Temperatures, *Met. Trans.*, vol. 13A (1) (1982) 125-134.
28. T. Suzuki, K.H. Tacke, K. Wunnenberg and K. Schwerdtfeger, Creep Properties of Steel at Continuous Casting Temperatures, *Ironmaking and Steelmaking*, vol. 15 (2) (1988) 90-100.
29. H. Mizukami, K. Murakami and Y. Miyashita, Mechanical Properties of Continuously Cast Steels at High Temperatures, *Tetsu-to-Hagane*, vol. 63 (146) (1977) S 652.
30. H. Zhu and B.G. Thomas, Evaluation of Finite Element Methods for Simulation of Stresses During Solidification, *University of Illinois, Report*, 1994.
31. B.G. Thomas, A. Moitra and H. Zhu, Coupled Thermo-mechanical Model of Solidifying Steel Shell Applied to Depression Defects in Continuous-cast Slabs, in *Modeling of Casting, Welding and Advanced Solidification Processes VII*, Vol. 7, M. Cross and J. Campbell, eds., TMS, Warrendale, PA, (1995) 241-248.
32. K. Harste, A. Jablonka and K. Schwerdtfeger, Shrinkage and Formation of Mechanical Stresses during Solidification of Round Steel Strands, 4th Int. Conf. on Continuous Casting, *Stahl und Eisen*, Brussels (1988) 633-644.
33. R.D. Pehlke, A. Jeyarajan and H. Wada, Summary of Thermal Properties for Casting Alloys and Mold Materials, Vol. NTIS-PB83-211003, (University of Michigan, Ann Arbor, MI, 1981).
34. H. Hiebler, J. Zirngast, C. Bernhard and M.M. Wolf, Inner Crack Formation in Continuous Casting: Stress or Strain Criterion, in *Steelmaking Conference Proceedings*, Vol. 77, Iron and Steel Society, Warrendale, PA, (1994) 405-416.
35. S. Dong, E. Niyama and K. Anzai, Free Deformation of Initial Solid Shell of Fe-C Alloys, *ISIJ International*, vol. 35 (6) (1995) 730-736.
36. J. Suni and H. Henein, Analysis of Shell Thickness Irregularity in Continuously Cast Middle Carbon Steel Slabs Using Mold Thermocouple Data, *Steelmaking Conference Proceedings*, vol. 76 (1993) 331-336.

37. J.K. Brimacombe, F. Weinberg and E.B. Hawbolt, Formation of Longitudinal, Midface Cracks in Continuously-Cast Slabs, Met Trans B, vol. 10B (1979) 279-292.

Chapter 5

Summary and Conclusions

Based on this investigation, several conclusions can be made:

1. Fixed-grid methods present special numerical difficulties which require careful consideration:

a) liquid can be handled using one of several different methods.

b) accuracy in the undiscretized direction can be improved by choosing the appropriate condition. Generalized plane strain is best solved with a direct method using a variable band-width solution algorithm.

2. A benchmark test problem for thermal-mechanical analysis of solidification with a known analytical solution has been developed, using a highly non-linear constitutive equation to create a severe numerical challenge. This test problem is ideal to compare finite element models for solving mechanical problems with solidification.

3. Decreasing time step size greatly increases accuracy. Accuracy within 3% is possible on a mesh with 17 elements across the solid shell. Refining mesh size also improves accuracy, but only if the time step size is sufficiently small. An optimum mesh size likely exists for each time step size. Accuracy within 0.1% is possible with 1000 time steps and 170 elements across the solid shell.

4. The alternating implicit-explicit scheme is stable and cheap compared with the forward Euler scheme and the backward Euler scheme. The implicit backward Euler scheme with proper constitutive algorithms takes 7 times of CPU time of this scheme while the explicit forward Euler scheme suffered the stability problem.

5. The implicit backward Euler scheme with the successive substitution method and non-iterative forward gradient method offer no or just less advantages compared with the explicit forward Euler scheme. The successive substitution method has a convergence problem while the forward gradient method lost the accuracy with relative large step size.
6. The bounded Newton-Raphson method is more efficient although both types of Newton-Raphson's methods performed very well.
7. The Nemat-Nasser's prediction method worked very well some problems and failed to the others.
8. A numerical efficient transient thermal-mechanical finite-element model has been developed to simulate temperature, shape and stress development in the steel shell, during the initial stages of solidification in the mold. This model can be applied to investigate the influences of processes parameters on the solidifying shell behavior and to understand the mechanisms of various defects-generating.
9. A severe, sudden level drop induces significant thermal distortion of the shell towards to liquid. The subsequent rise in liquid level causes the shell to bend even further inward. Shell distortion greater than 1 mm is predicted for a 0.6s level fluctuation of 20 mm. Subsequent overflow of the bent shell would create a transverse surface depression.
10. Large, rapid level drops induce large axial temperature gradients, which create high transverse tensile stresses in the shell, even in the absence of mold friction. This may be a cause of short, shallow, longitudinal surface cracks.
11. Ultra-low carbon steels and peritectic steels are expected to be particularly prone to this mechanism, owing to their high coherency temperature, which leads to strong initial shells that can resist flattening by ferrostatic pressure.

APPENDIX A Constant-Gradient Triangles Element in Chapter 4

For constant-gradient triangles the temperature variation across the element is defined by a linear equation as given by

$$T = a_0 + a_1x + a_2y . \quad (A1)$$

As the name suggests, this implies a constant temperature gradient or heat flux across the element. The temperature at any point in the element is given as

$$T(x,y) = \sum_{i=1}^3 N_i(x,y) T_i . \quad (A2)$$

The shape functions are given by the area coordinates as shown in Figure A.1 and are defined as:

$$[N] = \left[\frac{A_1}{A} \quad \frac{A_2}{A} \quad \frac{A_3}{A} \right] \quad (A.3)$$

where A_1, A_2, A_3 are the are of the triangles marked on the Figure A.1

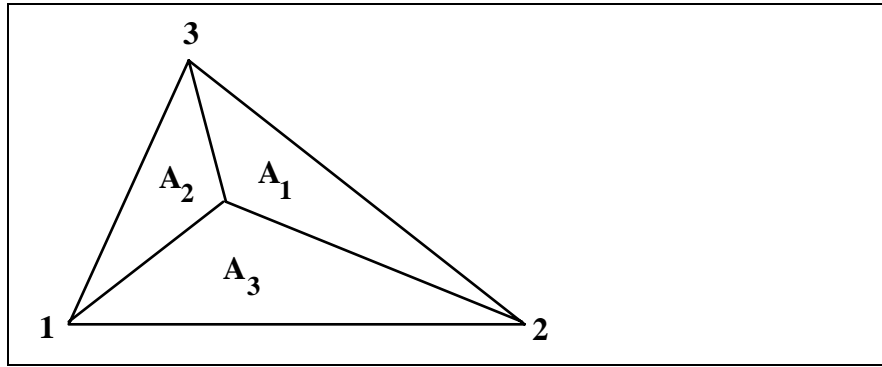


Figure A.1 Shape functions for constant gradient triangular elements

The nodal temperatures are defined as

$$\{T\} = \{ T_1 \quad T_2 \quad T_3 \}^T . \quad (A4)$$

The temperature gradient across the element can then be expressed as

$$\begin{Bmatrix} \frac{\partial T}{\partial x} \\ \frac{\partial T}{\partial y} \end{Bmatrix} = \begin{bmatrix} \frac{\partial N_1}{\partial x} & \frac{\partial N_2}{\partial x} & \frac{\partial N_3}{\partial x} \\ \frac{\partial N_1}{\partial y} & \frac{\partial N_2}{\partial y} & \frac{\partial N_3}{\partial y} \end{bmatrix} \begin{Bmatrix} T_1 \\ T_2 \\ T_3 \end{Bmatrix} .$$

(A5)

The [B] matrix for this element can be written in terms of the nodal coordinates, as

$$[B] = \frac{1}{2A} \begin{bmatrix} b_i & b_j & b_k \\ c_i & c_j & c_k \end{bmatrix} , \quad (A.6)$$

where

$$\begin{aligned} b_i &= x_j - x_k \\ c_i &= y_k - y_j \end{aligned} \quad (A.7)$$

Finally, for these elements the conductance and capacitance matrices can be directly evaluated using the following equation without using numerical integration

$$[K] = K_{ij} = \frac{t \cdot k(T)}{4A} (b_i b_j + c_i c_j) , \quad (A.8)$$

where $k(T)$ is the temperature dependent thermal conductivity

$$[C] = C_{ij} = \frac{t \cdot A}{12} \frac{\partial H(T)}{\partial T} (1 + \delta_{ij}) , \quad (A.9)$$

where $H(T)$ is the temperature dependent enthalpy function and the $\frac{\partial H(T)}{\partial T}$ term is defined

in Eq. 4.3. The thermal force vector $\{Q\}$ was formed as :

$$\{Q\} = \int N^T q'' dL = \frac{q'' L_{ij}}{2} , \quad (A.10)$$

where q'' is the heat flux and L_{ij} is the length of the boundary between node i,j . The material properties are evaluated at the centroid of the element where the temperature is given

$$T^e = \frac{1}{3} (T_1 + T_2 + T_3) . \quad (A.11)$$

